

Winter 2008

# Hafnium isotopic insights into the evolution of mantle source contributions to primitive lavas erupted in Turkana, East African Rift System

Jennifer A. Locke

*University of New Hampshire, Durham*

Follow this and additional works at: <https://scholars.unh.edu/thesis>

---

## Recommended Citation

Locke, Jennifer A., "Hafnium isotopic insights into the evolution of mantle source contributions to primitive lavas erupted in Turkana, East African Rift System" (2008). *Master's Theses and Capstones*. 425.  
<https://scholars.unh.edu/thesis/425>

This Thesis is brought to you for free and open access by the Student Scholarship at University of New Hampshire Scholars' Repository. It has been accepted for inclusion in Master's Theses and Capstones by an authorized administrator of University of New Hampshire Scholars' Repository. For more information, please contact [nicole.hentz@unh.edu](mailto:nicole.hentz@unh.edu).

HAFNIUM ISOTOPIC INSIGHTS INTO THE EVOLUTION OF MANTLE  
SOURCE CONTRIBUTIONS TO PRIMITIVE LAVAS ERUPTED IN TURKANA,  
EAST AFRICAN RIFT SYSTEM

BY

JENNIFER A. LOCKE

B.S., University of Washington, 2005

THESIS

Submitted to the University of New Hampshire

in Partial Fulfillment of

the Requirements for the Degree of

Master of Science

in

Earth Sciences: Geology

December, 2008

UMI Number: 1463229

### INFORMATION TO USERS

The quality of this reproduction is dependent upon the quality of the copy submitted. Broken or indistinct print, colored or poor quality illustrations and photographs, print bleed-through, substandard margins, and improper alignment can adversely affect reproduction.

In the unlikely event that the author did not send a complete manuscript and there are missing pages, these will be noted. Also, if unauthorized copyright material had to be removed, a note will indicate the deletion.

**UMI**<sup>®</sup>

---

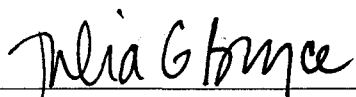
UMI Microform 1463229

Copyright 2009 by ProQuest LLC.

All rights reserved. This microform edition is protected against unauthorized copying under Title 17, United States Code.

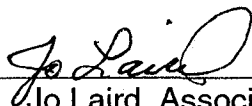
ProQuest LLC  
789 E. Eisenhower Parkway  
PO Box 1346  
Ann Arbor, MI 48106-1346

This thesis has been examined and approved.



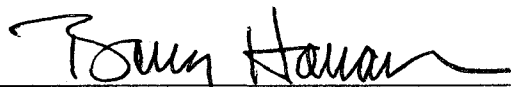
---

Thesis Director, Julia G. Bryce,  
Assistant Professor of Geochemistry



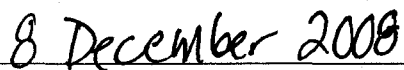
---

Jo Laird, Associate, Professor of Geology,  
Metamorphic Petrology



---

Barry Hanan, Staff Scientist,  
Isotopic Geochemistry,  
San Diego State University



---

Date

## **DEDICATION**

This thesis is dedicated to my parents, Tom and Alice Locke, and my sister, Anna Locke, who supported and encouraged me throughout my education.

## ACKNOWLEDGEMENTS

This thesis and completion of my master's degree would not have been possible without the mentorship of my adviser Julie Bryce. Thank you, Julie, for all your aid, constructive criticism, and support. I also have great appreciation for Barry Hanan who gave me use of his laboratory facilities at San Diego State University (SDSU) and taught me how to correct the raw data measured. A thanks also goes to Tyrone Rooney for leading me through the tedious lab procedures at SDSU. Tanya Furman was of great help with providing samples and her vast background knowledge of the Turkana area.

Thank you Jo Laird, for reviewing my writing and listening to countless practice presentations. Dave Graham at Oregon State University provided helium data and was significant in providing alternate insights and interpretations. I would also like to thank the late Karen von Damm who was an excellent teacher of geochemistry and offered generous support.

I am grateful to the National Science Foundation for funding this research through grant - EAR-0551960. I am also grateful to the UNH Earth Science department for awarding me a teaching assistantship for two years.

Finally many thanks go to my family and friends for their amazing support. Thank you to all my friends at UNH for being there throughout the classes, presentations, and writing. Thank you for the abundant fun and laughter. And thank you Mike, for always being there to help no matter how great the challenge.

## TABLE OF CONTENTS

DEDICATION	iii
ACKNOWLEDGEMENTS	iv
LIST OF TABLES	vii
LIST OF FIGURES	viii
ABSTRACT	x

CHAPTER	PAGE
I. INTRODUCTION	1
II. GEOLOGIC BACKGROUND	7
Volcanic and Tectonic Background	7
Mantle Plume Activity in the EARS?	8
Turkana Sample Petrology	9
Petrography and Mineral Compositions	12
III. METHODS	17
IV. RESULTS AND DISCUSSION	21
Source Contributions and Temporal Constraints	21
Regional Recurrence of Isotopic Signatures Observed in Turkana	27
Olivine Compositions and He (R/R <sub>A</sub> ) Data	33
Proposed Model	39
Comparisons to Other Continental Rifts	42

V. CONCLUSIONS	46
REFERENCES	48
APPENDICES	58
APPENDIX A: SAMPLE PETROGRAPHY	59
Quaternary Basalt Petrography	59
Tertiary Basalt Petrography	61
APPENDIX B: MICROPROBE DATA OF TURKANA OLIVINE	63
APPENDIX C: MICROPROBE DATA OF TURKANA CLINOPYROXENE	75
APPENDIX D: SAMPLE PREPERATIONS AND CHEMICAL PROCEDURES	94
Hafnium (Hf) Procedures	94
Lead (Pb) Procedures	99
Strontium (Sr) and Neodymium (Nd) Procedures	102
APPENDIX E: ISOTOPE STANDARDS	107



## LIST OF TABLES

TABLE		PAGE
1.	Rock Type and Locations of Turkana Samples	10
2.	Example Olivine Microprobe Data of Sample JRG 07	13
3.	Example Pyroxene Microprobe Data of Sample KCH-19	15
4.	Measured Isotopic Compositions	18
5.	Age Corrected Isotopic Compositions	20
6.	Quaternary Olivine Core Compositions	64
7.	Tertiary Olivine Core Compositions	66
8.	Quaternary Olivine Rim Compositions	67
9.	Tertiary Olivine Rim Compositions	68
10.	Quaternary Clinopyroxene Atomic Compositions	76
11.	Tertiary Clinopyroxene Atomic Compositions	78
12.	Quaternary Clinopyroxene End-Member Compositions	81
13.	Tertiary Clinopyroxene End-Member Compositions	84
14.	Hf Standard Measurements and Averages	108
15.	Pb Standard Measurements and Averages	109
16.	Nd Standard Measurements and Averages	109
17.	Sr Standard Measurements and Averages	109

## LIST OF FIGURES

FIGURE	PAGE
1. Map of the EARS	4
2. Map of the Turkana region of the EARS	5
3. Alkalis versus silica compositions	11
4. Example microphotograph of JRG 07 olivine #2	14
5. Olivine Fo and NiO compositions	14
6. Example microphotograph of KCH-19 pyroxene #4	16
7. Clinopyroxene compositions	16
8. $\epsilon_{\text{Hf}}$ versus $^{206}\text{Pb}/^{204}\text{Pb}$	22
9. $\epsilon_{\text{Hf}}$ versus $\epsilon_{\text{Nd}}$	24
10. $\epsilon_{\text{Hf}}$ versus $^{87}\text{Sr}/^{86}\text{Sr}$	26
11. $^{206}\text{Pb}/^{204}\text{Pb}$ versus $^{143}\text{Nd}/^{144}\text{Nd}$	28
12. $^{206}\text{Pb}/^{204}\text{Pb}$ versus $^{207}\text{Pb}/^{204}\text{Pb}$	28
13. $^{206}\text{Pb}/^{204}\text{Pb}$ versus $^{208}\text{Pb}/^{204}\text{Pb}$	29
14. $^{206}\text{Pb}/^{204}\text{Pb}$ versus $^{143}\text{Nd}/^{144}\text{Nd}$ with Regional Data	29
15. $^{206}\text{Pb}/^{204}\text{Pb}$ versus $^{207}\text{Pb}/^{204}\text{Pb}$ with Regional Data	30
16. $^{206}\text{Pb}/^{204}\text{Pb}$ versus $^{208}\text{Pb}/^{204}\text{Pb}$ with Regional Data	30
17. $^{206}\text{Pb}/^{204}\text{Pb}$ versus $^{143}\text{Nd}/^{144}\text{Nd}$ with Napak and Mt. Elgon Data	32
18. Graph of $^{206}\text{Pb}/^{204}\text{Pb}$ versus $^{87}\text{Sr}/^{86}\text{Sr}$	32
19. Olivine Fo and Ni compositions with Peridotite and Hawaiian data	34

20.	Map of the EARS with He (R/R <sub>A</sub> ) Data	36
21.	Proposed Model	40
22.	Olivine microphotographs BR-05 #1 and #2	69
23.	Olivine microphotographs CI-31 #1 and #2	70
24.	Olivine microphotograph SI-24 #1	71
25.	Olivine microphotograph SI-24 #2	71
26.	Olivine microphotograph SI-24 #5	72
27.	Olivine microphotograph JRG 07 #1	72
28.	Olivine microphotograph JRG 07 #2	73
29.	Olivine microphotograph JRG 07 #4	73
30.	Olivine microphotograph JRG 10 #1 and #2	74
31.	Pyroxene microphotographs CI-10 #4 and #5	88
32.	Pyroxene microphotograph KCH-19 #1	89
33.	Pyroxene microphotograph KCH-19 #4	89
34.	Pyroxene microphotograph KCH-19 #6	90
35.	Pyroxene microphotograph KJ 1 #1	90
36.	Pyroxene microphotograph KJ 1 #2	91
37.	Pyroxene microphotograph KJ 1 #5	91
38.	Pyroxene microphotograph JRG 07 #2	92
39.	Pyroxene microphotograph JRG 07 #3	92
40.	Pyroxene microphotograph JRG 07 #5	93

## ABSTRACT

# HAFNIUM ISOTOPIC INSIGHTS INTO THE EVOLUTION OF MANTLE SOURCE CONTRIBUTIONS TO PRIMITIVE LAVAS ERUPTED IN TURKANA, EAST AFRICAN RIFT SYSTEM

by

Jennifer A. Locke

University of New Hampshire, December, 2008

Compositions of mafic lavas from the Turkana region, within the East African Rift System (EARS), provide valuable contributions to the understanding of the significant processes in continental magmatism. Specifically, new Hf isotopic ratios coupled with new and existing Pb, Sr, Nd, and He isotopic compositions of Quaternary and Tertiary lavas from Turkana reveal compositional contributions from melt generation processes occurring in the sublithospheric mantle versus contributions from melt generation processes in the lithosphere. Pb and Nd compositions demonstrate two separate mixing trends within the Turkana lavas, and together with Sr isotopic compositions, three compositional end-members are revealed: C-Component, EM1, and HIMU. New Hf isotope ratios of the Quaternary and Tertiary Turkana samples presented a temporal correlation, in Hf-Pb space one trend progresses from an EM1-like component to a C-component over time, while the other trend progresses from a HIMU like

component to an EM1 like component throughout time. Based on compositional and spatiotemporal relationships, a model is proposed where HIMU is a lithospheric component, EM1 is a sublithospheric component that acts as an agent of metasomatism in the lithosphere, and the C-component is a second sublithospheric end-member likely present as a result of regional plume activity.

## CHAPTER I

### INTRODUCTION

Basaltic rock, covering over three-quarters of Earth's surface, is emplaced on the surface by melting and transportation processes in lithospheric mantle and/or sublithospheric mantle. Studying the composition of basalt and the processes that generate, alter, and transport basaltic magma are essential in expanding our understanding of the chemistry, physics, and mechanics of the mantle and capturing the flux of mass and heat through this inner silicate reservoir to the crust. Rock compositions provide one means to parameterize the contributions from melt generation and transport processes occurring in the sublithospheric mantle versus contributions from the lithosphere. The important processes relevant to melt generation and transportation include the upwelling of melt within the mantle, mixing of melts from different source regions, stalling of melt within magma chambers and the differentiation of melt, fractional crystallization, partial melting of surrounding material, and assimilation of surrounding material (e.g., Vollmer & Norry, 1983; De Mulder et al., 1986; Davies & MacDondald, 1987; Ribe, 1987; Davidson & Wilson, 1989; Richter & Daly, 1989; Morley, 1994; Simonetti & Bell, 1994; Simonetti & Bell, 1995; Paslick et al., 1996; Stewart & Rogers, 1996; Davidson & Tepley, 1997; Trua et al., 1999; Davidson et al., 2001; Späth et al., 2001; and Spera & Bohrson, 2004).

Magma generation in oceanic rifts constitutes a volumetrically important component of the basaltic magma flux. Accordingly, numerous studies have provided many insights into the links between the compositions and dynamics of these basaltic magmas in terms of their generation, transport, and emplacement (Hamelin et al., 1984; Prinzhofer et al., 1989; Sun & McDonough 1989; Kelemen et al., 1997; Sims & DePaolo, 1997; Sours-Page et al., 1999; Forsyth & Detrick, 2003; Sours-Page et al., 2003; and Putirka, 2005 among others). In comparison, the similarities and distinctions of these processes in continental rifts remain less well known, even though continental rifts are responsible for basaltic magma production in the forms of flood basalts, large igneous provinces (LIPs), shield volcanoes, and smaller flows through vents (e.g., Hart et al., 1989; Pik et al., 1999; Späth, 2001; Peccerillo et al., 2003; Furman et al., 2004; Ramos et al., 2005; Furman et al., 2006a; Furman et al., 2006b and many others). Though far more accessible, our understanding of magmatic processes of continental rifting has in some regards lagged behind, largely due to influences of crustal overprinting by assimilation. An essential question that remains controversial is whether continental rift magmatism is from the upwelling of buoyant material from the deep mantle, in the form of a mantle plume, or instead from decompressional melting of the upper mantle as a result of extension of the lithosphere. The chemical distinction between these separate potential source regions is readily disguised by crustal overprinting during the ascension of the magma through the lithosphere. In the last few decades, significant progress has been made in understanding both the tectonic and magmatic components of continental rifting

processes through use of integrated geochemical, geophysical, and tomographic methods (e.g., KRISP Working Group, 1995). These techniques, taken together, are more problematically applied in oceanic basins with most of the emphasis on mid-ocean ridges (e.g., Forsyth et al., 1998; Forsyth & Detrick, 2003; and Yingije & Forsyth, 2005), as opposed to hotspot or plume related volcanism (e.g., Li et al., 1990 and Osada et al., 2003).

The East African Rift System (EARS) is the classic example of continental rifting and provides a favorable site to research the processes significant in continental magma generation (Figure 1). Multiple episodes of basaltic volcanism have occurred throughout the EARS beginning 45 Ma (George et al., 1998) through the Quaternary. Several episodes of volcanism include periods of eruptions producing high volume flood basalts; one specific large eruptive event occurred around 30 Ma directly before rifting began at about 27 Ma (Schilling et al., 1992 and Pik et al., 1999). Periods of volcanism and rifting have continued up to present day.

The Turkana depression, located between the Ethiopian Plateau and the East African Plateau (Figure 2), has the thinnest lithosphere in the EARS and therefore the modern lavas that have erupted in this region have traveled through less lithosphere than in other areas. These lavas are the ideal samples for looking at mantle sources for this region, and possibly other regions, of the EARS because they likely have the least continental lithospheric contamination.



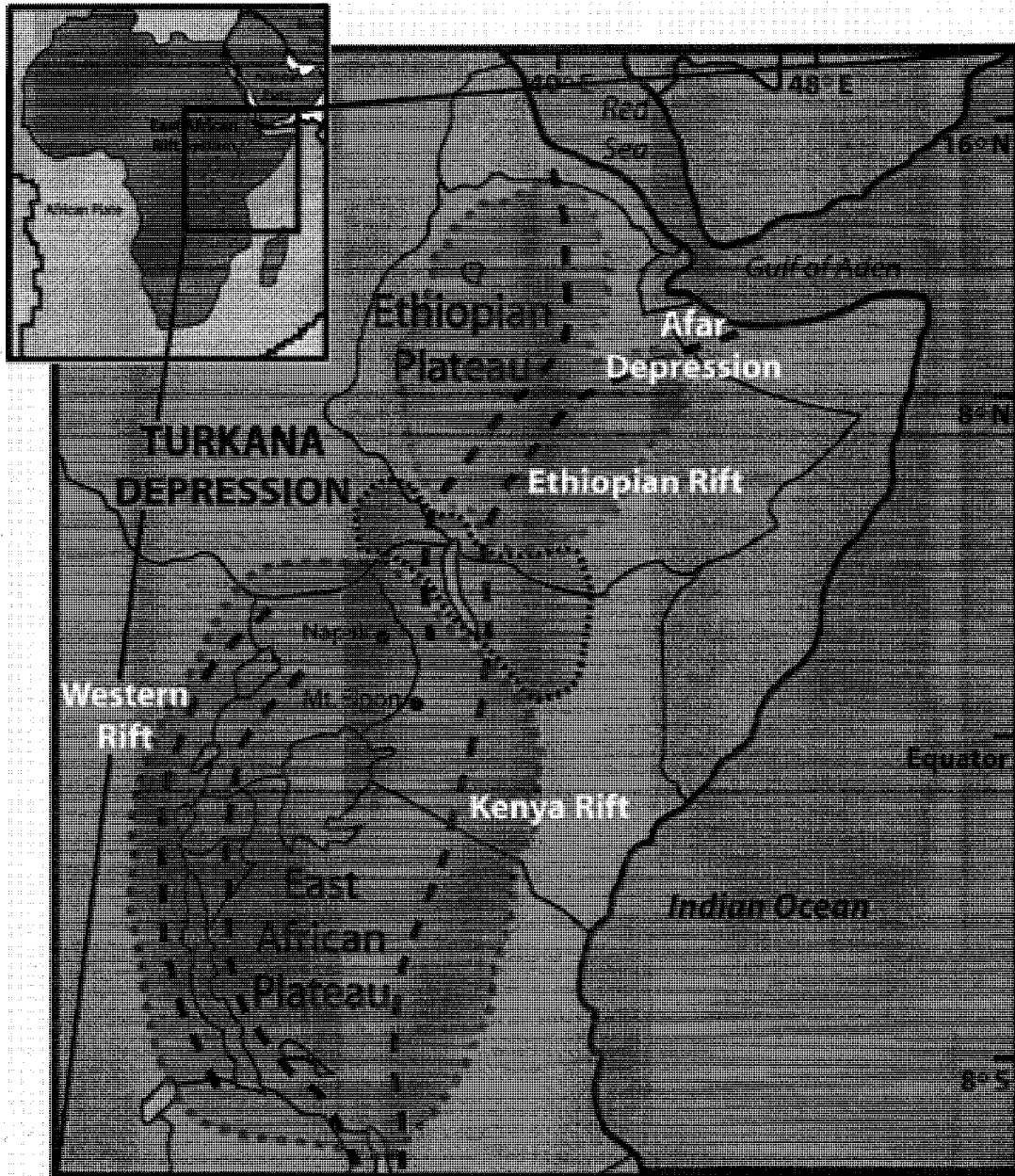


**Figure 1:** Map of the EARS showing location of the rifts (in bold dashed lines). The two brown dashed lines outline the two plateaus, and the blue dashed line outlines the Turkana Depression. Key geological regions are identified on the map.

Previous studies of mafic lavas from the Turkana region by Furman et al. (2004, 2006a) provided several constraints on the source regions for the lavas erupting in both the Quaternary and Tertiary. These studies, along with additional datasets from Curtis (1991), found a mixing trend in the lava

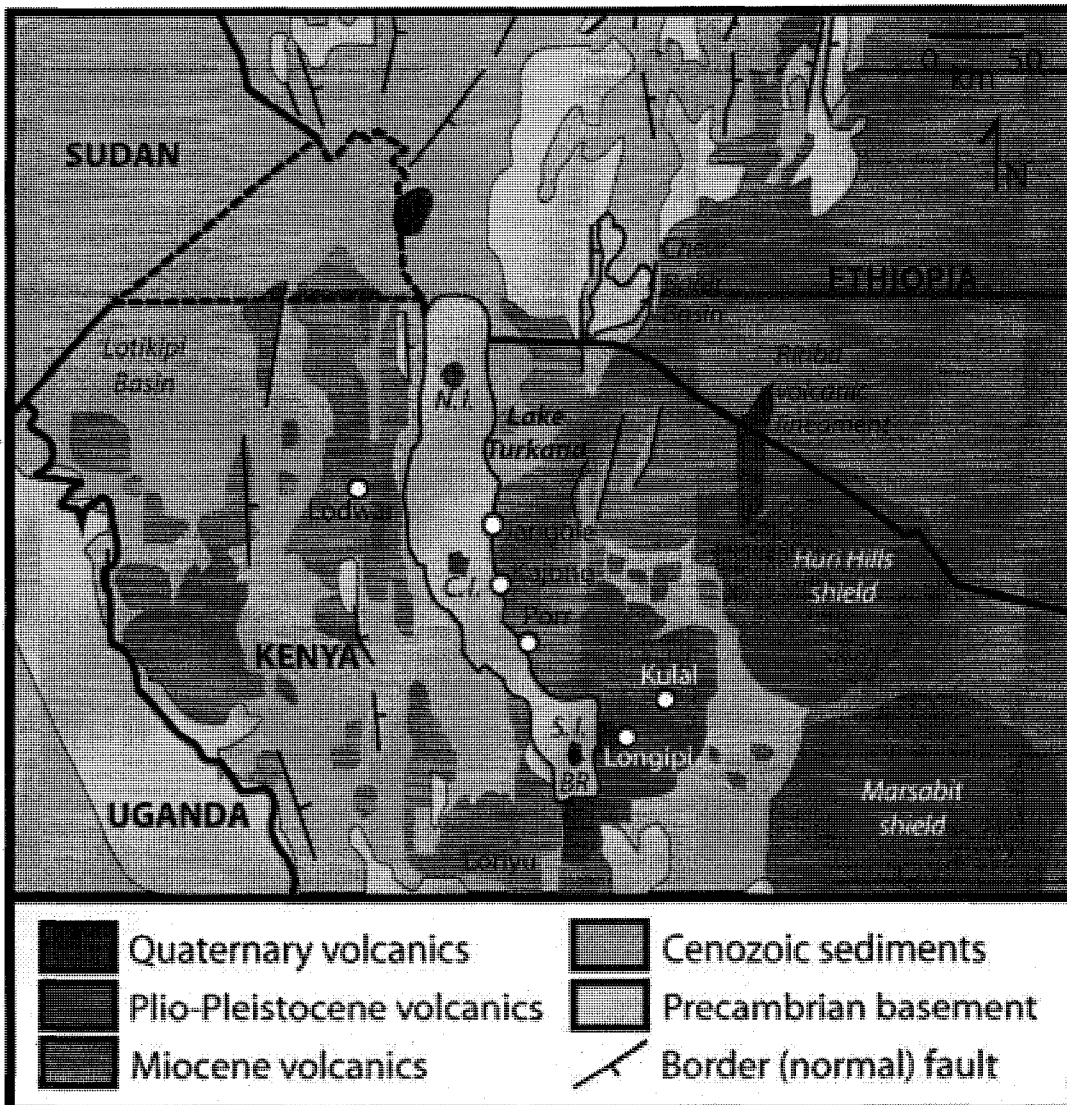


**Figure 2:** Map of the Turkana region of the EARS. N.I., C.I., S.I., and BR are North Island, Central Island, South Island, and Barrier Island respectively. After Furman et al. (2006a).

compositions between at least two distinct sources. The Tertiary Turkana samples in general had high  $^{206}\text{Pb}/^{204}\text{Pb}$  values that are similar to a HIMU composition (as defined by Stracke et al., 2005), meaning the lavas have a very high U/Pb ratio and therefore the samples are enriched in radiogenic Pb. The origin of HIMU is controversial, though the most accepted interpretation is that the source includes ancient subducted oceanic crust that has been entrained in a

rising plume or melts (Stracke et al., 2005). The Quaternary samples on average had lower  $^{206}\text{Pb}/^{204}\text{Pb}$  values that are similar to C-component (as defined by Hanan & Graham, 1996) which is the most common source for ocean island basalts (OIBs) and interpreted to have a mantle plume origin.

A seismic low-velocity anomaly has been observed in northeast Africa below the Afar depression and the Main Ethiopian Plateau and is interpreted to be at least one mantle plume called the Afar Plume (Debaille et al., 2001). A separate thermal anomaly has been observed in tomographic studies to be below the Turkana depression and the Kenyan Rift (Nyblade et al., 2000; Debaille et al., 2001; and Montelli et al., 2004). One hypothesis is that the volcanism in the Turkana region taps from two mantle plumes (George & Rogers, 2002) that may connect at depth in the mantle.

The previous studies of the Turkana region provide valuable insights to the compositions erupted, however the origins of these compositions remain poorly constrained. The purpose of this work is to resolve source contributions from convecting/sublithospheric mantle versus those acquired from the subcontinental lithospheric mantle and determine how these source contributions vary throughout time. This study uses new Hf, Sr, Nd, Pb and He isotopic data of Quaternary and Tertiary Turkana basalts, coupled with existing Pb, Sr, Nd and He isotopic data, to reveal the processes and source end-members of the Turkana region of the EARS, and ultimately will be utilized in integrated geochemical-geophysical modeling of continental rifting volcanism (e.g., Lin et al., 2007).

## CHAPTER II

### GEOLOGIC BACKGROUND

#### Volcanic and Tectonic Background

The EARS forms a branch of the Afar Triple Junction with the Red Sea Rift and the Gulf of Aden Rift (Figure 1), stretching about 3000 km N-NE in northeastern Africa. There are several rift sections that comprise the EARS, from North to South: the Afar Depression, the Main Ethiopian Rift, the Turkana Depression, and the Kenyan Rift. The Western Rift is located to the west of the Kenyan Rift.

The Turkana region has a long history of rifting, first beginning in the Cretaceous on the eastern side of Lake Turkana (Morley et al., 1992). Faults formed in the region throughout the Neogene and alternated between being active and inactive. The first large episodes of basaltic volcanism in the EARS, at 45 Ma and 30 Ma, both occurred in the Turkana and south Ethiopian regions (Davidson & Rex, 1980). In the Miocene and up through the Quaternary new faults opened to the west of Lake Turkana in the Lotikipi Basin and extended to the southeast (Furman et al., 2006). With seismic tomography other faults can be observed beneath Lake Turkana, where a large rift structure is apparent and is considered to be a northern extension of the Kenyan Rift (Dunklemann et al., 1988; Morley et al., 1992; and Hendrie et al., 1994). The rift beneath Lake Turkana is a series of half-grabens along the length of the lake, each graben is

approximately 20 km long and 10 km wide (Dunklemann et al., 1988). Ebinger et al. (2000) inferred that rifting of the EARS began in the Turkana region after the flood basalts at 30 Ma, then rifting propagated to the north and south forming the Ethiopian Rift and the Kenya Rift.

The Turkana depression rift is about 150 km wide, three times wider than other regions of the EARS (Morley et al., 1992). Most of the volcanism that took place in the Quaternary was along the axis of the rift beneath Lake Turkana, while the Tertiary volcanism was much more widespread (Figure 2). Simple models employing decompressional melting with adiabatic upwelling of subcontinental lithosphere cannot uniquely explain the mechanism of magma generation because the episodic nature of the rifting that occurred in the Turkana region did not produce enough extension per rifting episode (Ebinger & Ibrahim, 1994; Hendrie et al., 1994; and Furman et al., 2006). Also, the chemical data of the Turkana lavas are heterogeneous and are not entirely chemically consistent with derivation of mantle that produces MORB. Instead, geochemical, geophysical, and geological data are consistent with the concept that the volcanism from the Miocene through the Quaternary is due to increased mantle temperatures, likely from an emplaced mantle plume (Furman et al., 2006a).

### **Mantle Plume Activity in the EARS?**

The low-velocity seismic anomaly below the Afar depression attributed to the Afar Plume (Debaille et al., 2001) along with the thermal anomaly below the Turkana depression and the Kenyan Rift (Nyblade et al., 2000; Debaille et al.,

2001; and Montelli et al., 2004), may in fact be part of an even larger structure at depth. Some studies hypothesize that the Ethiopian and East African Plateaus are part of a larger geological entity that also encompasses the Southern African Plateau and the southeastern Atlantic Ocean Basin; this feature is referred to as the African Superswell (Nyblade & Robinson, 1994; Nyblade et al., 2000; and Nyblade, 2003). The volcanism and rifting in eastern Africa and heat flow measurements of southern Africa indicate that each component of the Superswell is at least in part, if not entirely, due to a thermal perturbation to the lithosphere (Nyblade & Robinson, 1994; Nyblade et al., 2000; and Nyblade, 2003).

The anomaly responsible for the Southern African Plateau is not as clear as the seismic data of the Afar plume below East Africa. However, it seems that the three separate anomalies comprising the Superswell have a common origin at depth in the mantle. Nyblade et al. (2000) proposes that the Southern African Plateau is a remnant uplift from a Mesozoic mantle plume. These proposals are consistent with the hypothesis that the C-component and/or the HIMU-like signatures in the Turkana region are from a deep mantle source.

### **Turkana Sample Petrology**

To minimize chances for crustal overprinting, this study employs primitive samples that are the least likely to have crustal signatures. Within the high MgO suite, Tertiary and Quaternary Turkana samples contain alkaline and subalkaline compositions (Table 1). The Quaternary samples, generally less alkaline

**Table 1:**

Location and compositions of Quaternary and Tertiary Turkana samples. \* Ages used for correction from Ochieng' et al. (1988), except samples KJ 16 and LGP 607 from Furman et al. (2006) analyzed by R. Duncan.

Quaternary:								
Sample	Location	Long (° N)	Lat (° E)	Age (Myr)*	Rock type	Alk. Index	SiO <sub>2</sub> (wt. %)	MgO (wt. %)
BR-05	Barrier Island	2.63	36.6	<1	Basalt	-0.80	47.40	13.10
BR-33	Barrier Island	2.63	36.6	<1	Basalt	0.68	46.50	7.06
CI-08B	Central Island	3.5	36.05	<1	Trachy-basalt	1.40	48.98	5.84
CI-09B	Central Island	3.5	36.05	<1	Basalt	1.14	47.56	6.15
CI-10A	Central Island	3.5	36.05	<1	Basalt	1.28	47.80	5.64
CI-31	Central Island	3.5	36.05	<1	Basalt	0.54	46.26	10.10
CI-32	Central Island	3.5	36.05	<1	Picro-basalt	0.65	43.70	9.63
KCH-16	South Island	2.63	36.6	<1	Basalt	0.11	45.60	5.80
KCH-19	South Island	2.63	36.6	<1	-	-	-	-
SI-15	South Island	2.63	36.6	<1	Basalt	1.48	46.93	7.25
SI-20B	South Island	2.63	36.6	<1	Basalt	-0.05	46.20	14.10
SI-24	South Island	2.63	36.6	<1	Basalt	0.75	45.51	11.57
LGP 92-11	Longipi	2.62	36.6	-	-	-	-	-
LGP 607	Longipi	2.62	36.6	1.5	Tephrite basanite	3.21	42.48	12.08
LGP 36	Longipi	2.62	36.75	2.5	Tephrite basanite	3.50	42.86	11.48
LGP 39	Longipi	2.62	36.75	2.5	Trachy-basalt	2.75	45.79	10.17

Tertiary:								
Sample	Location	Long (° N)	Lat (° E)	Age (Myr)*	Rock type	Alk. Index	SiO <sub>2</sub> (wt. %)	MgO (wt. %)
KJ 1	Kajong	3	36.6	39	Foidite	5.28	40.78	8.08
KJ 16	Kajong	3	36.6	39.2	Basalt	1.84	47.11	9.54
LOR 86-23B	Loriyu	2	36.3	-	-	-	-	-
KL 18	Kulal	2.72	36.93	3	Basalt	1.52	46.37	7.31
JRG 03	Jarigole	3.6	36.25	-	-	-	-	-
JRG 07	Jarigole	3.6	36.25	20	Basalt	0.55	45.51	14.34
JRG 10	Jarigole	3.6	36.25	20	Picro-basalt	0.17	43.90	22.37
JRG 12	Jarigole	3.6	36.25	20	Picro-basalt	0.48	42.49	28.65
PORR 404	Porr	2.9	36.55	35	Tephrite basanite	4.78	44.07	8.50
PORR 602	Porr	2.9	36.55	35	Tephrite basanite	4.81	44.87	7.97
PORR 606	Porr	2.9	36.55	35	Tephrite basanite	2.91	43.62	8.59

(Furman et al., 2004, 2006a), have basaltic, picro-basaltic, trachy-basaltic, and tephrite basanitic compositions (Figure 3) (Furman et al., 2004). The Tertiary samples more diverse with basalt, picro-basalt, tephrite basanite, and foidite compositions (Furman et al., 2006a).

The majority of the Tertiary and Quaternary Turkana samples in this study have MgO contents between 6 and 14 wt. %, however a few Tertiary samples (JRG 07, JRG 10, and JRG 12 from Jarigole) have MgO >14 wt. %. These high MgO levels are interpreted to result from olivine accumulation (Furman et.

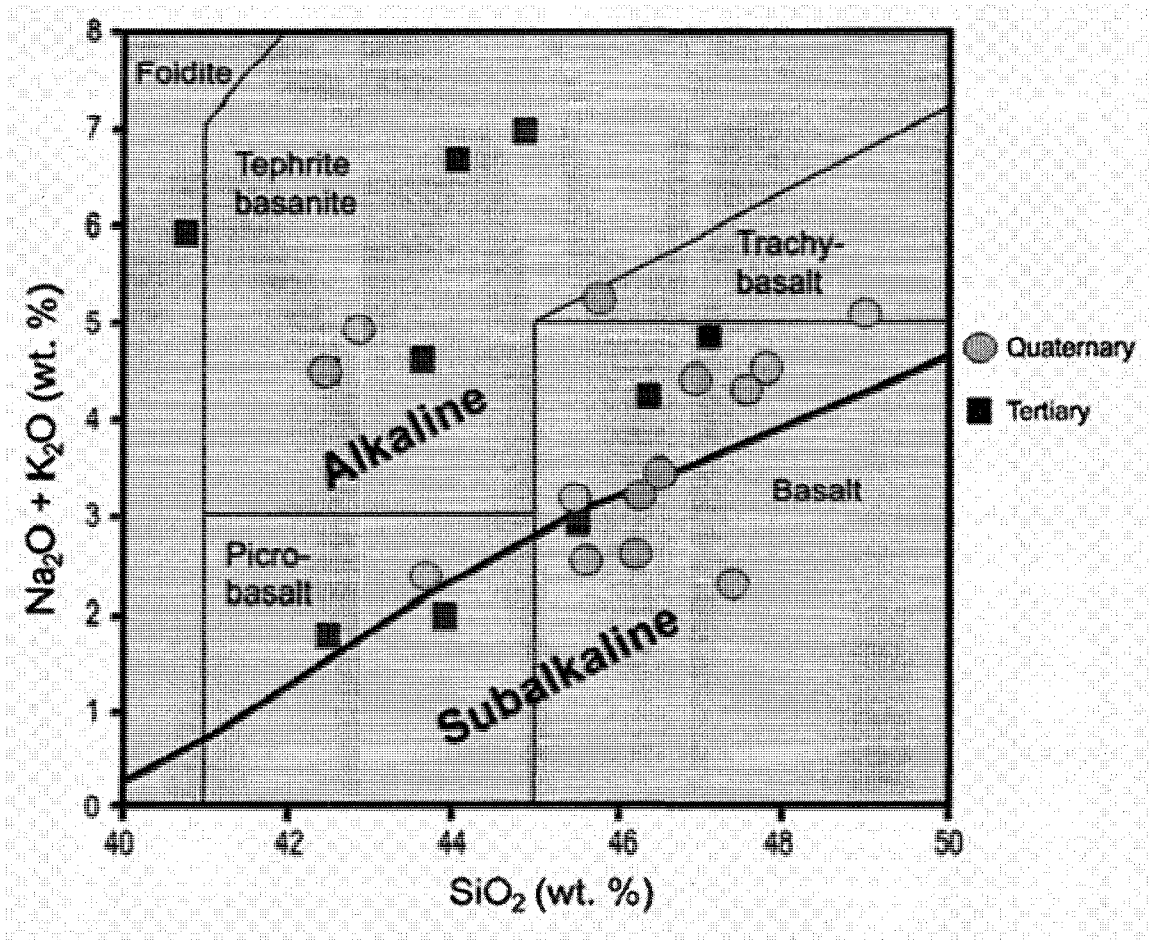


**Figure 3:** Alkalies versus silica weight percent of Quaternary and Tertiary Turkana samples (Furman et al., 2004 and 2006a).

al., 2004, 2006a). Trace element data have been used to constrain source mineralogy contents in Turkana lavas (Furman & Graham, 1999; and Furman et al., 2004, 2006a). Elevated Ba/Rb coupled with low Rb/Sr is indicative of hydrous phases (such as amphibole) in one of the source components. High values of Ba/Th with low Th concentrations for several samples also indicated metasomatic processes were involved in the melt region (Furman et al., 2004, 2006a).



## **Petrography and Mineral Compositions**

The Tertiary and Quaternary samples are massive to vesicular with olivine, plagioclase, and/or pyroxene phenocrysts. The groundmass is microcrystalline with the same mineralogy as the phenocrysts with trace amounts of oxides. For complete detailed sample descriptions see Appendix A. Olivine phenocrysts of five Quaternary and Tertiary samples were analyzed for major element compositions on a JEOL JXA-733 Superprobe at the Electron Microprobe Facility in the Center for Geochemical Analysis at Massachusetts Institute of Technology (MIT). An example of the data collected is shown in Table 2 for sample JRG 07, and an example of the microphotograph with points analyzed is shown in Figure 4 (for all data and microphotographs see Appendix B). Many Quaternary and Tertiary samples contained olivine phenocrysts with rims that have distinct compositions compared to the cores. A few samples, both Quaternary and Tertiary, lacked this zonation. The cores of the olivine phenocrysts had a range of forsterite compositions between Fo<sub>84</sub> to Fo<sub>88</sub> (Figure 5, data in Appendix B). Olivine rim compositions were as low as Fo<sub>58</sub>, but the majority rim compositions ranged from Fo<sub>63</sub> to Fo<sub>73</sub>. High total element weight percents (>98.5 %) imply that these compositional variations are not due to surface alteration, instead the wide range of compositions is likely due to magma mixing. Nickel content of the olivine phenocrysts varied between 0.16 to 0.33 wt. % NiO in the cores and 0.10 to 0.29 wt. % NiO in the rims (Figure 5, data in Appendix B). NiO-Fo relationships have previously been used in basalts to infer the lithology of the source region (Sobolev et al., 2005). In the Turkana samples,

**Table 2:**

Example table of microprobe data from JRG 07 olivine cores and rims. Data of all olivines analyzed are reported in Appendix B. The cores have very homogeneous compositions and therefore the averages of the cores are used, the rims have diverse compositions and therefore each data point is interpreted individually.

Sample	Mineral #	Fo %			NiO wt. %			Totals %
		Measured	Average	Std. Dev.	Measured	Average	Std. Dev.	
<b>CORES:</b>								
JRG 07	2	87.8			0.40			99.1
JRG 07	2	87.6			0.31			99.1
JRG 07	2	87.2	87.6	0.3	0.35	0.36	0.04	99.9
JRG 07	2	87.9			0.36			98.8
JRG 07	2	87.5			0.39			99.4
JRG 07	2	87.7			0.32			99.0
JRG 07	2	87.5			0.29			99.5
JRG 07	2	87.3	87.5	0.2	0.31	0.31	0.01	100.0
JRG 07	2	87.7			0.32			99.5
JRG 07	2	87.6			0.32			99.1
<b>RIMS:</b>								
JRG 07	2	81.56			0.31			100.1
JRG 07	2	80.14			0.26			99.1
JRG 07	2	83.61			0.23			98.9
JRG 07	2	80.71			0.28			99.8
JRG 07	2	63.07			0.16			98.7
JRG 07	2	63.76			0.17			98.9
JRG 07	2	65.26			0.16			99.9
JRG 07	2	71.98			0.20			99.3

elevated NiO contents in Fo-rich olivines (e.g., JRG-07 from Jarigole and sample SI-24 from South Island) are consistent with derivation from a mantle source region rich in pyroxene (Sobolev et al., 2005).

Four Quaternary and Tertiary samples were chosen to analyze pyroxene phenocrysts for major element compositions with the electron microprobe at MIT. Several grains, Quaternary and Tertiary, showed zonations, some oscillating from core to rim, while others showed random patterns of zones. An example of the data collected is shown in Table 3 of sample KCH-19, and an example microphotograph with points analyzed is shown in Figure 6 (for all data and microphotographs see Appendix C). The compositions ranged from

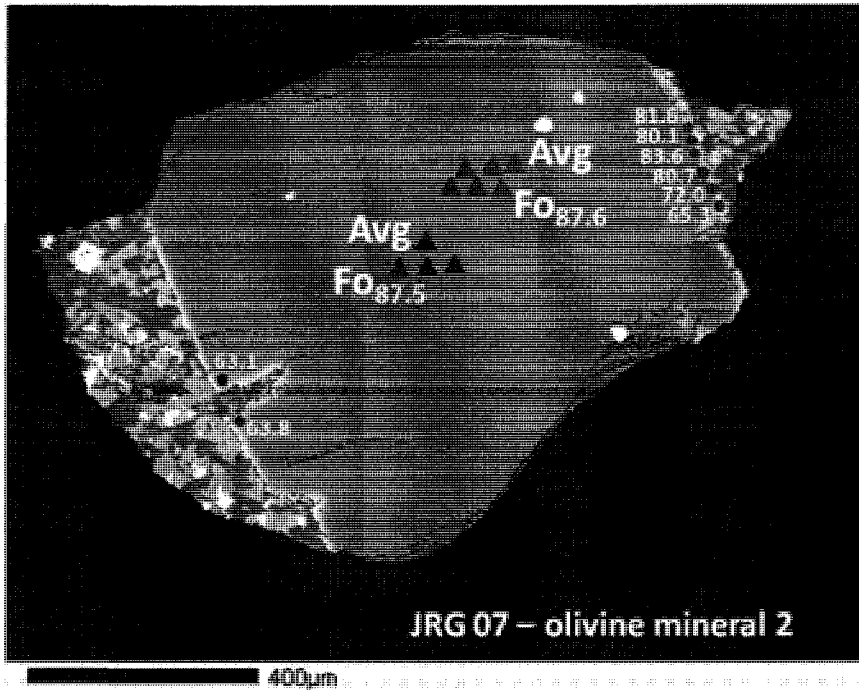


**Figure 4:** Example microphotograph of olivine #2 of JRG 07. To see all microphotographs of olivines analyzed see Appendix B. Triangles represent points measured of the core, with the average forsterite compositions shown for the two groups measured. Dots represent points measured of the rim, with forsterite compositions shown for each point.

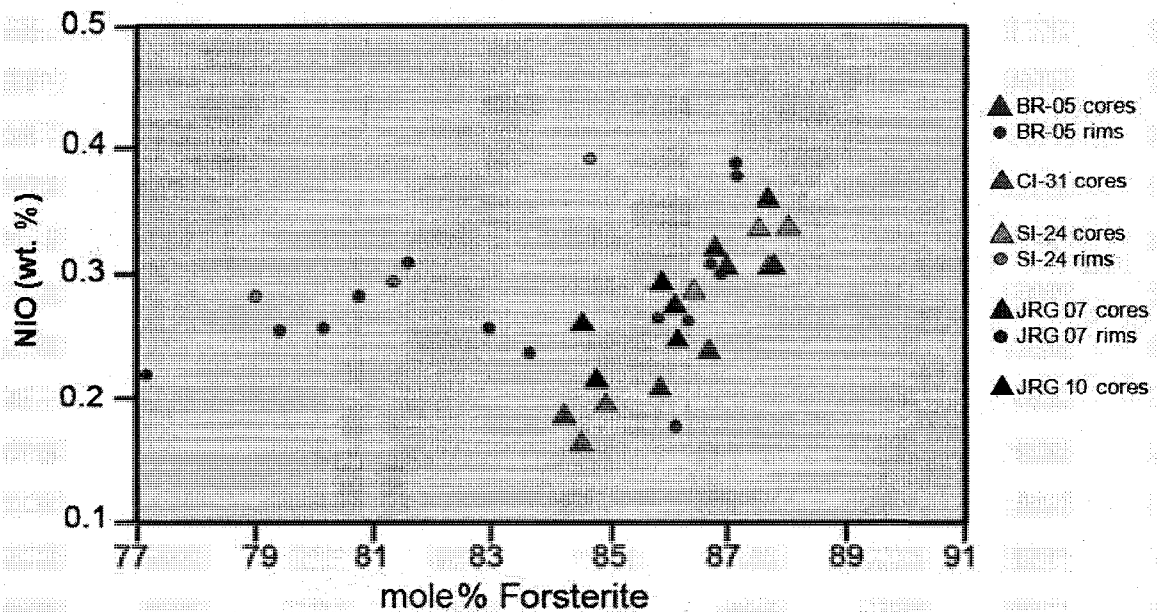


**Figure 5:** Forsterite composition versus nickel weight percent of Quaternary (BR-05, CI-31, and SI-24) and Tertiary (JRG 07 and JRG 10) Turkana olivine. Triangle symbols represent the core compositions of the olivine crystals, the dots represent the rim compositions.

**Table 3:**

Example table of microprobe data from KCH-19 pyroxene #4 transects. For data of all pyroxenes analyzed see Appendix C. The end-member compositions of enstatite (En), ferrosilite (Fs), wollastonite (Wo), and other (jadeite and CaTs) are shown (see Appendix C for more complete explanation). The end-members En, Fs, and Wo are then re-normalized in the far right column.  $Fe^* = Fe + Mn$ .

Sample	Mineral #	Point #	End-member mole percentages				Normalized end-members		
			En(Mg)	Fs( $Fe^*$ )	Wo(Ca)	Other	En(Mg)	Fs( $Fe^*$ )	Wo(Ca)
KCH-19	4	1a	42.37	8.86	41.07	7.70	45.91	9.59	44.49
KCH-19	4	2a	41.14	8.80	42.40	7.67	44.56	9.53	45.92
KCH-19	4	3a	42.15	8.94	41.45	7.46	45.55	9.66	44.79
KCH-19	4	4a	43.02	9.14	40.30	7.54	46.53	9.89	43.58
KCH-19	4	5a	45.94	7.37	40.29	6.40	49.08	7.88	43.04
KCH-19	4	6a	41.96	8.87	41.69	7.48	45.35	9.59	45.06
KCH-19	4	8a	38.59	12.70	41.58	7.13	41.55	13.68	44.77
KCH-19	4	1b	35.72	14.73	43.76	5.79	37.92	15.64	46.45
KCH-19	4	2b	39.86	12.91	43.26	3.96	41.51	13.45	45.05
KCH-19	4	3b	43.77	9.28	42.33	4.63	45.89	9.73	44.38
KCH-19	4	4b	42.53	9.26	42.33	5.88	45.19	9.83	44.98
KCH-19	4	5b	43.60	9.96	41.82	4.62	45.71	10.45	43.84
KCH-19	4	6b	43.59	10.09	42.39	3.93	45.38	10.50	44.12
KCH-19	4	7b	41.57	9.28	41.26	7.88	45.13	10.08	44.79
KCH-19	4	8b	43.04	9.29	39.83	7.85	46.70	10.08	43.22
KCH-19	4	9b	41.96	9.11	41.67	7.26	45.24	9.83	44.93
KCH-19	4	10b	42.68	8.72	41.48	7.12	45.95	9.39	44.66
KCH-19	4	11b	42.76	8.77	41.58	6.89	45.92	9.42	44.66
KCH-19	4	12b	41.77	8.68	42.21	7.34	45.08	9.36	45.56

36.6 to 48.6 mol. % enstatite ( $MgSiO_3$ ), 7.7 to 18.3 mol. % ferrosilite ( $FeSiO_3$ ), and 41.7 to 47.4 mol. % wollastonite ( $CaSiO_3$ ), all of which fall into the diopside or augite compositions (Figure 7, data in Appendix C). The complex zonations observed make the pyroxenes impractical for thermobarometric analysis (e.g., Putirka papers).

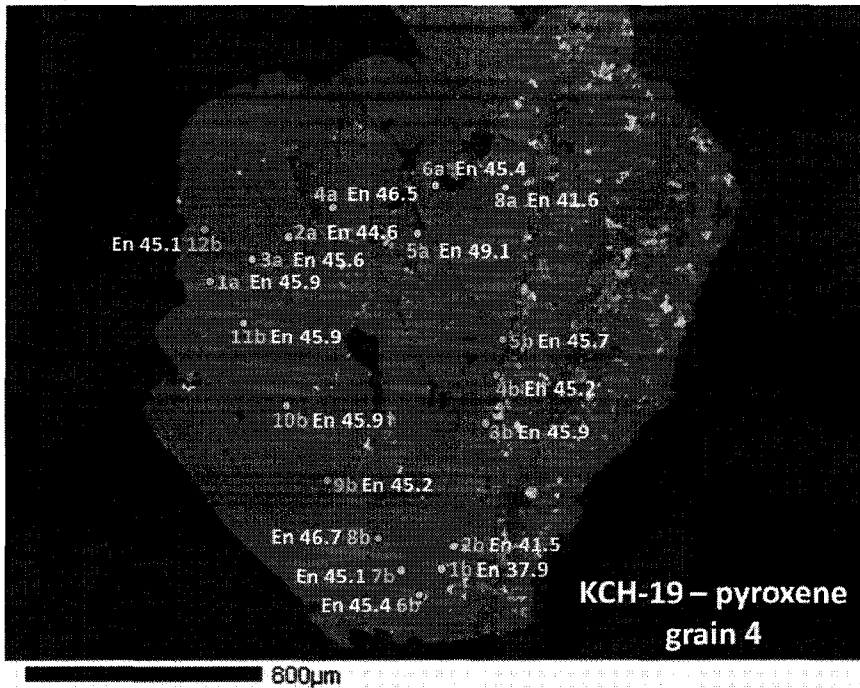


**Figure 6:** Example microphotograph of pyroxene #4 of KCH-19. Microphotographs of all pyroxenes analyzed are in Appendix C. The yellow points show transect "a" analyzed, and the orange points show transect "b" analyzed (Table 3). The re-normalized enstatite end-member composition is shown for each point as an example of how the composition changes spatially. For complete compositions see Table 3 and/or Appendix C.

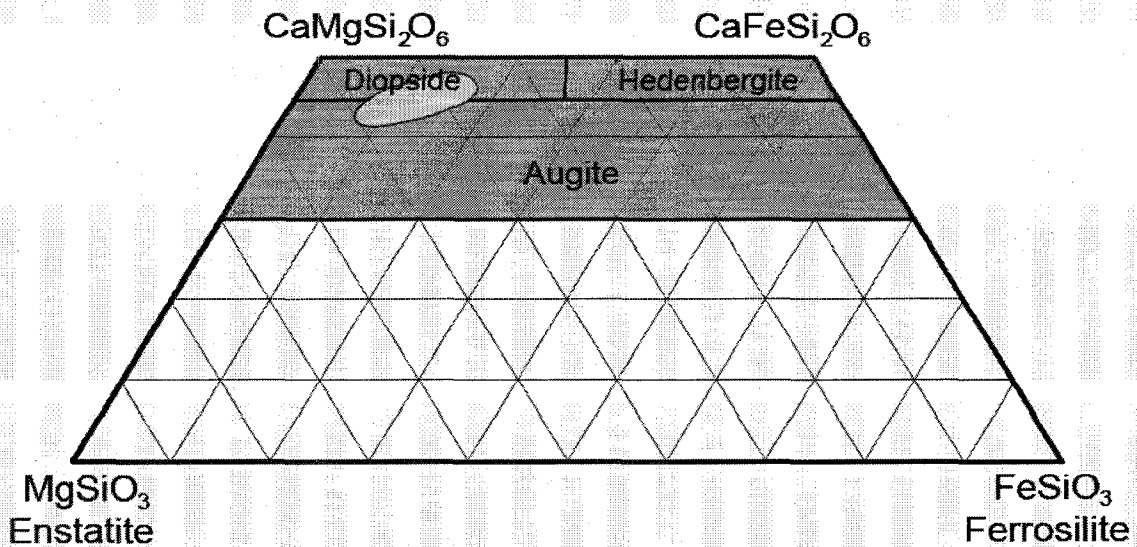


**Figure 7:** Normalized clinopyroxene compositions of Quaternary and Tertiary Turkana lavas (shown in the light blue oval), using classification of pyroxenes from Morimoto (1988). The diopside, hedenbergite, and augite compositions are shown in grey.

## CHAPTER III

### METHODS

Sixteen Quaternary and eleven Tertiary mafic basalts were selected from T. Furman's collection at Pennsylvania State University. Nearly all of the samples chosen for this study have trace and major element datasets from previous work by Furman et al. (2004, 2006a), and many of the samples have been characterized for Sr-Nd and/or Pb isotopic compositions (Curtis, 1991 and Furman et al., 2004, 2006a). This study measured Hf isotope ratios of twenty-two samples, the other five samples were measured by T. Rooney at San Diego State University (Table 4). When necessary to complete the dataset, Sr, Nd and/or high precision Pb analyses were undertaken (Table 4). Several samples with previous data were reanalyzed to assess the reproducibility amongst the separate datasets.

The samples were crushed to <100  $\mu\text{m}$  chips in a stainless steel mortar and pestle. Clean chips were picked out for analysis and leached first in dilute HCl and then in dilute HBr. The chips were then digested via processing with a HF-HNO<sub>3</sub> mixture, and then HNO<sub>3</sub> and HCl were used to drive off fluoride precipitates. Sr, Nd, Pb, and Hf were isolated via ion exchange chromatography. Clean olivine phenocrysts were picked from the crushed samples and sent to D. Graham at Oregon State University for helium isotopic analyses. Complete procedures of sample preparation, dissolution, and element separations by ion exchange chromatography are reported in Appendix D.

**Table 4:**

Measured isotopic compositions of Quaternary and Tertiary Turkana lavas. \* From T. Rooney et al., unpublished data. † From Furman et al. 2006 analyzed by D. Graham.

**MEASURED VALUES:**

<b>Quaternary:</b>							
Sample	$^{176}\text{Hf}/^{177}\text{Hf}$	$^{143}\text{Nd}/^{144}\text{Nd}$	$^{87}\text{Sr}/^{86}\text{Sr}$	$^{208}\text{Pb}/^{204}\text{Pb}$	$^{207}\text{Pb}/^{204}\text{Pb}$	$^{206}\text{Pb}/^{204}\text{Pb}$	R/Ra
BR-05	0.283028	0.512905	0.703276	39.2030	15.5992	19.3815	
BR-33	0.283017	0.512913	0.703280	39.2773	15.5977	19.4672	
CI-08B	0.283035	-	-	-	-	-	
CI-09B	0.283035	-	-	-	-	-	
CI-10A	0.283020	-	-	-	-	-	
CI-31	0.283028*	-	-	-	-	-	
CI-32	0.283032	-	-	-	-	-	
KCH-16	0.283034	0.512919	-	39.0025	15.5792	19.2188	
KCH-19	0.283034	0.512929	0.703092	39.3062	15.6106	19.4932	
SI-15	0.283022*	-	-	-	-	-	
SI-20B	0.283024	-	-	-	-	-	6.45
SI-24	0.283029*	-	-	-	-	-	
LGP 92-11	0.283006	0.512900	0.703156	39.2479	15.6126	19.4458	2.89
LGP 607	0.283006	-	-	39.0933	15.5953	19.3006	
LGP 36	0.283005	-	-	39.0985	15.5891	19.3213	
LGP 39	0.282985	-	-	39.0613	15.5972	19.2699	

<b>Tertiary:</b>							
Sample	$^{176}\text{Hf}/^{177}\text{Hf}$	$^{143}\text{Nd}/^{144}\text{Nd}$	$^{87}\text{Sr}/^{86}\text{Sr}$	$^{208}\text{Pb}/^{204}\text{Pb}$	$^{207}\text{Pb}/^{204}\text{Pb}$	$^{206}\text{Pb}/^{204}\text{Pb}$	R/Ra
KJ 1	0.282926	-	-	40.0599	15.7481	20.5117	
KJ 16	0.282964	-	-	38.6912	15.5846	18.9425	
LOR 86-23B	0.282910	0.512716	0.703767	38.2183	15.5588	18.4609	
KL 18	0.282798	-	-	39.8228	15.7623	19.9212	
JRG 03	0.282894	0.512821	0.703119	40.0632	15.7308	20.4508	
JRG 07	0.282881	-	-	-	-	-	6.26 <sup>†</sup>
JRG 10	0.282889	-	-	-	-	-	6.59 <sup>†</sup>
JRG 12	0.282862*	-	-	-	-	-	6.15 <sup>†</sup>
PORR 404	0.282930*	-	-	-	-	-	
PORR 602	0.282950	-	-	39.9404	15.6822	20.1066	
PORR 606	0.282922	-	-	40.0904	15.7175	20.4943	

Nd, Pb, and Hf isotopes were measured on the Nu Plasma 1700 multicollector inductively coupled plasma mass spectrometer (MC-ICP-MS) in the Baylor Brooks Institute for Isotope Geology in the Department of Geological Sciences at San Diego State University (Table 4). The TI-doping technique was

used to correct the standards isotopic values for Pb analyses using NIST SRM 997 Tl (White et al., 2000; and Albarède et al., 2004) and  $^{205}\text{Tl}/^{203}\text{Tl} = 2.3889$  (Thirlwall, 2002). Within-run fractionation of sample isotopic values was corrected by using standard-sample-standard bracketing and a delta correction using NIST SRM 981 Pb and values from Todt et al. (1996). The NIST SRM 981 Pb standard was run seven times throughout the fifteen samples run, the averages of the measurements are  $^{206}\text{Pb}/^{204}\text{Pb} = 17.238 \pm 0.002$ ,  $^{207}\text{Pb}/^{204}\text{Pb} = 15.906 \pm 0.002$ , and  $^{208}\text{Pb}/^{204}\text{Pb} = 38.013 \pm 0.007$ . The Tl-corrected NIST SRM 981 Pb standard measured averages are  $^{206}\text{Pb}/^{204}\text{Pb} = 16.9417 \pm 0.0008$ ,  $^{207}\text{Pb}/^{204}\text{Pb} = 15.4984 \pm 0.0008$ , and  $^{208}\text{Pb}/^{204}\text{Pb} = 36.7217 \pm 0.0029$ . For a complete list of standard measurements and averages see Appendix E.

Nd and Hf isotopic measurements were corrected for instrument drift using standard-sample-standard bracketing. The AMES Nd standard, run eight times, averaged  $^{143}\text{Nd}/^{144}\text{Nd} = 0.512111 \pm 0.000005$ . A La Jolla standard was measured between standards with a corrected value of  $^{143}\text{Nd}/^{144}\text{Nd} = 0.511840 \pm 0.000003$ . Within run fractionation was corrected for using  $^{146}\text{Nd}/^{144}\text{Nd} = 0.7219$ . The JMC 475 Hf standard was measured twenty-two times, throughout the analyses, and averaged  $^{176}\text{Hf}/^{177}\text{Hf} = 0.282141 \pm 0.000002$ . The  $\epsilon_{\text{Nd}}$  and  $\epsilon_{\text{Hf}}$  values were calculated using the chondritic uniform reservoir (CHUR) values of  $^{143}\text{Nd}/^{144}\text{Nd} = 0.512638$  and  $^{176}\text{Hf}/^{177}\text{Hf} = 0.282772$ .

Sr isotopic values, reported in Table 4, were measured with a VG Sector 54 thermal ionization mass spectrometer (TIMS) at San Diego State University. The Sr isotopic values were corrected for fractionation using the NIST SRM 987



Sr standard. The standard, run eleven times, averaged  $^{87}\text{Sr}/^{86}\text{Sr} = 0.710237 \pm 0.000005$ . For consistency between other datasets, data reported in Table 4 are normalized to 0.710250.

The initial Pb and Hf isotopic values were calculated for samples older than 1 Ma (Table 5) using U-Th-Pb and Lu-Hf concentrations from Furman et al. (2004 & 2006). Three samples (LGP 92-11, LOR 86-23B, and JRG-03) do not have trace element data or ages; therefore initial values were not calculated. However the difference between the initial versus measured values are not significant for other similar samples, and therefore the measured values are used for diagrams and discussion. The only three samples older than 1 Ma and analyzed for Sr and Nd isotope ratios are the same three samples (LGP 92-11, LOR 86-23B, and JRG-03) with no trace element concentrations or ages, thus measured values are used for Sr and Nd ratio values in diagrams and discussion.

**Table 5:**  
Age corrected isotopic compositions of Quaternary and Tertiary Turkana lavas.

**AGE CORRECTED VALUES:**

<b>Quaternary:</b>				
Sample	$^{176}\text{Hf}/^{177}\text{Hf}$	$^{206}\text{Pb}/^{204}\text{Pb}$	$^{207}\text{Pb}/^{204}\text{Pb}$	$^{208}\text{Pb}/^{204}\text{Pb}$
LGP 607	0.283006	38.87	15.59	19.29
LGP 36	0.283005	38.91	15.59	19.31
LGP 39	0.282984	38.89	15.60	19.26

<b>Tertiary:</b>				
Sample	$^{176}\text{Hf}/^{177}\text{Hf}$	$^{206}\text{Pb}/^{204}\text{Pb}$	$^{207}\text{Pb}/^{204}\text{Pb}$	$^{208}\text{Pb}/^{204}\text{Pb}$
KJ 1	0.282921	39.56	15.75	20.33
KJ 16	0.282958	38.56	15.58	18.79
KL 18	0.282796	39.72	15.77	19.92
JRG 07	0.282878	-	-	-
JRG 10	0.282885	-	-	-
JRG 12	0.282858	-	-	-
PORR 404	0.282924	-	-	-
PORR 602	0.282945	39.77	15.68	19.96
PORR 606	0.282917	39.90	15.72	20.29

## CHAPTER IV

### RESULTS AND DISCUSSION

#### Source Contributions and Temporal Constraints

Hafnium isotopic concentrations of the Turkana lavas examined in this study are radiogenic, with  $\epsilon_{\text{Hf}}$  ranging from enrichments of +1.0 to +9.5 when compared with the chondritic reservoir. When evaluated with  $^{206}\text{Pb}/^{204}\text{Pb}$ ,  $\epsilon_{\text{Hf}}$  data reveal two distinct mixing trends (Figure 8a,b). One trend includes the Quaternary samples clustered at high  $\epsilon_{\text{Hf}}$  values (between 7 and 9.5) and mid-range  $^{206}\text{Pb}/^{204}\text{Pb}$  values (about 19.5), with two Tertiary samples at lower  $\epsilon_{\text{Hf}}$  (6.5 and 5) and lower  $^{206}\text{Pb}/^{204}\text{Pb}$  (18.75 and 18.5) values that trend towards the Quaternary compositions. The Quaternary samples with mid-range  $^{206}\text{Pb}/^{204}\text{Pb}$  compositions have isotopic compositions similar to a C-component composition; accordingly, the two Tertiary samples and the Quaternary samples in this group will be referred to as the “C Trend” throughout the rest of this discussion. The remaining Tertiary samples form a separate mixing trend that extends from low up to mid-range  $\epsilon_{\text{Hf}}$  (1 to 6) and mid-range up to radiogenic  $^{206}\text{Pb}/^{204}\text{Pb}$  values (about 19.9 to 20.5). The Tertiary lavas with the high  $^{206}\text{Pb}/^{204}\text{Pb}$  compositions are similar to, or approach, a HIMU-like component. Accordingly, these Tertiary samples will be called the “HIMU Trend” throughout the rest of this discussion.

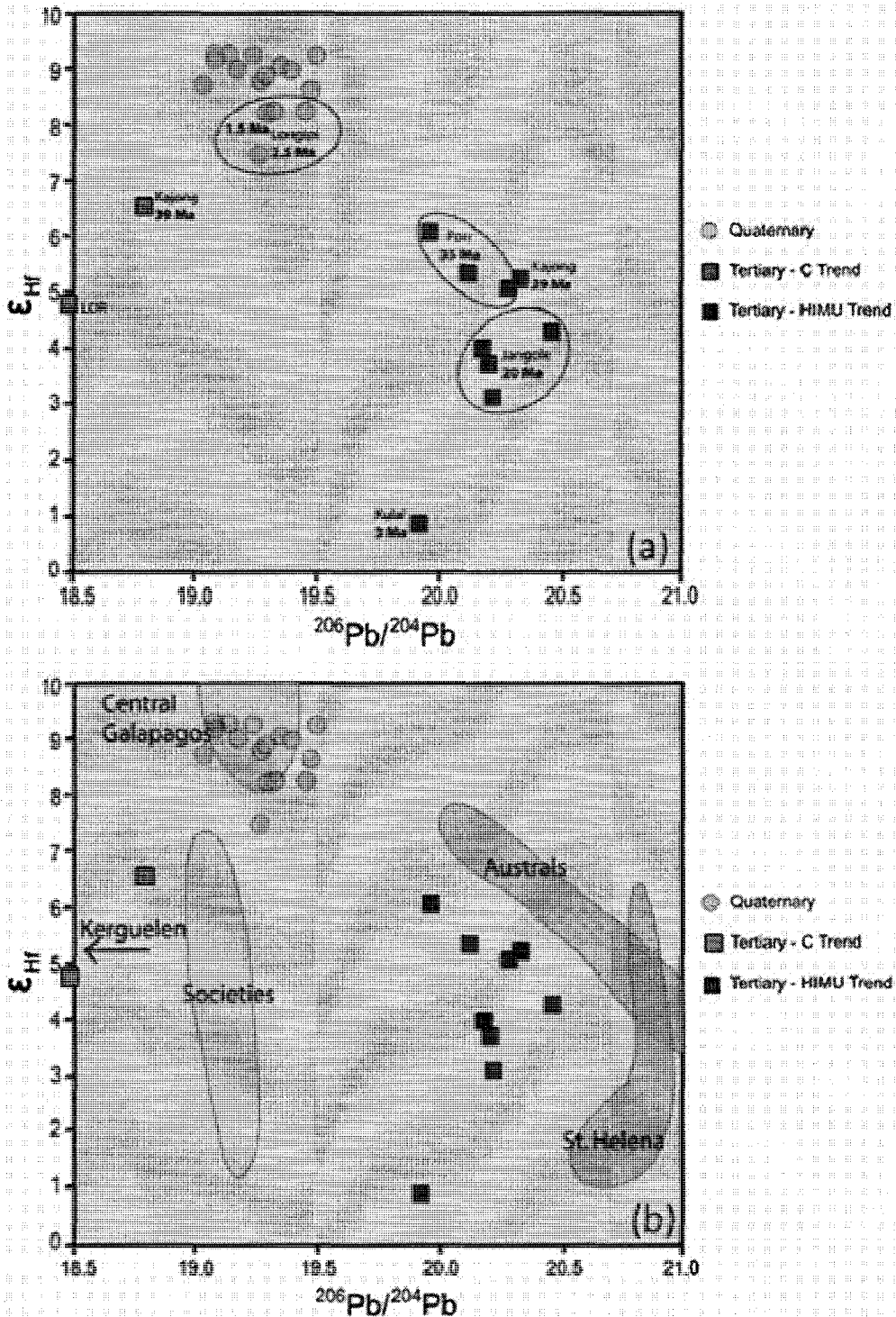


**Figure 8:**

$\epsilon_{Hf}$  versus  $^{206}Pb/^{204}Pb$  with age correlations in Turkana (a) and with Turkana related to world wide OIB data (b). Light blue circles represent Quaternary lavas, the blue and red squares represent Tertiary lavas. Galapagos field data are from Blichert-Toft & White (2001), all other OIB field data are from Salters & White (1998) and Chauvel & Blichert-Toft (2001).

In Pb-Hf space two temporal trends for the two mixing lines are observed (Figure 8a), the older Tertiary C Trend samples have lower  $\epsilon_{\text{Hf}}$  and Pb isotope values than the Quaternary (note: LOR 86-23B has an unknown age, it is also commonly an outlier in other isotopic compositions) and the older Quaternary samples have lower  $\epsilon_{\text{Hf}}$  than the younger Quaternary samples. The HIMU Trend has an age correlation in the opposite direction of the C Trend and Quaternary samples. The oldest HIMU Trend samples have the highest  $\epsilon_{\text{Hf}}$  and Pb isotope values and the youngest have the lowest  $\epsilon_{\text{Hf}}$  and Pb isotope values.

Examination of Turkana Quaternary and Tertiary Hf-Pb relationships in comparison with ocean island basalt (OIB) fields further support interpretations of magma sources (Figure 8b). The comparison reveals an overlap of the Quaternary samples with the central Galapagos, plume-related basalts interpreted to result from a source region rich in C-component (Blichert-Toft & White, 2001). Turkana C Trend samples fall in a group overlapping the Central Galapagos compositions and trend towards the Societies. The Turkana HIMU Trend, on the other hand, is offset from the Australs and St. Helena suites, both of which are interpreted to be associated with a HIMU mantle source (Hemond et al., 1994; and Ballentine et al., 1997).

The Quaternary and Tertiary Turkana Hf data and Nd isotopic compositions are positively correlated (Figure 9a,b). This relationship is commonly seen in mantle-derived basalts and is inferred to result from both Lu and Sm being incompatible elements. The incompatibility leads to partial melts of the mantle enriched in Lu and Sm compared to Hf and Nd, resulting in more

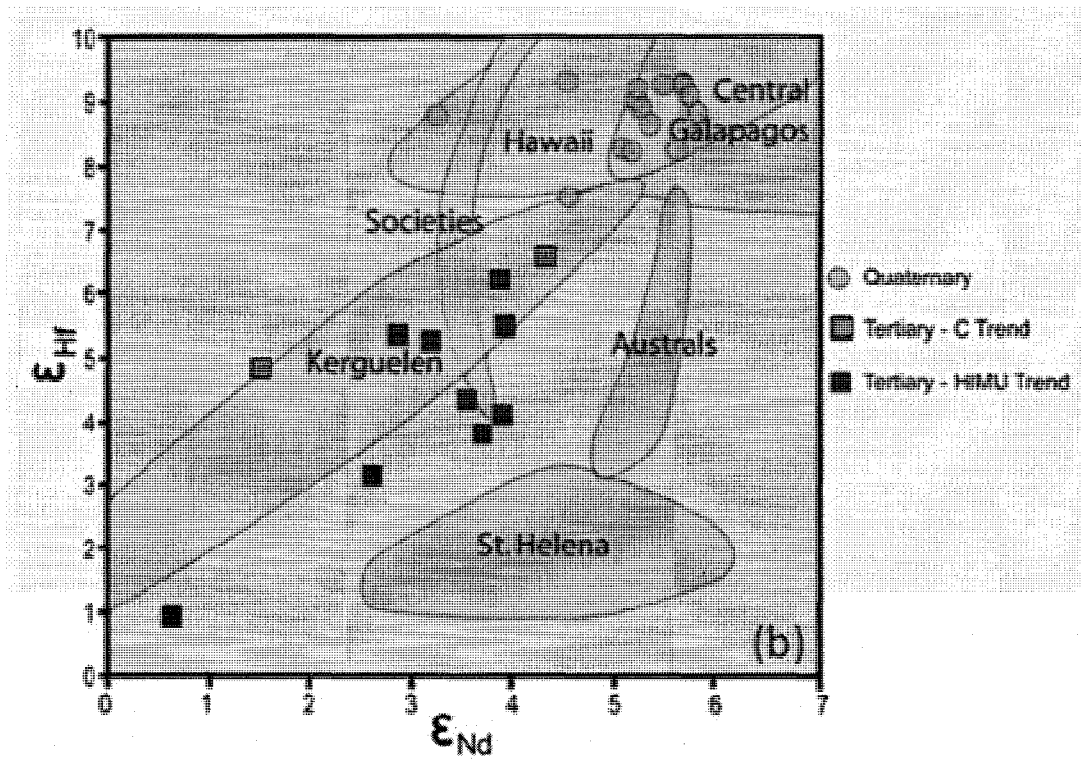
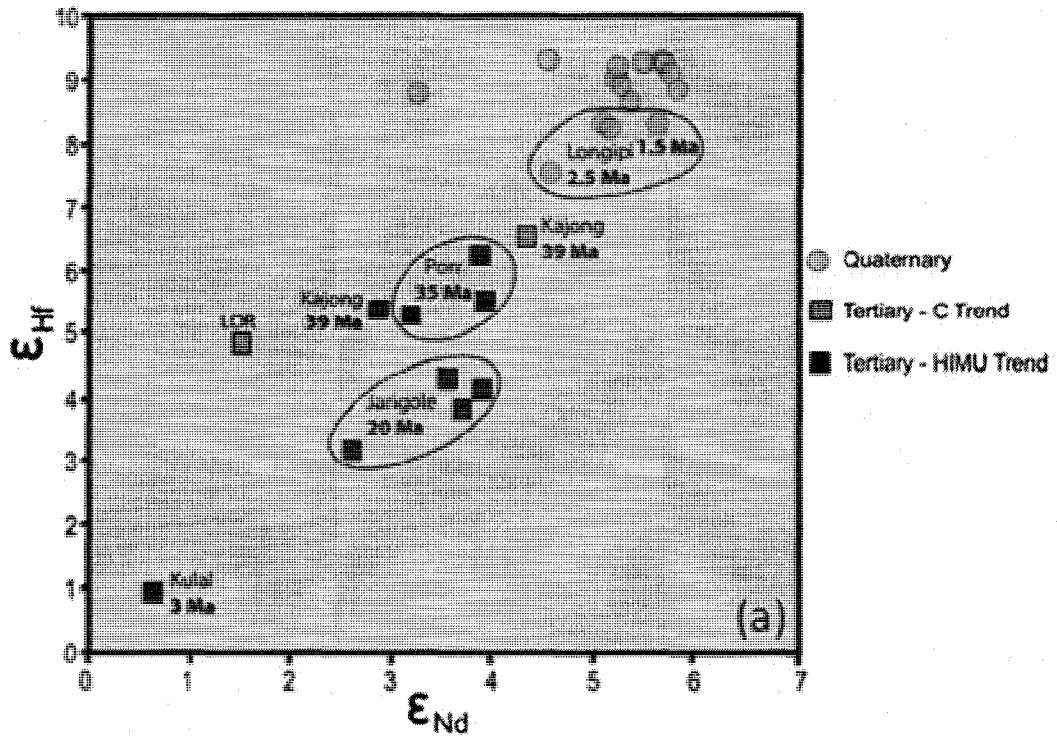


**Figure 9:**

$\epsilon_{\text{Hf}}$  versus  $\epsilon_{\text{Nd}}$  with age correlations in Turkana (a) and with Turkana related to world wide OIB data (b). Symbols and referenced datasets as in Figure 8.

isotopic compositions of Hf and Nd. Quaternary lavas are clustered with high radiogenic values, while the Tertiary samples have a much wider range. In Hf-Nd compositional space the temporal relationships are apparent within each trend, with the older samples more depleted and the younger samples more enriched (Figure 9a).

Figure 9b provides a comparison of  $\epsilon_{Nd}$  versus  $\epsilon_{Hf}$  for the Turkana Tertiary and Quaternary lavas with OIB fields. Again the Quaternary samples overlap the central Galapagos and the C Trend samples trend toward the central Galapagos field and overlap the Kerguelen field. The HIMU Trend is near and/or overlaps Kerguelen, the Australs, and St. Helena.

Turkana Hf and Sr isotopic data demonstrate a weak negative correlation (Figure 10a,b). As noted above with Hf-Pb relationships, Hf-Sr characteristics of the Quaternary "C-Trending" samples overlap with the Central Galapagos samples and have less radiogenic Sr values than the Kerguelen field. The Hf-Sr signatures in the HIMU Trend Turkana samples approach those documented in the Australs and St. Helena fields (with the exception of KL-18 from Kulal). The clearly distinctive Sr isotopic signature of the Kerguelen group when compared to the Turkana lavas imply that the source regions responsible for the volcanism in these two distinct geographic areas represent two different time-integrated histories of formation. The nonradiogenic Sr signatures in Turkana imply that, unlike in the case of Kerguelen, Turkana lavas are not representative of recycled continental lithosphere (Mattielli et al., 2002).

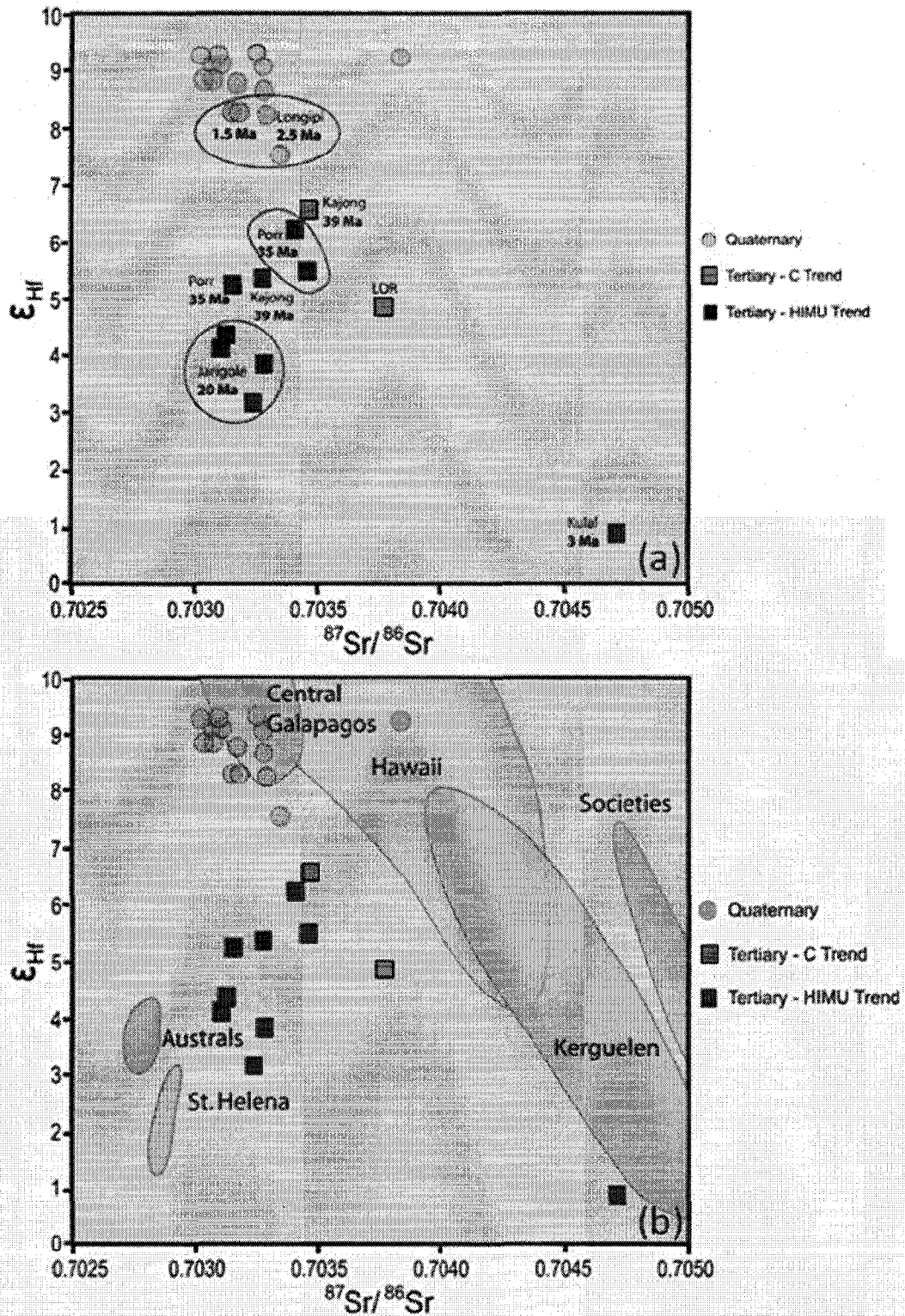


**Figure 10:**  $\epsilon_{Hf}$  versus  $^{87}Sr/^{86}Sr$  with age correlations in Turkana (a) and with Turkana related to world wide OIB data (b). Symbols and referenced datasets as in Figure 8.

New Pb and Nd isotope ratios of Quaternary and Tertiary Turkana basalts complement the dataset reported by Furman et al. (2004, 2006a). Pb-Nd isotopic relationships also identify two distinct trends, following the same grouping of samples that is evident in the Pb-Hf relationships (Figure 11). As with the Hf-Pb relationships, the Quaternary samples cluster together in Pb-Nd composition near the C-component field with the two Tertiary values forming the C Trend mixing line. The HIMU trend form a mixing line that approaches the HIMU field as defined by Stracke et al. (2005). Relationships between the Pb isotopic signatures provide similar results as Pb-Nd isotopic data (Figures 12 and 13), though with the consideration of Pb alone, it is more difficult to distinguish the C Trending Turkana samples from those trending towards HIMU.

### **Regional Recurrence of Isotopic Signatures Observed in Turkana**

Consideration of other regions within the EARS with the Turkana Pb and Nd isotope ratios reveals that the two mixing trends may be more extensive throughout the EARS (Figures 14, 15, and 16). Some regions trend towards the C-component field similar to the Quaternary samples and C Trend, while other regions trend towards the HIMU field similar to the HIMU Trend. The Turkana C Trend and Quaternary samples overlap with MER and partially overlap with the Afar Depression. The Turkana HIMU Trend samples overlap with the South MER and the North Kenya Rift.



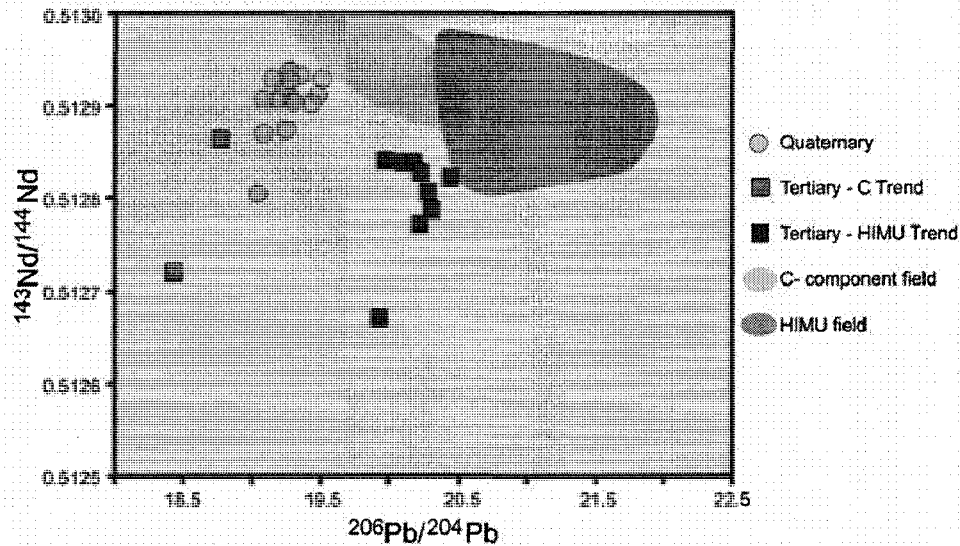


**Figure 11:**  $^{206}\text{Pb}/^{204}\text{Pb}$  versus  $^{143}\text{Nd}/^{144}\text{Nd}$  with Turkana lavas related to C-component (the light blue field) and HIMU type (the red field) compositions. Symbols are same as in Figure 8. The Quaternary lavas with the C Trend Tertiary lavas form a mixing line with a C-component end member and the HIMU Trend Tertiary lavas form a separate mixing line with a HIMU like end member. Some data points from Furman et al. (2004, 2006a) (Tables 4 and 5). C-component and HIMU fields are modified from Stracke et al. (2005).

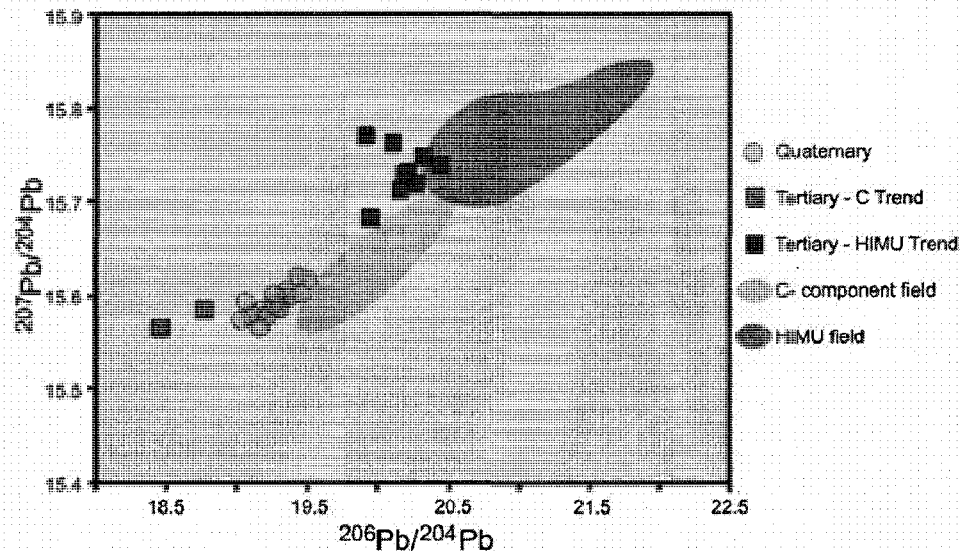


**Figure 12:**  $^{206}\text{Pb}/^{204}\text{Pb}$  versus  $^{207}\text{Pb}/^{204}\text{Pb}$  with Turkana lavas related to C-component and HIMU type compositions. Symbols are same as in Figure 8. Referenced data are as in Figure 11. The Quaternary lavas with the C Trend Tertiary lavas form a mixing line with a C-component end-member, and the HIMU Trend Tertiary lavas have a HIMU like component.

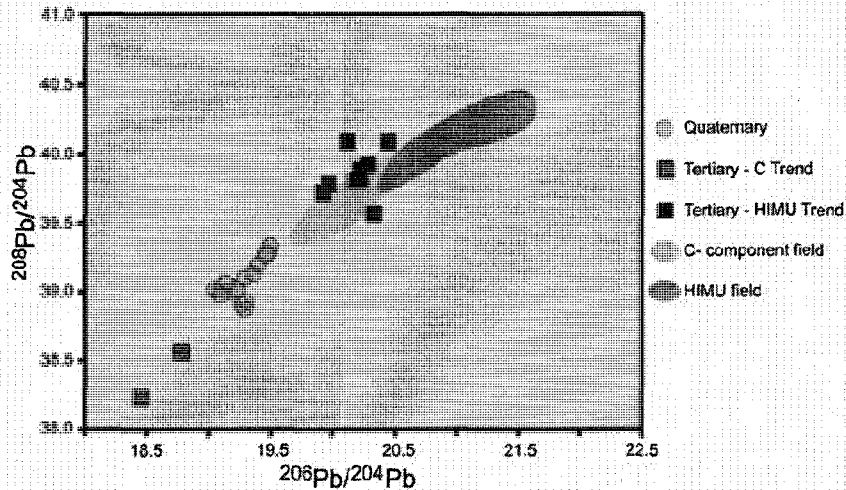


**Figure 13:**  $^{206}\text{Pb}/^{204}\text{Pb}$  versus  $^{208}\text{Pb}/^{204}\text{Pb}$  with Turkana lavas related to C-component and HIMU type compositions. Symbols are same as in Figure 8. Referenced data are as in Figure 11. The Quaternary lavas with the C Trend Tertiary lavas form a mixing line with a C-component end-member, and the HIMU Trend Tertiary lavas have a HIMU like component.

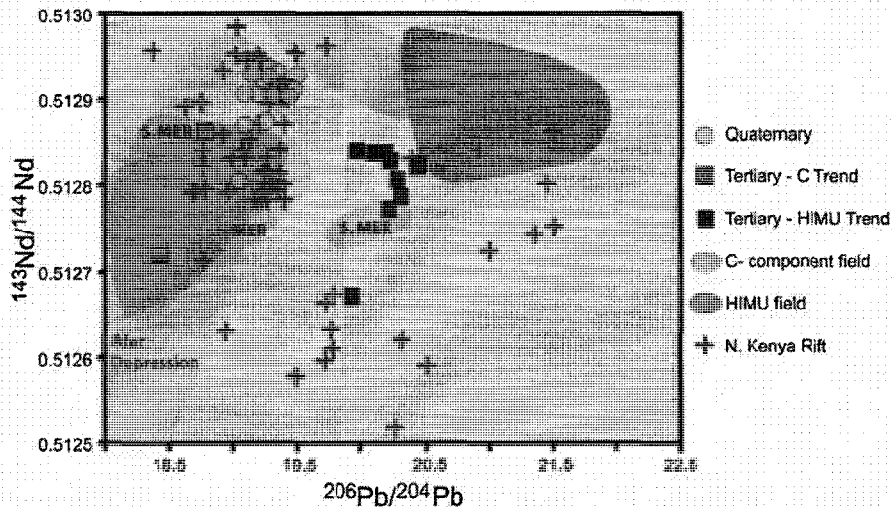


**Figure 14:**  $^{206}\text{Pb}/^{204}\text{Pb}$  versus  $^{143}\text{Nd}/^{144}\text{Nd}$  with Turkana lavas related to other EARS regional data. The Quaternary and C Trend Tertiary Turkana lavas have similar compositions to the Afar Depression and the Main Ethiopian Rift (MER) and the HIMU Trend Tertiary Turkana lavas have a similar composition to the North Kenya Rift. Some Turkana data points from Furman et al. (2004, 2006a). HIMU and C-component fields after Stracke et al. (2005). Afar Depression field data are from Barrat et al. (1998), Betton & Civetta (1984), Deniel et al. (1994), Hart et al. (1989), and Vidal et al. (1991). MER field data are from Furman et al. (2006), Hart et al. (1989), Peccerillo et al. (2003), Stewart & Rogers (1996), and Trua et al. (1999). Southern MER field data are from George & Rogers (1999), and Stewart & Rogers (1996). Northern Kenya Rift field data are from Bell & Doyle (1971), Class et al. (1994), Clément et al. (2003), MacDonald et al. (1995), Norry et al. (1980), Rogers et al. (2000), Rogers et al. (2006), Simonetti & Bell (1994), and Simonetti & Bell (1995).

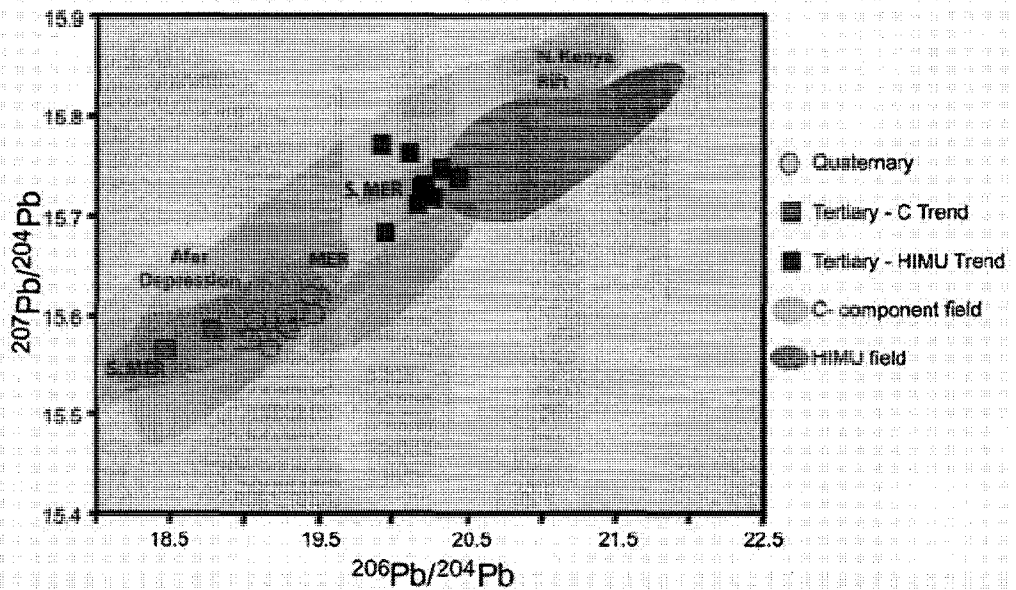


**Figure 15:**

$^{206}\text{Pb}/^{204}\text{Pb}$  versus  $^{207}\text{Pb}/^{204}\text{Pb}$  with Turkana lavas related to other EARS regional data. The Quaternary and C Trend Tertiary Turkana lavas have similar compositions to the Afar Depression and the Main Ethiopian Rift (MER), and the HIMU Trend Tertiary Turkana lavas have a similar composition to the North Kenya Rift. Symbols and referenced data are as in Figure 14.

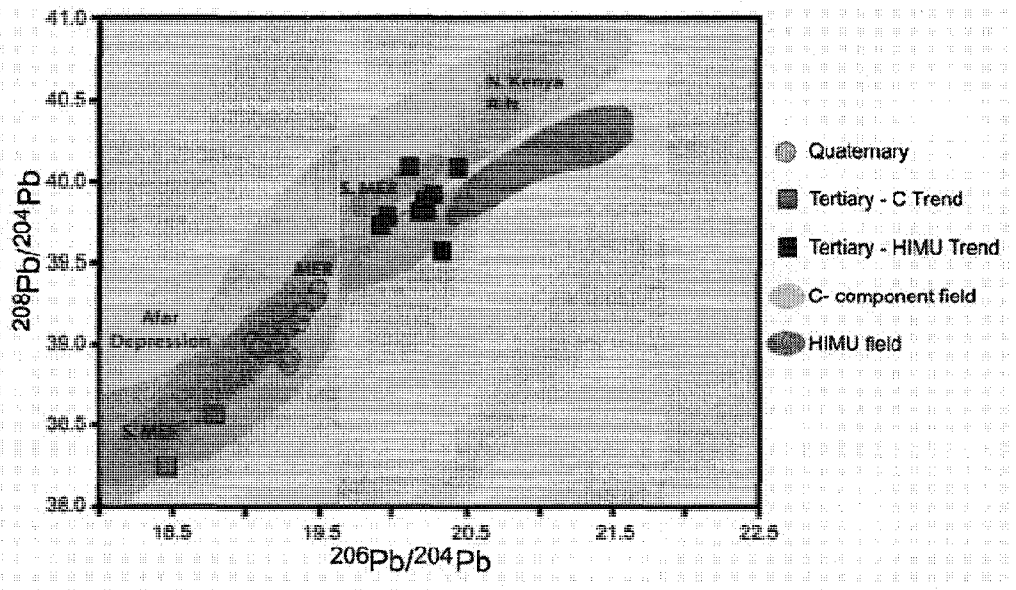


**Figure 16:**

$^{206}\text{Pb}/^{204}\text{Pb}$  versus  $^{208}\text{Pb}/^{204}\text{Pb}$  with Turkana lavas related to other EARS regional data. The Quaternary and C Trend Tertiary Turkana lavas have similar compositions to the Afar Depression and the Main Ethiopian Rift (MER), and the HIMU Trend Tertiary Turkana lavas have a similar composition to the North Kenya Rift. Symbols and referenced data are as in Figure 14.

Mt. Elgon and Napak samples from the North Kenya Rift are extremely alkaline in composition, dominantly nephelinites and carbonatites (Simonetti & Bell, 1994, 1995), and are in close proximity to the Turkana depression. They also have the most similar Nd-Pb composition to the Turkana Tertiary HIMU Trend samples (Figure 17). Lavas from Mt. Elgon and Napak have been interpreted to be from small discrete melts from heterogeneous subcontinental lithosphere with one end-member being HIMU in composition and the opposite end-member being EM1 in composition (Simonetti & Bell, 1994, 1995). The Turkana Tertiary HIMU Trend, being in the same vicinity of the Mt. Elgon and Napak mixing line compositions, can be interpreted to have the same two compositional end-members.

The EM1 component also becomes apparent in Pb-Sr isotopic compositions (Figure 18). The HIMU Trend samples with less radiogenic compositions trend toward the EM1 composition, opposite the more radiogenic Pb end-member HIMU, implying an EM1-like material plays a role as an end-member composition. KL-18 from Kulal lies off the trend line with a high Sr isotope value; this sample is commonly an outlier in other compositions which is likely due to it being from a very small degree of melt from a heterogeneous source. The Pb-Sr compositions also indicate the opposite end-member of the C Trend. The Quaternary data again have a C-component, OIB like, composition while the Tertiary C Trend data trend toward the same EM1 end-member as is being mixed in the HIMU Trend.

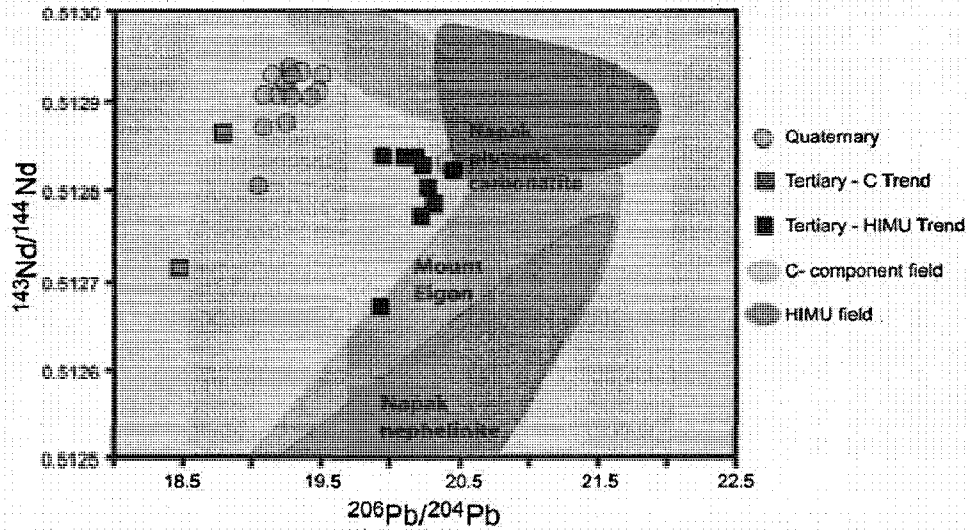


**Figure 17:**

$^{206}\text{Pb}/^{204}\text{Pb}$  versus  $^{143}\text{Nd}/^{144}\text{Nd}$  with Turkana lavas related to regional data from North Kenya Rift. The HIMU Trend Tertiary Turkana lavas have a very similar mixing line (though not as extensive) as the Mt. Elgon and Napak lavas. Some data points from Furman et al. (2004 & 2006). HIMU and C- component fields modified from Stracke et al. (2005). Mt. Elgon field data are from Simonetti & Bell (1995) and Napak field data are from Simonetti & Bell (1994).

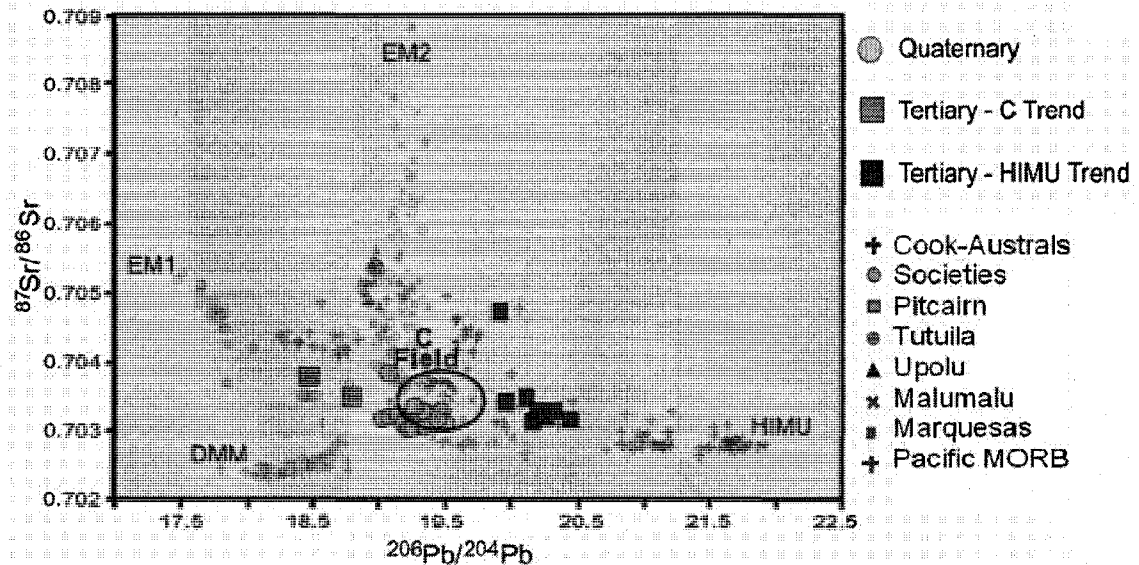


**Figure 18:**

$^{206}\text{Pb}/^{204}\text{Pb}$  versus  $^{87}\text{Sr}/^{86}\text{Sr}$  with Turkana lavas related to OIB and MORB compositions. The HIMU Trend forms a mixing line between a HIMU like end member and an EM1 like end member, and the C Trend forms a mixing line between a C-component end member and an EM1 like end member. OIB and MORB after Workman et al. (2004) & Bizimis et al. (2003), including datasets from Chauvel et al. (1992, 1997), Hauri & Hart (1993), Nakamura & Tatsumoto (1988), Palacz & Saunders (1986), Vidal et al. (1984), and Stracke et al. (2003). C-component field after Hanan & Graham (1996).

The two distinct temporal trends observed with the new Hf isotopic data coupled with source compositions interpreted from Pb, Nd, and Sr, isotopic data provides a compositional timeline for the Turkana region of the EARS. The C Trend and Quaternary samples over time go from EM1 composition to OIB C-composition. The HIMU Trend over time goes from HIMU to EM1. The disparate trends in Pb-Hf with respect to time suggest that the source mixtures for the two groups of lavas are distinct. It is important to note the two Kajole samples; they have the same age and are from the same location, yet fall on the two different trends (Figure 8). This can be explained best by one Kajole sample being from of the heterogeneous plume/polluted mantle (KJ-16 in the C Trend) and the other is strictly plume composition (KJ-1 in the HIMU Trend).

### **Olivine Compositions and He ( $R/R_A$ ) Data**

Compositions of olivine phenocrysts within the Turkana lavas can be used to infer source region processes. The olivine forsterite and nickel compositions when compared to Sobolev et al. (2005) fields (Figure 19) also reveal possible source lithologies. The cores of the olivines trend towards higher nickel compositions with increased forsterite compositions, this trend is indicative of a pyroxene rich source for the olivine cores (Sobolev et al., 2005). However, these olivine phenocrysts are strongly zoned, and because there are high oxide totals in the rims, the zones are likely a result of magma mixing rather than post eruptive alterations. If magma mixing is a significant process, then the cores of the olivine phenocrysts may not be related to the erupted lavas, especially in the

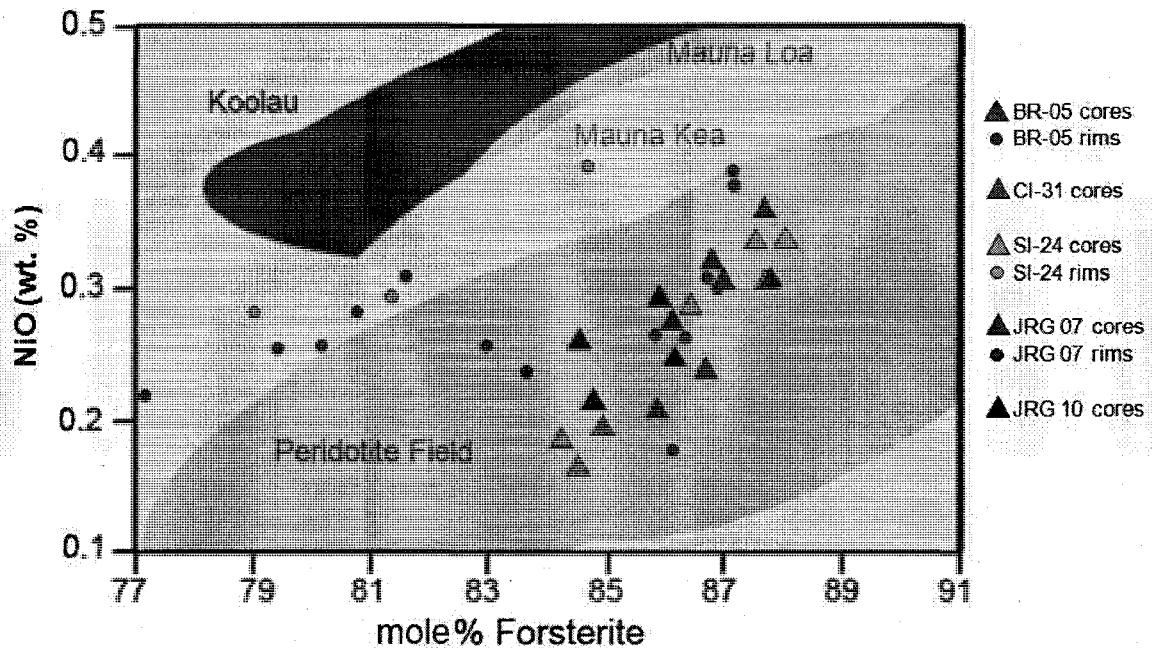


**Figure 19:**

Forsterite composition versus nickel weight percent of Quaternary and Tertiary Turkana lavas compared with peridotite and Hawaiian basalt fields after Sobolev et al. (2005). The "Peridotite Field" is a combination of peridotites from mantle xenoliths, orogenic massifs and ophiolites, oceanic abyssal peridotites, and phenocrysts from MORBS (Sobolev et al., 2005).

Jarigole picrites where there is already evidence for olivine accumulation. However, there is further evidence of a pyroxene rich source in several of the olivine rims (specifically SI-24 and JRG 07), which also have high nickel concentrations with respect to forsterite compositions (Figure 19). The other samples analyzed have rims with lower nickel concentrations relative to forsterite compositions, which are indicative of a peridotite source (Sobolev et al., 2005). This wide range of rim compositions is evidence for mixing of two separate source lithologies, which are likely a peridotite and a pyroxene rich source.

Helium isotopic compositions in olivine crystals from the lavas provide unique information about the mantle source history and the magmatic dynamics.

Of the two isotopes  $^3\text{He}$  and  $^4\text{He}$ ,  $^4\text{He}$  is the most abundant isotope and is primarily produced from the radioactive decay of  $^{238}\text{U}$ ,  $^{235}\text{U}$ , and  $^{232}\text{Th}$ .  $^3\text{He}$  is dominantly primordial and is therefore assumed that all  $^3\text{He}$  found in rocks is from the formation of the Earth (Graham, 2002). Mafic lavas with low relative amounts of  $^3\text{He}$ , or a low value of  $R/R_A$  [where  $R/R_A$  denote the ratio of the sample  $^3\text{He}/^4\text{He}$  to that of the atmosphere, defined as  $1.384 \times 10^{-6}$  (Graham, 2002)], are interpreted to be melting products from degassed sublithospheric mantle or the continental lithosphere with a long residence time (allowing the build of  $^4\text{He}$ ) (Graham, 2002). Lavas with relatively large amounts of  $^3\text{He}$  (a high value of  $R/R_A$ ) are interpreted to have come from a mantle source previously undegassed, therefore likely from a deep mantle source (Graham, 2002). Mid-ocean ridge basalts (MORBs) are fairly homogeneous with an average  $R/R_A$  of about 8 (Allègre et al., 1995; and Graham, 2002). While OIBs have a much more diverse range of ratios between a radiogenic end-member with  $R/R_A = 4$ , and a very un-radiogenic end-member with  $R/R_A = 42.9$  (Kurz et al., 1982a; Kurz et al., 1982b; and Allègre et al., 1995).

Olivine phenocrysts of Tertiary lavas from Jarigole (20 Ma picrites) in the Turkana region have  $R/R_A = 6.15$  to  $6.59$  (Table 4 and Figure 20) which are similar to OIBs that contain HIMU signatures (Moreira & Kurz, 2001). The source of the low  $R/R_A$  signature of HIMU is still controversial, with some articles supporting a recycled oceanic crust (Hanyu & Kaneoka, 1997) and others favoring lithospheric contamination (Hilton et al., 1998). Moreira and Kurz (2001) created a model where the HIMU source incorporates oceanic lithosphere, which



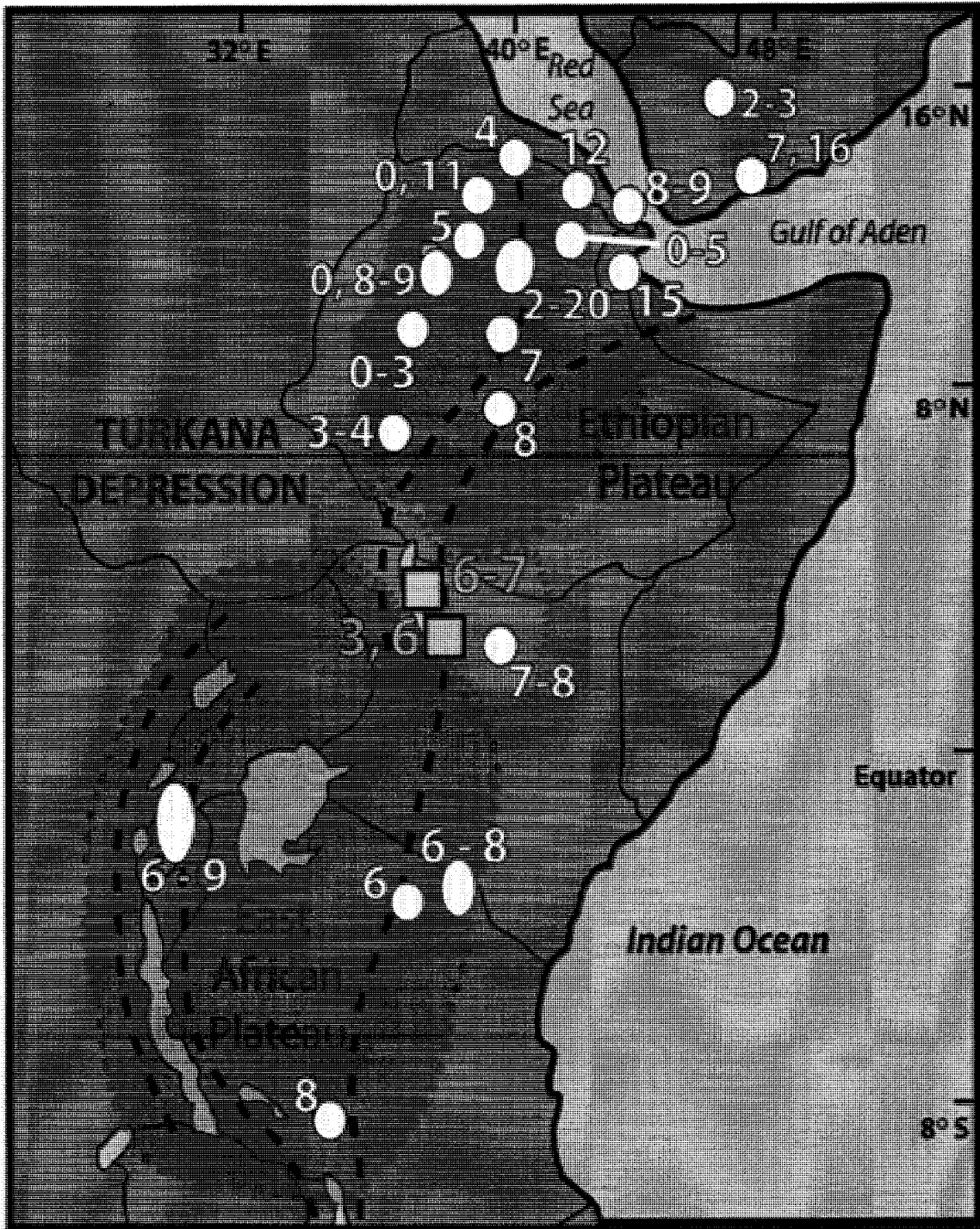


**Figure 20:** Helium isotopic contours within the EARS. New helium analyses from this study depicted by orange squares. Other regional data is from Marty et al. (1996) and Pik et al. (2006). The Ethiopian plateau has R/Ra ranges from less than 1 to 20, the Turkana depression has R/Ra values around 6 to 8, with one sample (LGP 92-11 from Longipi) R/Ra = 3. The East African Plateau has R/Ra values between 6 and 9.

has a very radiogenic component of subducted oceanic crust (with  $^3\text{He}/^4\text{He} = 0.01$ ) and a less radiogenic component of residual lithosphere. The combination of the two components creates the HIMU signature of  $R/R_a = 5 - 7$ . Alternatively, the He isotopic signature of the Jarigole picrites also falls within the range of other He isotopic values for subcontinental lithosphere. Gautheron and Moreira (2002) studied the helium isotopic compositions of alkali basalts and peridotites representing subcontinental lithospheric mantle (from Europe, West Africa, Western US, and Australia) and found them to have homogeneous values with an average of  $R/R_a = 6.1$ . Graham et al. (2007) found the same range of values ( $R/R_a < 7$ ) within a suite of basalts from the Pacific Northwest and interpreted the source to be the subcontinental lithosphere. The model used to explain the homogeneity of the subcontinental lithosphere is an open-system steady-state sub-continental lithosphere, where noble gases are transported via metasomatism through cracks and veins or porous flow (Gautheron & Moreira, 2002).

Class et al. (2005) measured helium isotope ratios of alkali basalts and basanites from Grand Comore and found two end-members dominating the compositions. One compositional end-member was interpreted to be from the lithospheric mantle and the other from a mantle plume. The lithospheric mantle end-member below Grand Comore has an average  $R/R_a = 6.9$ . The helium signature in the lithospheric mantle is interpreted to be from metasomatism from the Kenya plume (the thermal anomaly below Turkana and the Kenya Rift System) by lateral flow. The Kenya plume was determined to have an  $R/R_a = 7.0$

– 7.9 by analyses from Huri Hills, North Kenya (Class et al., 2005). An alternative possibility for the origin of the lithospheric mantle helium signature is infiltration of the oceanic lithosphere during its formation, either through cracks or by porous flow (Halliday et al., 1995; and Class et al., 2005). The mantle plume helium composition has an average of  $R/R_A = 5.2$ , and is interpreted to incorporate recycled oceanic crust (Class et al., 2005).

Helium isotopic compositions alone, especially in Turkana, cannot be used to distinguish between the Moreira and Kurz (2001) model and the scenarios put forth by Gautheron and Moreira (2002) and Graham et al. (2007). The plume activity beneath eastern Africa could have the HIMU source originating from areas of the plume, potentially tapping areas of recycled crust. Alternatively, the plume activity could be preferentially thermally eroding the HIMU composition out from the sub-continental lithosphere by partial melting of the lithosphere.

One Quaternary sample (SI-20B from South Island) has a similar value to the Tertiary with  $R/R_A = 6.45$ ; however this sample has Pb isotopic values similar to C-component, and not a HIMU composition. Another Quaternary sample (LGP 92-11 from Longipi), has a lower, even more radiogenic value of  $R/R_A = 2.89$ . These radiogenic values are consistent with a degassed source region, either from being previously tapped or by metasomatic processes, and possibly longer residence times (Allègre et al., 1995). The helium data used in this study can be further discussed when compared with other regional data (Figure 20). The Main Ethiopian Rift, located at the Ethiopian Plateau, has a very wide range of  $R/R_A$  values from  $<1$  up to 20, this wide range suggests a diverse variety of

magmatic processes must have occurred throughout the region. The lower values are indicative of degassed melts and/or longer residence times below the crust, while higher values are interpreted to be from undegassed mantle which is interpreted to result from contributions from a mantle plume (Marty et al., 1996; Pik et al., 1999; and Pik et al., 2006). To the south, the East African Plateau (comprised of the Western Rift and the Kenya Rift) has a narrower range of compositions that are similar to the Turkana region with  $R/R_a = 6$  to 8, these values are again similar to a HIMU signature.

### **Proposed Model**

The new isotopic trends and end-members, and their relationships with respect to age requires two distinct regions of mixing that do not mix with each other (due to the lack of mixing between the two isotopic trends). The following proposed model takes into account the mixing trends, the age relationships, and the regional data from the other studies discussed above. At 40 Ma the mantle underlying the lithosphere was heterogeneous with a C-component composition and an EM1-like composition (Figure 21). In this model the EM1 material is related to the general upwelling in the area, either from a plume itself, or sublithospheric mantle “polluted” by contributions from the deep mantle because of activity associated with the Afar plume. The subcontinental lithosphere had a HIMU-like component that easily melted out upon heating from below associated with regional activity or potentially the edge of a plume at that time. Within the heterogeneous mantle the EM1-like component preferentially melted out,

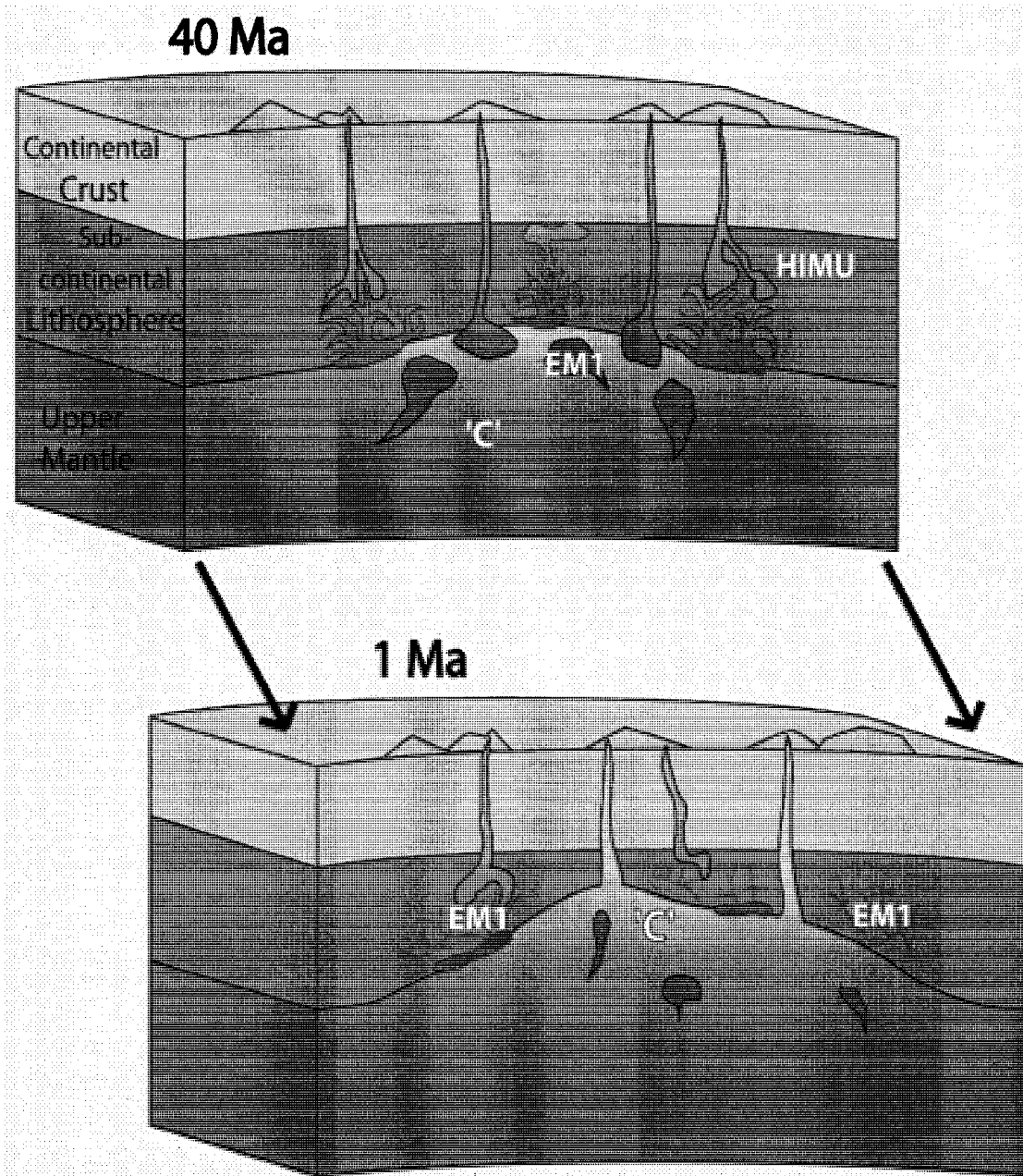


**Figure 21:**

Proposed model for the Turkana region of the EARS. At 40 Ma mantle underlying the lithosphere had a C-component composition and an EM1-like composition. The subcontinental lithosphere had a HIMU-like component that readily melted out. Within the mantle the EM1-like component preferentially melted out and ascended into the lithosphere. This subcontinental lithosphere partially melted due to metasomatic activity and erupted with a dominantly HIMU composition with some mixing of EM1. Also, larger zones of melt in the sublithospheric mantle, representing mixed EM1-C melted out and erupted. Through time, the EM1-rich end member was depleted in the sublithospheric mantle. At the end of the Tertiary, the volcanism reflected primarily sublithospheric contributions of a C-composition.

compared to the C-like component, and ascended into and metasomatized the lithosphere. This subcontinental lithosphere partially melted due to the metasomatic activity and erupted with a dominantly HIMU composition with some mixing of EM1. Alternatively, larger zones of melt in the sublithospheric mantle, representing mixed EM1-C-components melted out at and erupted (e.g., KJ-16). Through time, the EM1-rich end-member was depleted in the sublithospheric mantle, either through mixing with the C-like component and erupting C Trend Tertiary compositions or by metasomatizing the lithosphere.

By 1 Ma much of the EM1-like component had erupted or mixed and metasomatized within the subcontinental lithosphere (Figure 21). At the end of the Tertiary, the resulting volcanism reflected primarily sublithospheric contributions, with the last metasomatized lithospheric sample in our suite at 3 Ma. This model builds on the lithospheric erosion model presented in Furman et al. (2006).

The proposed model requires the EM1-like component to preferentially melt out compared to the C-component in the sublithospheric mantle. Therefore the EM1-like component must have a lithology that more readily melts compared to the surrounding material, such as a pyroxene rich lithology, and possibly a pyroxenite (c.f. e.g., Morgan & Morgan, 1999). The olivine samples from both Quaternary and Tertiary lavas support the concept of at least one pyroxene-rich lithology source that is being melted and erupted in the Turkana region. This is further supported by the EM1 composition being the only component found in both the Quaternary and Tertiary lavas. This idea is similar to the model Morgan

and Morgan (1999) present for the entire mantle, where the mantle as a whole is inhomogeneous with “plums” of pyroxenite type lithologies that preferentially melt out first. The same idea can be applied on a smaller scale to the Turkana region of the EARS (and possibly all of the EARS), where “plums” of pyroxene-rich EM1-type compositions are entrained, and not well mixed, in the upwelling C-component peridotite. It is the EM1 “plums” that metasomatized and partially melt the HIMU composition in the lithospheric mantle. It is also the EM1 “plums” that directly erupt at the surface (without assimilation of the lithosphere) with an EM1-C-component composition, which slowly become more of a C-component over times as the “plums” are depleted.

### **Comparisons to Other Continental Rifts**

The model proposed in this study is similar to other findings and models proposed for several continental rift systems on Earth. A couple examples are the Ross Sea Rift in Antarctica and the Red Sea Rift on the Arabian Plate. The Ross Sea Rift has three mantle sources, EM, HIMU, and depleted MORB-type compositions (Rocholl et al., 1995), that have contributed to the volcanism for at least the past 15 million years. Neither the HIMU nor EM compositions were found to be from continental crust contamination. Comparisons of compositions with the ages of the samples revealed age progressions of EM to HIMU-type signatures, then from HIMU to depleted MORB-type composition. Rocholl et al. (1995) proposed a model of a stratified mantle with the MORB-type above the HIMU-type that is above the EM-type composition. The MORB and EM source

contributions are interpreted to both be components within the subcontinental lithosphere, and the HIMU-type source component is from either a mantle plume head or a fossilized plume head that was emplaced in-between the two chemically heterogeneous layers. The fossilized plume head is the more favorable alternative due to the presence of HIMU beneath several divisions of the past Gondwanaland (East Africa, Antarctica, and the Arabian Plate), indicating that the HIMU is from remnants of a plume/s (or a swarm of plumes) emplaced before the breakup of the supercontinent (Rocholl et al., 1995).

As within the Ross Sea Rift, volcanism along the Red Sea Rift on the Arabian plate also has three mantle source components, EM, depleted MORB-type, and a high radiogenic Pb composition (Bertrand et al., 2003), similar compositions to the Ross Sea Rift, that have erupted over the past 12 million years. The high radiogenic Pb component is similar to a C-component composition; however with the data graphed it is apparent that the data forms a trend line that approaches the HIMU compositional end-member (Bertrand et al., 2003). Therefore the third end member was interpreted to have a HIMU component and not a C-component. The younger samples in the northwest region of the Red Sea form a mixing line in Pb-Pb compositional space between a depleted-MORB end-member and a HIMU end-member, while the older samples in the southeast form a mixing line in Pb-Pb space between an EM end-member and a HIMU end-member. Bertrand et al. (2003) propose a model where HIMU and EM are within the lithospheric mantle and the depleted MORB lies below in the mantle, the depleted MORB-type composition erupts once the



HIMU and EM sources are consumed in a particular location.

A possible source for the magmatism of the Red Sea Rift is the nearby Afar plume, which is inferred to have a HIMU component (Vidal et al., 1991; Schilling et al., 1992; and Deniel et al., 1994). However, helium data ( $R/R_a$ ) from the Red Sea Rift area do not support a plume source (Bertrand et al., 2003). Instead it was proposed that the HIMU signature is widespread in the subcontinental lithosphere below the Arabian Plate, which may either be due to an emplaced fossilized HIMU mantle plume head, or from chromatographic metasomatism of the lithospheric mantle as discussed by Stein et al. (1997). Chromatographic metasomatism would occur where the fluid flow is through porous material, resulting in percolation of the fluid; if the fluid is not in equilibrium with the surrounding material a chromatographic effect would transpire changing the ratios of rare earth and trace elements (Navon et al., 1996). Chromatographic metasomatism could create a HIMU-like isotopic composition by increasing Th/U and Rb/Sr ratios (Bertrand et al., 2003).

The model proposed in this study for the Turkana region of the EARS has strong similarities to both the Ross Sea Rift and the Red Sea Rift. Specifically, the three rift systems all have a HIMU component that is best explained to reside in the subcontinental lithosphere. The idea suggested from Rocholl et al. (1995) that the HIMU component in the lithospheric mantle is widespread and emplaced before the breakup of Gondwanaland seems plausible, though it remains unclear whether the incorporation of HIMU into the lithospheric mantle results from fossilized plume heads or other mechanisms of metasomatic enrichment.

A significant difference between the Turkana area versus the Red Sea and Ross Sea Rifts is the cause of melt generation. The best explanation for magmatism in the Ross Sea Rift and Red Sea Rift is extension of the lithosphere, resulting in decompressional melting of the HIMU component, then the EM component (which also resides in the lithospheric mantle), and then finally when the HIMU and EM compositions have been consumed the underlying MORB mantle decompressionally melts and erupts (Rocholl et al., 1995 and Bertrand et al., 2003). In the Turkana region the extension was not great enough to generate decompressional melting (Ebinger & Ibrahim, 1994; Hendrie et al., 1994; and Furman et al., 2006a). Instead an upwelling of melt (likely a mantle plume), with a C-component composition and an entrained EM composition, beneath the lithospheric mantle in the Turkana region resulted in the magmatism of the Turkana region. This explains the difference in where the EM component is derived from, and also why the final compositions to erupt in the Red Sea Rift and Ross Sea Rift are depleted MORB-type compositions, while the final composition to erupt in the Turkana region is C-component.

## CHAPTER V

### CONCLUSIONS

Quaternary and Tertiary mafic lavas from the Turkana region provide valuable contributions to the understanding of the compositional contributions from melt generation processes occurring in the sublithospheric mantle versus contributions from melt generation processes in the lithosphere in this region. New Pb and Nd isotope ratios of Quaternary and Tertiary Turkana basalts coupled with existing data from Furman et al. (2004, 2006a), show two distinctive trends: the Quaternary samples cluster near the C-component field which is one end-member of a mixing line with two Tertiary samples (the "C Trend"), and the remaining Tertiary samples form a separate mixing line that approaches the HIMU field (the "HIMU Trend") as defined by Stracke et al. (2005). The data then were compared to other regional alkaline data from Napak and Mt. Elgon, which had a similar trend as the HIMU Trend. The comparison revealed a third end-member to the Turkana mafic lavas, an EM1 component. The Sr isotope ratios when looked at with Pb isotope ratios further supported an EM1 end-member for both the C Trend and the HIMU Trend.

Hf isotope ratios of the Quaternary and Tertiary Turkana samples presented a temporal correlation that the other isotopes were unable to demonstrate. In Hf-Pb space the C Trend progresses from an EM1-like component to a C-component over time, while the HIMU Trend progresses from

a HIMU-like component to an EM1 like component throughout time. Based on the chronology, regional data and the spatiotemporal relationships, we interpret HIMU as a lithospheric mantle component, the EM1 end-member as a sublithospheric mantle component that also is an agent of metasomatism in the lithosphere, and the C-component as the second sublithospheric mantle end-member likely present as a result of regional plume activity.

## REFERENCES

- Albarède, F., Télouk, P., Blichert-Toft, J., Boyet, M., Agranier, A., & Nelson, B. (2004). Precise and accurate isotopic measurements using multiple-collector ICPMS. *Geochimica et Cosmochimica Acta* **68**, 2725-2744.
- Allègre, C. J., Moreira, M., & Staudacher, T. (1995)  $^4\text{He}/^3\text{He}$  dispersion and mantle convection. *Geophysical Research Letters* **22**, 2325-2328.
- Ballenine, C. J., Lee, D. C., & Halliday, A. N. (1997). Hafnium isotopic studies of the Cameroon Line and new HIMU paradoxes. Highlights of the Goldschmidt meeting, in honor of A. W. Hofmann. *Chemical Geology* **139**, 111-124.
- Barrat, J. A., Fourcade, S., Jahn, B.-M., Cheminée, J.-L., & Capdevila, R. (1998). Isotope (Sr, Nd, Pb, O) and trace-element geochemistry of volcanics from the Erta Ale Range (Ethiopia). *Journal of Volcanology Geotherm. Res.* **80**, 85-100.
- Bell, K. & Doyle, R. J. (1971). K-Rb relationships in some continental alkalic rocks associated with the East African Rift Valley System. *Geochimica et Cosmochimica Acta* **35**, 903-915.
- Betton, P. J. & Civetta, L. (1984). Strontium and neodymium isotopic evidence for the heterogeneous nature and development of the mantle beneath Afar (Ethiopia). *Earth and Planetary Science Letters* **71**, 59-70.
- Bertrand, H., Chazot, G., Blichert-Toft, J., & Thorvaldson, S. (2003). Implications of widespread high- $\mu$  volcanism on the Arabian Plate for Afar mantle plume and lithosphere composition. *Chemical Geology* **198**, 47-61.
- Bizimis, M., Salters, V. J. M., & Dawson, J. B. (2003). The brevity of carbonatite sources in the mantle: Evidence from Hf isotopes. *Contributions to Mineralogy and Petrology* **145**, 281-300.
- Blichert-Toft, J. & White, W. M. (2001). Hf isotope geochemistry of the Galapagos Islands. *Geochemistry Geophysics Geosystems* **2**, 2000GC000138.
- Chauvel, C. & Blichert-Toft, J. (2001). A hafnium isotope and trace element perspective on melting of the depleted mantle. *Earth and Planetary Science Letters* **190**, 137-151.
- Chauvel, C., Hofmann, A. W., & Vidal, P. (1992). HIMU-EM: the French Polynesia connection. *Earth and Planetary Science Letters* **110**, 99-119.

Chauvel, C., McDonough, W., Guille, W., Maury, R., & Duncan, R. (1997). Contrasting old and young volcanism in Rurutu Island, Austral chain. *Chemical Geology* **139**, 125-143.

Class, C., Altherr, R., Eberz, G., & McCulloch, M. T. (1994). Geochemistry of Pliocene to Quaternary alkali basalts from the Huri Hills, Northern Kenya. *Chemical Geology* **113**, 1-22.

Class, C., Goldstien, S. L., Stute, M., Kurz, M. D., & Schlosser, P. (2005). Grand Comore Island: A well-constrained "low  $^3\text{He}/^4\text{He}$ " mantle plume. *Earth and Planetary Science Letters* **233**, 391-409.

Clément, J.-P., Caroff, M., Hémond, C., Tiercelin, J. J., Bollinger, C., Guillou, H., & Cotton, J. (2003). Pleistocene magmatism in a lithospheric transition area: Petrogenesis of alkaline and peralkaline lavas from the Baringo-Bogoria Basin, Central Kenya Rift. *Can. Journal of Earth Sciences* **40**, 1239-1257.

Curtis, P. C. (1991). Competing magmatic processes at a continental rift: petrology and geochemistry of Quaternary volcanoes in the Turkana Rift Zone, East Africa. Ph.D. thesis, University of North Carolina at Chapel Hill.

Davidson, A. & Rex, D. C. (1980). Age of volcanism and rifting in southern Ethiopia. *Nature* **283**, 657-658.

Davidson, J. P. & Tepley, F. J. (1997). Recharge in volcanic systems: Evidence from isotope profiles of phenocrysts. *Science* **275**, 826-829.

Davidson, J. P., Tepley, F. J., Palacz, Z., & Meffan-Main, S. (2001) Magma recharge, contamination, and residence times revealed by in-situ laser ablation isotopic analysis of feldspar in volcanic rocks. *Earth and Planetary Science Letters* **184**, 427-442.

Davidson, J. P. & Wilson, I. R. (1989). Evolution of an alkali basalt-trachyte suite from Jebel Marra volcano, Sudan, through assimilation and fractional crystallization. *Earth and Planetary Science Letters* **95**, 141-160.

Davies, G. R. & MacDondald, R. (1987). Crustal influences in the petrogenesis of the Naivasha basalt-comendite complex: Combined trace element and Sr-Nd-Pb isotope constraints. *Journal of Petrology* **28**, 1009-1031.

Debayle, E., Leveque, J. -J., & Cara, M. (2001). Seismic evidence for a deeply rooted low-velocity anomaly in the upper mantle beneath the northeastern Afro/Arabian continent. *Earth and Planetary Science Letters* **193**, 423-436.

- De Mulder, M., Hertogen, J., Deutsch, S., & André, L. (1986). The role of crustal contamination in the potassic suite of the Karisimbi Volcano (Virungu, African Rift Valley). *Chemical Geology* **57**, 117-136.
- Deniel, C., Vidal, P., Coulon, C., Vellutini, P. J. & Piguet, P. (1994). Temporal evolution of mantle sources through continental rifting: The volcanism of Djibouti (Afar). *Journal of Geophysical Research* **B99**, 2853-2869.
- Dunkleman, T. J., Karson, J. A., & Rosendahl, B. R. (1988). Structural style of the Turkana Rift. *Geology* **16**, 258-261.
- Ebinger, C. J. & Ibrahim, N. H. (1994). Multiple episodes of rifting in Central and East Africa. *Geology* **16**, 258-261.
- Ebinger, C. J., Yemane, T., Harding, D. J., Tesfaye, S., Kelley, S., & Rex, D. C. (2000). Rift deflection, migration, and propagation: linkage of the Ethiopian and Eastern rifts, Africa. *Geological Society of America Bulletin* **112**, 163-176.
- Forsyth, D. W. & Detrick, R. S. (2003). Probing geodynamic processes beneath the sea floor. *Eos Transactions, American Geophysical Union* **84**, 517, 523.
- Forsyth, D. W., Scheirer, D. S., Webb, S. C., Dorman, L. M., Orcutt, J. A., Harding, A. J., Blackman, D. K., Phipps, M. J., Detrick, R. S., Yang, S., Wolfe, C. J., Canales, J. P., Toomey, D. R., Sheehan, A. F., Solomon, S. C., & Wilcock, W. S. D. (1998). Imaging the deep seismic structure beneath a mid-ocean ridge; the MELT experiment. *Science* **280**, 1215 – 1218.
- Furman, T., Bryce, J. G., Karson, J., & Iotti, A. (2004). East African Rift System (EARS) plume structure: insights from Quaternary mafic lavas of Turkana, Kenya. *Journal of Petrology* **45**, 1069–1088.
- Furman, T., Bryce, J., Rooney, T., Hanan, B., Yirgu, G., & Ayalew, D. (2006b). Heads and tails: 30 million years of the Afar Plume. *Geological Society, London* **259**, 95-119.
- Furman T. & Graham D. (1999). Erosion of lithospheric mantle beneath the East African Rift system: evidence from the Kivu volcanic province. *Lithos* **48**, 237-262.
- Furman, T., Kaleta, K. M., & Bryce, J. G. (2006a). Tertiary mafic lavas of Turkana, Kenya: Constraints on East African plume structure and the occurrence of high- $\mu$  volcanism in Africa. *Journal of Petrology* **47**, 1221-1244.
- Gautheron, C. & Moreira, M. (2002). Helium signature of the subcontinental lithospheric mantle. *Earth and Planetary Science Letters* **199**, 39-47.

George, R. M. M. & Rogers, N. W. (1999). The petrogenesis of Plio-Pliocene alkaline volcanic rocks from the Tosa Sucha region, Arab Minch, Southern Main Ethiopian Rift. *Acta Vulcanol.* **11**, 121-130.

George, R., Rogers, N., & Kelley, S. (1998). Earliest magmatism in Ethiopia: evidence for two mantle plumes in one flood basalt province. *Geology* **26**, 923-926.

Graham, D. (2002). Noble gas isotope geochemistry of mid-ocean ridge and ocean island basalts; characterization of mantle reservoirs. *Reviews in Mineralogy and Geochemistry* **47**, 247-317.

Graham, D. W., Reid, M. R., Jordan, B. T., Grunder, A. L., Leeman, W. P., & Lupton, J. E. (2007). Mantle source provinces beneath the Pacific Northwest revealed by helium isotope variations in basaltic lavas. *Geological Survey of America - Abstracts with Programs* **39**, pp 455.

Halliday, A. N., Lee, D. -C., Tommasini, S., Davies, G. R., Paslikc, C. R., Fitton, J. G., & James, D. E. (1995). Incompatible trace elements in OIB and MORB and source enrichment in the sub-oceanic mantle. *Earth and Planetary Science Letters* **133**, 379-395.

Hamelin, B., Dupre, B., & Allegre, C. J. (1984). The lead isotope systematics of ophiolite complexes. *Earth and Planetary Science Letters* **67**, 351-366.

Hanan, B. B. & Graham, D. W. (1996). Lead and helium isotope evidence from oceanic basalts for a common deep source of mantle plumes. *Science* **272**, 991-995.

Hanyu, T. & Kaneoka, I. (1997). The uniform and low  $^3\text{He}/^4\text{He}$  ratios of HIMU basalts as evidence for recycled materials. *Nature* **390**, 273-276.

Hart, W. K., Woldegabriel, G., Walter, R. C., & Mertzman, S. A. Jr. (1989). Basaltic Volcanism in Ethiopia: Constraints on continental rifting and mantle interactions. *Journal of Geophysical Research* **B94**, 7731-7748.

Hauri, E. H. & Hart, S. R. (1993). Re-Os isotope systematics of HIMU and EMII oceanic island basalts from the South Pacific Ocean. *Earth and Planetary Science Letters* **114**, 353-371.

Hemond, C., Devey, C. W., & Chauvel, C. (1994). Source compositions and melting processes in the Society and Austral plumes (South Pacific Ocean); element and isotope (Sr, Nd, Pb, Th) geochemistry. *Chemical Geology* **115**, 7-45.



Hendrie, D. B., Kuszniir, N. J., Morley, C. K., & Ebinger, C. J. (1994). Cenozoic extension in northern Kenya: a quantitative model of rift basin development in the Turkana region. *Tectonophysics* **236**, 409-438.

Hilton, D. R., Gronvold, K., Sveinbjornsdottir, A. E., & Hammerschmidt, K. (1998). Helium isotope evidence for off-axis degassing of the Iceland hotspot. *Chemical Geology* **149**, 173-187.

Kelemen P. B., Hirth G., Shimizu N., Spiegelman M., & Dick H. J. B. (1997). A review of melt migration processes in the adiabatically upwelling mantle beneath oceanic spreading ridges. *Philos. Trans. Royal Society of London* **355**, 283-318.

KRISP Working Group (1995). Group takes a fresh look at the lithosphere underneath southern Kenya. *Eos Transactions, American Geophysical Union* **76**, 81-82.

Kurz, M. D., Jenkins, W. J., & Hart, S. R. (1982a). Helium isotopic systematic of oceanic islands and mantle heterogeneity. *Nature* **297**, 43-47.

Kurz, M. D., Jenkins, W. J., Schilling, J. -G., & Hart, S. R. (1982b). Helium isotopic variation in the mantle beneath the central North Atlantic Ocean. *Earth and Planetary Science Letters* **58**, 1-14.

Li, Y., Thurber, C., Prothero, W. A., Munson, C., Shengold, L., Deems, L., & Short, M. (1990). Project ALOHA; PASSCAL experiment on Hawaii. *Eos Transactions, American Geophysical Union- Programs with Abstracts* **71**, 1615.

Lin, S., van Keken, P. E., Brandenburg, J. P., Furman, T., & Bryce, J. (2007). Mantle support of the East African Rift System. *Eos Transactions, American Geophysical Union- Programs with Abstracts* **88**, Abstract V33B-1387.

MacDonald, R., Davies, G. R., Upton, B. G. J., Dunkley, P. N., Smith, M., & Leat, P. T. (1995). Petrogenesis of Silali Volcano, Gregory Rift, Kenya. *Special Publication Geological Society, London* **152**, 703-720.

Marty, B., Pik, R., & Gezahegn, Y. (1996). Helium isotopic variations in Ethiopian plume lavas: Nature of magmatic sources and limit on lower mantle contribution. *Earth and Planetary Science Letters* **144**, 223-237.

Mattielli, N., Weis, D., Blichert-Toft, J., & Albarede, F. (2002). Hf isotope evidence for a Miocene change in the Kerguelen mantle plume composition. *Journal of Petrology* **43**, 1327-1339.

Montelli, R., Nolet, G., Dahlen, F. A., Masters, G., Engdahl, E. R., & Hung, S. -H. (2004). Finite-frequency tomography reveals a variety of plumes in the mantle. *Science* **303**, 338-343.

Moreira, M. & Kurz, M. D. (2001). Subducted oceanic lithosphere and the origin of the 'high  $\mu$ ' basalt helium isotopic signature. *Earth and Planetary Science Letters* **189**, 49-57.

Morgan, J. P. & Morgan, W. J. (1999). Two-stage melting and the geochemical evolution of the mantle: A recipe for mantle plum-pudding. *Earth and Planetary Science Letters* **170**, 215-239.

Morimoto, N. (1988). Nomenclature of pyroxenes. *Fortschritte der Mineralogie* **66**, 237-252

Morley, C. K. (1994). Interaction of deep and shallow processes in the evolution of the Kenya rift. *Tectonophysics* **236**, 81-91.

Morley, C. K., Wescott, W. A., Stone, D. M., Harper, R. M., Wigger, S. T., & Karanja, F. M. (1992). Tectonic evolution of the northern Kenya Rift. *Journal of the Geological Society, London* **149**, 333-348.

Nakamura, Y. & Tatsumoto, M. (1988). Pb, Nd, and Sr isotopic evidence for a multicomponent source for rocks of Cook-Austral Islands and heterogeneities of mantle plumes. *Geochimica et Cosmochimica Acta* **52**, 2909-2924.

Navon, O., Frey, F. A., & Takazawa E. (1996). Magma transport and metasomatism in the mantle: A critical review of current geochemical models – Discussion. *American Mineralogist* **81**, 754-759.

Norry, M. J., Truckle, P. H., Lippard, S. J., Hawkesworth, C. J., Weavers, S. D., Marriner, G. F., & Bailey, D. K. (1980). Isotopic and trace element evidence from lavas bearing on mantle heterogeneity beneath Kenya (and discussion). *Philos. Trans. Royal Society of London* **A297**, 259-271.

Nyblade, A. A. (2003). The origin of the African Superswell. *Eos Transactions, American Geophysical Union- Programs with Abstracts* **84(46)**, Abstract S51F-01 Invited.

Nyblade, A. A., Owens, T. J., Gurrola, H., Ritsema, J., & Langston, C. A. (2000). Seismic evidence for a deep upper mantle thermal anomaly beneath east Africa. *Geology* **28**, 599-602.

Nyblade, A. A. & Robinson, S. W. (1994). The African Superswell. *Geophysical Research Letters* **21(9)**, 765-768.

Ochieng', J. O., Wilkinson, A. F., Kagasi, J., & Kimomo, S. (1988). Geology of the Loiyangalani area. Report 107 (Reconnaissance). *Republic of Kenya Ministry of Environment and Natural Resources, Mines and Geology Department*, pp 53.

Osada, Y., Fujimoto, H., Miura, S., Sweeney, A., Kanazawa, T., Nakao, S., Sakai, S., Hildebrand, J. A., & Chadwell, C. D. (2003). Estimation and correction for the effect of sound velocity variation on GPS/acoustic seafloor positioning; an experiment off Hawaii Island. *Earth, Planets and Space* **55**, pp 4.

Palacz, Z. A. & Saunders, A. D. (1986). Coupled trace element and isotope enrichment in the Cook-Austral-Samoa islands, southwest Pacific. *Earth and Planetary Science Letters* **79**, 270-280.

Paslick, C. R., Halliday, A. N., Lange, R. A., James, D. E., & Dawson, J. B. (1996). Indirect crustal contamination: Evidence from isotopic and chemical disequilibria in minerals from alkali basalts and nephelinites from Northern Tanzania. *Contributions to Mineralogy and Petrology* **125**, 277-292.

Peccerillo, A., Barberio, M. R., Yirgu, G., Ayalew D., Barbieri, M., & Wu, T. -W. (2003). Relationships between mafic and peralkaline silicic magmatism in continental rift settings: A petrological, geochemical and isotopic study of the Gedemsa Volcano, Central Ethiopian Rift. *Journal of Petrology* **44**, 2003-2032.

Pik, R., Deniel, C., Coulon, C., Yirgu, G., & Marty, B. (1999). Isotopic and trace element signatures of Ethiopian flood basalts; evidence for plume-lithosphere interactions. *Geochimica et Cosmochimica Acta* **63**, 2263-2279.

Pik, R., Marty, B., & Hilton, D. R. (2006). How many mantle plumes in Africa? The geochemical point of view. *Chemical Geology* **226**, 100-114.

Prinzhofer, A., Lewin, E., & Allègre, C. J. (1989). Stochastic melting of the marble cake mantle: evidence from local study of the East Pacific Rise at 12°50'N. *Earth and Planetary Science Letters* **92**, 189-206.

Putirka, K. D. (2005). Mantle potential temperatures at Hawaii, Iceland, and the mid-ocean ridge system, as inferred from olivine phenocrysts: Evidence for thermally driven mantle plumes. *Geochemistry Geophysics Geosystems* **6**, 2005GC000915.

Ramos, F. C., Wolff, J. A., & Tollstrup, D. L. (2005). Sr isotope disequilibrium in Columbia River flood basalts: Evidence for rapid shallow-level open-system processes. *Geology* **33**, 457-460.

Ribe, N. M. (1987). Theory of Melt Segregation – A review. *Journal of Volcanology and Geothermal Research* **33**, 241-253.

Richter, F. M. & Daly S. F. (1989). Dynamical and chemical effects of melting a heterogeneous source. *Journal of Geophysical Research* **94**, 12499-12510.

- Rocholl, A., Stein, M., Molzahn, M., Hart, S. R., & Wörner, G. (1995). Geochemical evolution of rift magmas by progressive tapping of a stratified mantle source beneath the Ross Sea Rift, Northern Victoria Land, Antarctica. *Earth and Planetary Science Letters* **131**, 207-224.
- Rogers, N. W., MacDonald, R., Fitton, J. G., George, R. M. M., Smith, M., & Barreiro, B. (2000). Two mantle plumes beneath the East African Rift System: Sr, Nd, and Pb isotopic evidence from Kenya Rift basalts. *Earth and Planetary Science Letters* **176**, 387-400.
- Rogers, N. W., Thomas, L. E., MacDonald, R., Hawkesworth, C. J., & Mokadem, F. (2006).  $^{238}\text{U}$ - $^{230}\text{Th}$  disequilibrium in recent basalts and dynamic melting beneath the Kenya Rift. *Chemical Geology* **234**, 148-168.
- Salters, V. J. M. & White, W. M. (1998). Hf isotope constraints on mantle evolution. *Chemical Geology* **145**, 447-460.
- Schilling, J. -G., Kingsley, R. H., Hanan, B. B., & McCully, B. L. (1992). Nd-Sr-Pb isotopic variations along the Gulf of Aden: evidence for Afar mantle plume-continent lithosphere interaction. *Journal of Geophysical Research* **97**, 10927-10966.
- Simonetti, A. & Bell, K. (1994). Nd, Pb, and Sr isotopic data from the Napak carbonatite-nephelinite center, Eastern Uganda: An example of open-system crystal fractionation. *Contributions to Mineralogy and Petrology* **115**, 356-366.
- Simonetti, A. & Bell, K. (1995). Nd, Pb, and Sr isotopic data from the Mount Elgon volcano, eastern Uganda – western Kenya: Implications for the origin and evolution of nephelinite lavas. *Lithos* **36**, 141-153.
- Sims, K. W. W. & DePaolo, D. J. (1997). Inferences about mantle magma sources from incompatible element concentration ratios in oceanic basalts, *Geochimica et Cosmochimica Acta* **61**, 765-784.
- Sobolev, A. V., Hofmann, A. W., Sovolev, S. V., & Nikogosian, I. K. (2005). An olivine free mantle source of Hawaiian shield basalts. *Nature* **434**, 590-597.
- Sours-Page, R., Johnson, K. T. M., Nielsen, R. L., & Karsten, J. L. (1999). Local and regional variation of MORB parent magmas: evidence from inclusions from the Endeavor Segment of the Juan de Fuca Ridge. *Contributions to Mineralogy and Petrology* **134**, 342-363.
- Sours-Page R., Nielsen R. L., & Batiza R. (2002). Melt inclusions as indicators of parental magma diversity on the northern East Pacific Rise. *Chemical Geology* **183**, 237-261.

Späth, A., le Roex, A. P., & Opiyo-Akech, N. (2001). Plume-lithosphere interaction and the origin of continental rift-related alkaline volcanism – the Chyulu Hills volcanic province, Southern Kenya. *Journal of Petrology* **42**, 765-787.

Spera, F. J. & Bohron, W. A. (2004). Open-system magma chamber evolution: an energy-constrained geochemical model incorporating the effects of concurrent eruption, recharge, variable assimilation and fractional crystallization (E'RA<sup>c</sup>FC). *Journal of Petrology* **45**, 2459-2480.

Stein, M., Navon, O., & Kessel, R. (1997). Chromatographic metasomatism of the Arabian-Nubian lithosphere. *Earth and Planetary Science Letters* **152**, 75-91.

Stewart, K. & Rogers, N. W. (1996). Mantle plume and lithosphere contribution to basalts from Southern Ethiopia. *Earth and Planetary Science Letters* **139**, 195-211.

Stracke, A., Bizimis, M., & Salters, V. J. M. (2003). Recycling oceanic crust: Quantitative constraints. *Geochemistry, Geophysics, Geosystems* **4**, 2001GC000223.

Stracke, A., Hofmann, A. W., & Hart, S. R. (2005). FOZO, HIMU, and the rest of the mantle zoo. *Geochemistry Geophysics Geosystems* **6**, 2004GC000824.

Sun, S- S. & McDonough, W. F. (1989). Chemical and isotopic systematics of oceanic basalts: implications for mantle composition and processes. In: A.D. Saunders and M. J. Norry (eds) *Magmatism in the Ocean Basins. Geological Society of London*, 313-315.

Thirlwall, M. F. (2002). Multicollector ICP-MS analysis of Pb isotopes using a <sup>207</sup>Pb-<sup>204</sup>Pb double spike demonstrates up to 4000ppm/amu systematic errors in TI-normalization. *Chemical Geology* **184**, 255-279.

Todt, W., Cliff, R. A., Hanser, A., & Hofmann, A. W. (1996). Evaluation of a <sup>202</sup>Pb-<sup>205</sup>Pb double spike for high precision lead isotope analysis. In: Basu, A. & Hart, S. (eds) *Earth Processes: Reading the Isotopic Code. Geophysical Monograph, American Geophysical Union* **95**, 429-437.

Trua, T., Deniel, C., & Massuoli, R. (1999). Crustal control in the genesis of Plio-Quaternary bimodal magmatism o the Main Ethiopian Rift (MER): Geochemical and isotopic (Sr, Nd, Pb) evidence. *Chemical Geology* **155**, 201-231.

Vidal, P., Chauvel, C., & Brousse, R. (1984). Large mantle heterogeneity beneath French Polynesia. *Nature* **307**, 536-538.

Vidal, P., Deniel, C., Vellutini, P. J., Piguët, P., Coulon, C., Vincent, J., & Audin, J. (1991). Changes of mantle sources in the course of a rift evolution: The Afar case. *Geophysical Research Letters* **18**, 1913-1916.

Vollmer, R. & Norry, M. J. (1983). Possible origin of K-rich volcanic rocks from Virunga, East Africa, by metasomatism of continental crust material: Pb, Nd and Sr isotopic evidence. *Earth and Planetary Science Letters* **64**, 374-386.

White, W. M., Albarède, F., & Télouk, P. (2000). High-precision analysis of Pb isotopic ratios using multi-collector ICP-MS. *Chemical Geology* **167**, 257-270.

Workman, R. K., Hart, S. R., Jackson, M., Regelous, M., Farley, K. A., Blusztajn, J., Kurz, M., & Staudigel, H. (2004). Recycled metasomatized lithosphere as the origin of the Enriched Mantle II (EM2) end-member: Evidence from the Samoan Volcanic Chain. *Geochemistry Geophysics Geosystems* **5**, 2003GC000623.

Yingjie, Y. & Forsyth, D. W. (2005). Seismic velocity and attenuation constraints on the formation of oceanic plate and the origin of the low-velocity zone. *Geological Society of America- Abstracts with Programs* **37**, pp 521.

## **APPENDICES**

## APPENDIX A

### SAMPLE PETROGRAPHY

#### Quaternary Basalt Petrography

The Quaternary basalt samples are massive to vesicular microcrystalline basalts, most are fresh samples from within a lava flow with little alterations. The samples have olivine, pyroxene, and/or plagioclase phenocrysts with a groundmass of the same minerals plus trace amounts of oxides. The Barrier samples (BR-05 and BR-33) are composed of 15 to 25% pyroxene, about 5% olivine, and 10% plagioclase phenocrysts. Most phenocrysts are subhedral with a few euhedral; pyroxenes are 0.5 to 2 mm, olivines are 0.5 to 2 mm, and the plagioclase phenocrysts are around 1 mm. BR-05 is very vesicular with vesicles up to 2 mm, while BR-33 is massive.

There are a variety of samples from South Island (KCH-16, KCH-19, SI-15, SI-20B, and SI-24) with different modes. KCH-16 has 10% plagioclase phenocrysts that are around 1 mm, and trace amounts of olivine phenocrysts up to 1 mm. The sample has vesicles up to 2 mm. KCH-19 is massive with 10% pyroxene phenocrysts that average about 1 mm across, and trace amounts of plagioclase and olivine phenocrysts that are also about 1 mm. SI-15 is massive with euhedral pyroxene and plagioclase phenocrysts. The pyroxene phenocrysts compose less than 5 % of the whole rock with crystals around 1 mm. The plagioclase phenocrysts compose 15% of the whole rock with crystals up to 2



mm. SI-20B is very vesicular, with numerous 1 mm vesicles. The sample is composed of 25 % pyroxene, 15 % olivine, and 10% plagioclase phenocrysts. All phenocrysts are subhedral to euhedral and 1 to 3 mm in size. SI-24 is massive with few 0.5 mm vesicles. The sample contains 15 % olivine, 15 % pyroxene, and 5 % plagioclase phenocrysts. The olivine crystals are slightly oxidized and are up to 5 mm in size. The pyroxene and plagioclase crystals are both 1 to 2 mm.

The Central Island samples (CI-08, CI-09, CI-10, CI-31, and CI-32) are also diverse in composition. CI-08 is very vesicular with many vesicles less than 0.5 mm. The only phenocryst present in CI-08 is plagioclase, which makes up about 5 % of the whole rock and are around 1 mm. The phenocrysts are anhedral. CI-09 and CI-10 are both massive with around 30 % plagioclase phenocrysts. The plagioclase crystals are anhedral and 2 to 4 mm. The samples also have trace pyroxenes up to 1 mm. CI-31 and CI-32 are both vesicular with vesicles between 1 and 3 mm in diameter. They both have 10 to 20 % plagioclase phenocrysts that are 1 to 3 mm anhedral crystals. They also have small amounts (around 5 %) of subhedral pyroxenes, making up less than 10 % of the samples. The pyroxene crystals are around 1 mm. CI-31 also has trace amounts of olivine phenocrysts around that are about 3 mm.

Longipi samples (LGP 92-11, LGP-607, LGP-36, and LGP-39) are much sparser in phenocrysts than the other Quaternary samples. LGP 92-11 and LGP-607 are massive with few small (less than 0.5 mm) vesicles. The samples are composed of 5 to 10 % subhedral to euhedral olivine phenocrysts that are 1

to 2 mm, 5 % pyroxene phenocrysts that are 1 mm, and trace plagioclase phenocrysts that are also 1 mm. LGP-36 is very vesicular with many vesicles less than 0.5 mm. The sample contains trace amounts of plagioclase and olivine phenocrysts that are about 1 mm. LGP-39 is very massive with only trace amounts of olivine phenocrysts that are 1 to 2 mm.

### **Tertiary Basalt Petrology**

The Tertiary basalt samples used in this study are massive microcrystalline basalts, most being very fresh samples from within a lava flow with little alterations. The majority of the basalts have olivine, pyroxene, and plagioclase phenocrysts with a groundmass of the same minerals, plus trace amounts of oxides. Olivines are the most abundant phenocryst in the Jarigole samples (JRG-03, JRG-07, JRG-10, and JRG-12) accounting for 5 to 20% of the whole rock; the crystals vary between 0.5 to 4 mm in size. Plagioclase and pyroxene phenocrysts each comprise 2 to 10% of the whole rock and have crystal sizes between 0.5 to 5 mm.

The Kulal sample (KL-18) has about 5% olivine phenocrysts and less than 5% plagioclase phenocrysts, and no pyroxenes. The phenocrysts range in size from 1 to 3 mm. The Porr samples (PORR 404, PORR 602, and PORR 606) have fewer phenocrysts with only trace amounts of olivine, around 1 mm in size, and a few small feldspar cumulates between 1 and 3 mm in size.

The two Kajole samples are very different from each other. One sample (KJ-1) has some olivine phenocrysts, comprising 2 to 3% of the whole rock, with

crystals between 1 and 3 mm. KJ-1 has about 5% pyroxene phenocrysts that are up to 3 mm in size, and trace amounts of feldspars that are within the matrix. The other sample (KJ-16) has an oxidized matrix (grey to reddish brown in color) with olivine crystals in the matrix and a few large enough to be phenocrysts. Some of the olivine crystals are fresh while a few are weathered to a brownish shade. No other phenocrysts are observed in KJ-16.

The last of the Tertiary samples is from Loryu (LOR86-23B). This sample is unlike the other Tertiary samples and has an unknown age. The basalt is vesicular and has an oxidized matrix. The vesicles of LOR86-23B are filled in with secondary minerals (note: for geochemical analyses the secondary minerals were not included). The basalt contains some plagioclase phenocrysts that compose about 3% of the whole rock, and trace amounts of olivine and pyroxene phenocrysts. Most phenocrysts are oxidized as well.

## APPENDIX B

### MICROPROBE DATA OF TURKANA OLIVINE

Olivine phenocrysts of five Quaternary and Tertiary Turkana lavas were analyzed for major element compositions on a JEOL JXA-733 Superprobe at MIT. Transects of the phenocrysts were measured for SiO<sub>2</sub>, TiO<sub>2</sub>, Al<sub>2</sub>O<sub>3</sub>, Cr<sub>2</sub>O<sub>3</sub>, FeO, MnO, MgO, CaO, and NiO weight percent. The major element standards used were Marjalotti Olivine (MARJ) with 40.24 wt. % SiO<sub>2</sub>, 11.53 wt. % FeO, and 48.08 wt. % MgO, and synthetic Fayalite (SYNFA) with 29.49 wt. % SiO<sub>2</sub> and 70.52 wt. % FeO. The standards used for minor elements were Rutile (TiO<sub>2</sub>) for Ti, Uvaorite (Ca<sub>3</sub>Cr<sub>2</sub>Si<sub>3</sub>O<sub>12</sub>) for Cr, and Rhodonite (MnSiO<sub>3</sub>) for Mn. For most elemental analyses the count times ranged from 10 – 50 s. However, due to the small amount of Ni in general in olivine, the Ni analyses had a count time of 300 s. The forsterite composition was calculated by  $Mg / (Fe + Mg + Mn)$  mol. %. The nickel and forsterite compositional differences between the olivine cores and rims (Tables 6, 7, 8, and 9) are of particular interest to reveal magma mixing and possible source lithologies (see "Results and Discussion" for further discussion of the data). The microphotographs of the minerals with the points analyzed are in Figures 22 – 30.

**Table 6:**  
Turkana Quaternary olivine core compositions.

OLIVINE CORES								
Quaternary:		Fo %			NiO wt. %			Totals %
Sample	Mineral #	Measured	Average	Std. Dev.	Measured	Average	Std. Dev.	
BR-05	1	85.7			0.19			98.8
BR-05	1	85.7			0.21			99.3
BR-05	1	85.8	85.8	0.1	0.19	0.21	0.02	99.9
BR-05	1	85.7			0.19			99.3
BR-05	1	85.8			0.24			99.6
BR-05	1	85.9			0.21			99.0
BR-05	2	86.7			0.19			98.8
BR-05	2	86.7			0.29			98.6
BR-05	2	86.5			0.29			99.1
BR-05	2	86.6			0.24			99.6
BR-05	2	86.7	86.7	0.3	0.25	0.24	0.04	99.6
BR-05	2	87.0			0.20			98.6
BR-05	2	87.4			0.25			98.8
BR-05	2	86.2			0.23			100.1
BR-05	2	86.3			0.19			99.7
CI-31	1	84.7			0.19			99.2
CI-31	1	84.8			0.18			99.5
CI-31	1	84.6			0.21			99.4
CI-31	1	84.8	84.9	0.2	0.16	0.19	0.02	99.2
CI-31	1	84.9			0.19			99.3
CI-31	1	85.1			0.23			98.8
CI-31	1	85.1			0.19			99.3
CI-31	2	84.5			0.16			99.6
CI-31	2	84.4			0.15			99.8
CI-31	2	84.2	84.5	0.3	0.18	0.16	0.01	99.9
CI-31	2	84.8			0.16			99.3
CI-31	2	84.9			0.16			99.1
CI-31	2	84.2			0.16			99.8
CI-31	2	84.0			0.19			99.6
CI-31	2	84.1			0.16			99.5
CI-31	2	84.2	84.1	0.1	0.19	0.18	0.01	98.9
CI-31	2	84.1			0.19			99.3
CI-31	2	84.2			0.16			99.3
CI-31	2	84.2			0.20			99.8

Table 6 - Continued

OLIVINE CORES

Quaternary:		Fo %			NiO wt. %			Totals %
Sample	Mineral #	Measured	Average	Std. Dev.	Measured	Average	Std. Dev.	
SI-24	1	87.9			0.38			99.4
SI-24	1	87.4			0.35			98.7
SI-24	1	87.5	87.5	0.2	0.31	0.33	0.03	98.8
SI-24	1	87.3			0.33			99.6
SI-24	1	87.3			0.31			99.4
SI-24	1	87.4			0.31			99.8
SI-24	1	87.7			0.29			99.0
SI-24	1	87.5			0.31			99.5
SI-24	1	87.7	87.6	0.1	0.28	0.30	0.02	99.4
SI-24	1	87.6			0.33			99.7
SI-24	1	87.7			0.31			99.4
SI-24	1	87.5			0.29			99.5
SI-24	2	87.6			0.30			99.7
SI-24	2	88.1			0.32			98.9
SI-24	2	87.5	87.7	0.2	0.29	0.30	0.01	99.2
SI-24	2	87.6			0.29			99.7
SI-24	2	87.5			0.30			99.6
SI-24	2	87.6			0.31			98.7
SI-24	2	87.8			0.37			98.8
SI-24	2	88.3	88.0	0.3	0.28	0.33	0.05	100.8
SI-24	2	87.9			0.35			100.5
SI-24	5	86.5			0.28			99.2
SI-24	5	86.3			0.28			99.4
SI-24	5	86.3	86.4	0.1	0.27	0.28	0.01	99.3
SI-24	5	86.5			0.29			98.8
SI-24	5	86.2			0.30			99.5

**Table 7:**  
Turkana Tertiary olivine core compositions.

**OLIVINE CORES**

Tertiary:		Fo %			NiO wt. %			Totals %
Sample	Mineral #	Measured	Average	Std. Dev.	Measured	Average	Std. Dev.	
JRG 07	1	87.3			0.31			99.4
JRG 07	1	86.9			0.30			99.5
JRG 07	1	86.7	86.9	0.3	0.29	0.30	0.01	99.6
JRG 07	1	87.2			0.29			99.4
JRG 07	1	86.9			0.31			99.9
JRG 07	1	86.5			0.30			99.8
JRG 07	1	86.6			0.26			100.3
JRG 07	1	86.8			0.37			99.9
JRG 07	1	86.9	86.7	0.2	0.28	0.32	0.04	100.2
JRG 07	1	86.6			0.32			99.7
JRG 07	1	86.6			0.36			100.4
JRG 07	1	86.9			0.31			100.4
JRG 07	2	87.8			0.40			99.1
JRG 07	2	87.6			0.31			99.1
JRG 07	2	87.2	87.6	0.3	0.35	0.36	0.04	99.9
JRG 07	2	87.9			0.36			98.8
JRG 07	2	87.5			0.39			99.4
JRG 07	2	87.7			0.32			99.0
JRG 07	2	87.5			0.29			99.5
JRG 07	2	87.3	87.5	0.2	0.31	0.31	0.01	100.0
JRG 07	2	87.7			0.32			99.5
JRG 07	2	87.6			0.32			99.1
JRG 07	4	86.1			0.26			99.5
JRG 07	4	85.8			0.26			99.3
JRG 07	4	85.9	86.0	0.2	0.27	0.27	0.01	99.1
JRG 07	4	86.2			0.28			99.1
JRG 07	4	85.9			0.29			99.3
JRG 10	1	84.9			0.20			99.3
JRG 10	1	84.8			0.21			99.1
JRG 10	1	84.6	84.7	0.1	0.22	0.21	0.01	99.7
JRG 10	1	84.7			0.22			99.3
JRG 10	1	84.6			0.21			99.1
JRG 10	1	84.7			0.21			99.5

**Table 7 - Continued**

Tertiary:		Fo %			NiO wt. %			Totals %
Sample	Mineral #	Measured	Average	Std. Dev.	Measured	Average	Std. Dev.	
JRG 10	1	84.5			0.26			98.7
JRG 10	1	84.4			0.23			98.9
JRG 10	1	84.6	84.5	0.1	0.29	0.26	0.02	98.8
JRG 10	1	84.4			0.25			98.9
JRG 10	1	84.6			0.27			99.2
JRG 10	2	85.9			0.24			99.9
JRG 10	2	86.1			0.24			99.6
JRG 10	2	86.5	86.1	0.3	0.26	0.24	0.01	98.5
JRG 10	2	85.8			0.23			99.4
JRG 10	2	86.1			0.23			99.7
JRG 10	2	85.8			0.28			98.7
JRG 10	2	85.7	85.8	0.3	0.28	0.29	0.02	98.6
JRG 10	2	85.5			0.31			99.8
JRG 10	2	86.3			0.28			98.6

**Table 8:**  
Turkana Quaternary olivine rim compositions.

Quaternary:				
Sample	Mineral #	Fo %	NiO	Totals %
BR-05	1	86.03	0.17	99.3
BR-05	2	85.76	0.26	98.8
BR-05	2	86.24	0.26	98.9
CI-31	2	70.57	0.12	99.4
SI-24	1	68.59	0.19	98.8
SI-24	1	70.34	0.21	99.0
SI-24	1	61.27	0.18	99.1
SI-24	1	84.60	0.39	99.1
SI-24	1	72.29	0.27	99.7
SI-24	1	70.46	0.24	99.5
SI-24	1	68.31	0.27	99.0
SI-24	2	69.33	0.18	99.6
SI-24	2	70.61	0.22	99.5
SI-24	2	79.01	0.28	99.9
SI-24	2	81.29	0.29	99.3
SI-24	5	63.37	0.17	98.9



**Table 9:**  
Turkana Tertiary olivine rim compositions.

**OLIVINE RIMS**

Tertiary:				
Sample	Mineral #	Fo %	NiO	Totals %
JRG 07	1	79.40	0.25	99.6
JRG 07	1	82.90	0.25	98.7
JRG 07	1	87.08	0.38	98.6
JRG 07	1	86.65	0.31	99.2
JRG 07	1	86.86	0.30	100.2
JRG 07	1	87.05	0.39	99.5
JRG 07	2	81.56	0.31	100.1
JRG 07	2	80.14	0.26	99.1
JRG 07	2	83.61	0.23	98.9
JRG 07	2	80.71	0.28	99.8
JRG 07	2	63.07	0.16	98.7
JRG 07	2	63.76	0.17	98.9
JRG 07	2	65.26	0.16	99.9
JRG 07	2	71.98	0.20	99.3
JRG 07	4	77.14	0.22	99.3
JRG 07	4	72.43	0.25	99.5
JRG 07	4	67.14	0.21	99.4
JRG 10	2	57.76	0.10	98.6
JRG 10	2	72.11	0.15	99.4

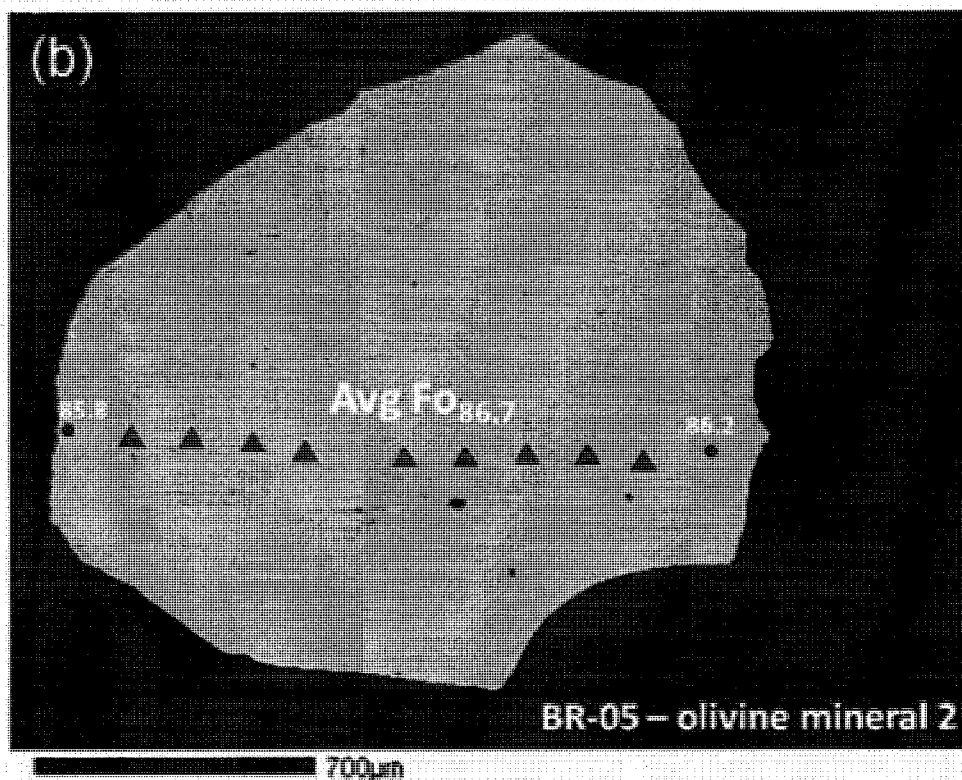
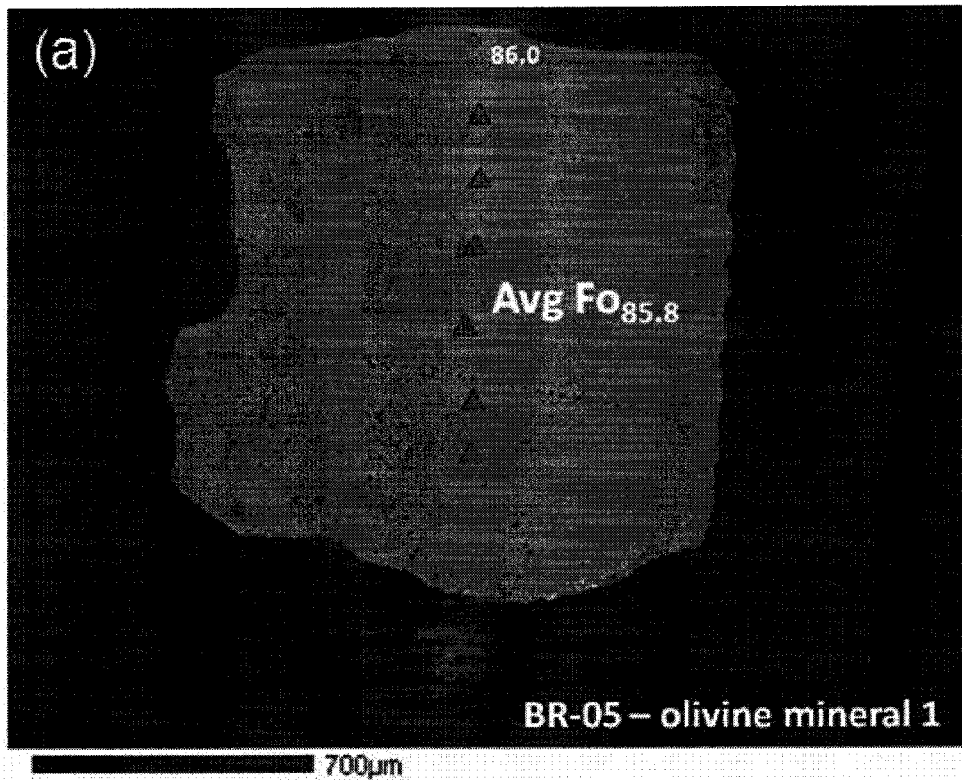


**Figure 22:** Microphotographs of BR-05 olivine #1(a) and #2(b). The triangles represent points measured of the cores, with the average forsterite compositions shown. The dots represent points measured of the rims, with each of their forsterite compositions shown.

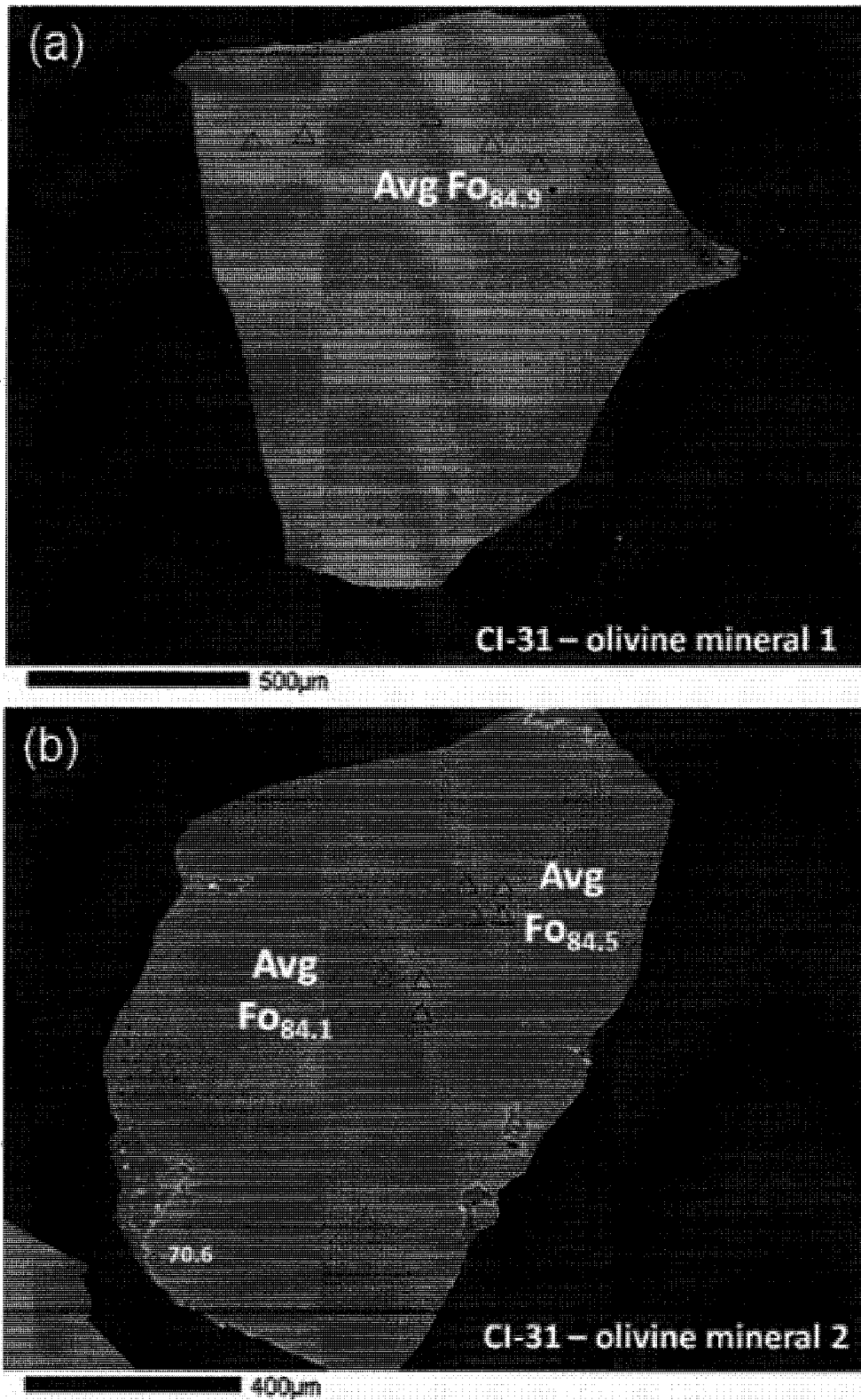


**Figure 23:** Microphotographs of CI-31 olivine #1(a) and #2(b). The triangles represent points measured of the cores, with the average forsterite compositions shown. The dots represent points measured of the rims, with each of their forsterite compositions shown.

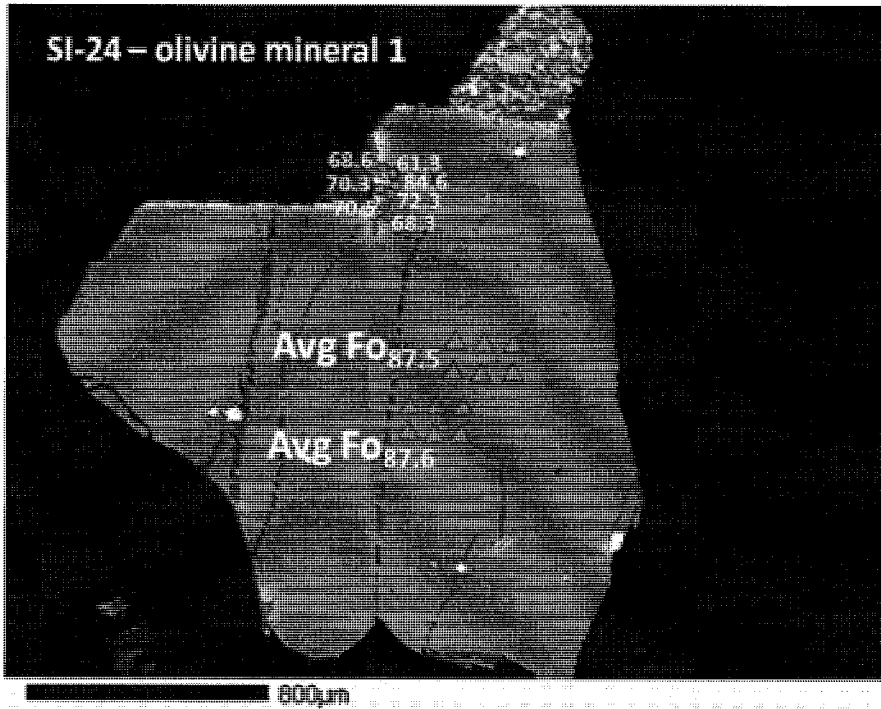


**Figure 24:**

Microphotograph of SI-24 olivine #1. The triangles represent points measured of the cores, with the average forsterite compositions shown. The dots represent points measured of the rims, with each of their forsterite compositions shown.

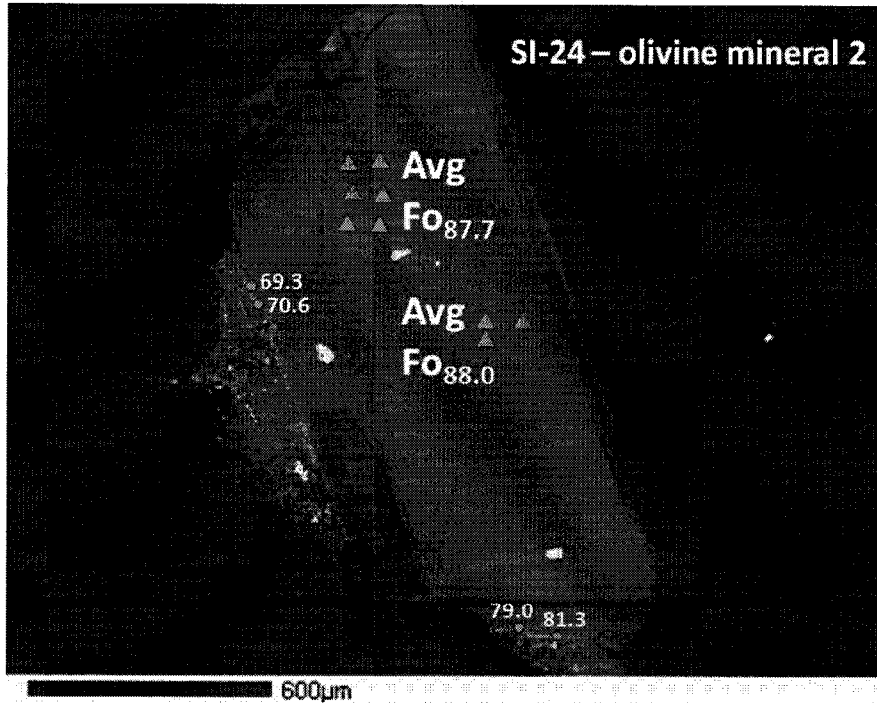


**Figure 25:**

Microphotograph of SI-24 olivine #2. The triangles represent points measured of the cores, with the average forsterite compositions shown. The dots represent points measured of the rims, with each of their forsterite compositions shown.

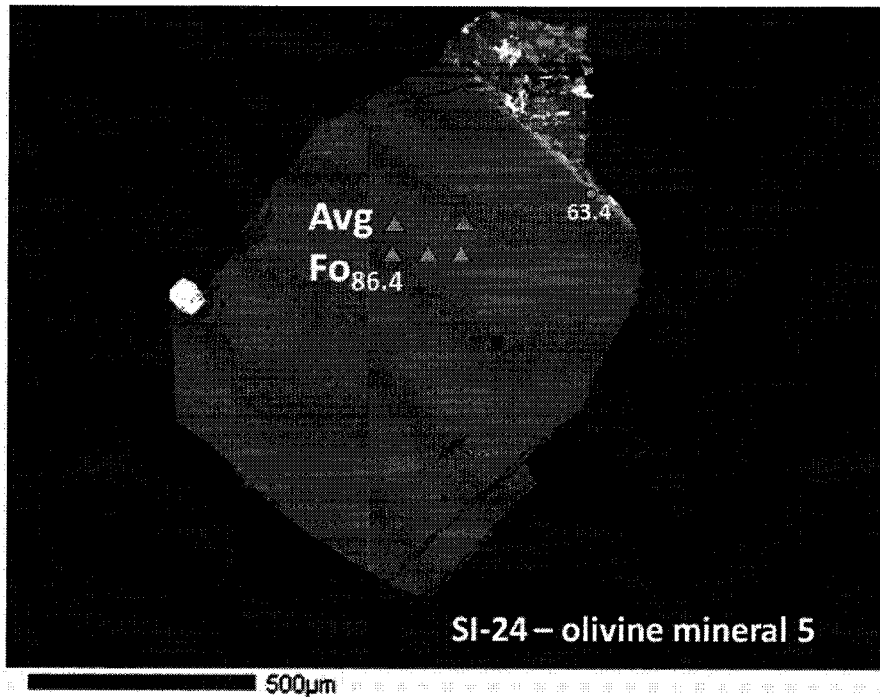


**Figure 26:**  
 Microphotograph of SI-24 olivine #5. The triangles represent points measured of the cores, with the average forsterite compositions shown. The dots represent points measured of the rims, with each of their forsterite compositions shown.

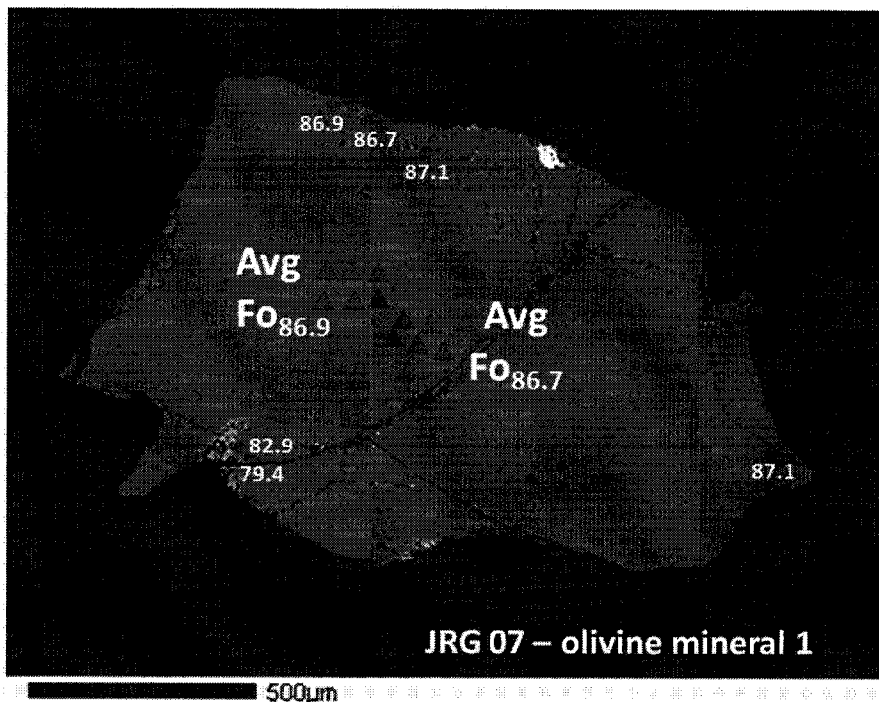


**Figure 27:**  
 Microphotograph of JRG 07 olivine #1. The triangles represent points measured of the cores, with the average forsterite compositions shown. The dots represent points measured of the rims, with each of their forsterite compositions shown.

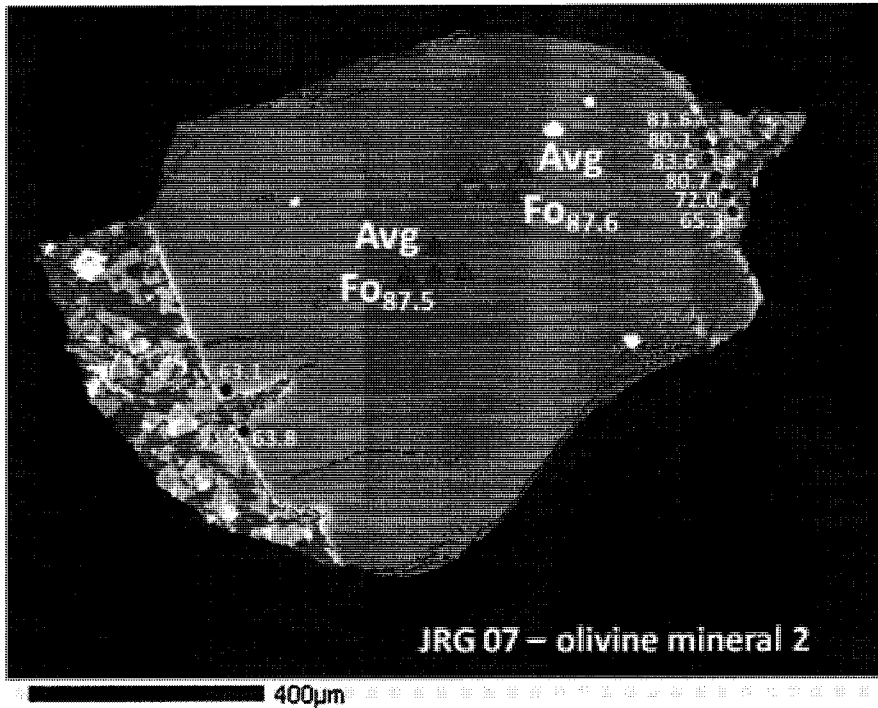


**Figure 28:**

Microphotograph of JRG 07 olivine #2. The triangles represent points measured of the cores, with the average forsterite compositions shown. The dots represent points measured of the rims, with each of their forsterite compositions shown.

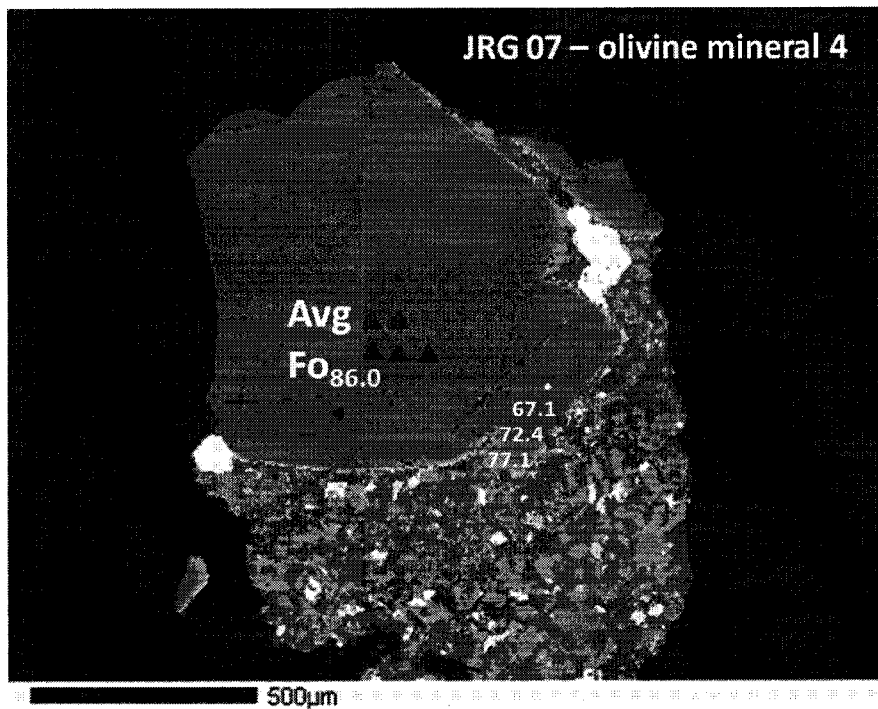


**Figure 29:**

Microphotograph of JRG 07 olivine #4. The triangles represent points measured of the cores, with the average forsterite compositions shown. The dots represent points measured of the rims, with each of their forsterite compositions shown.

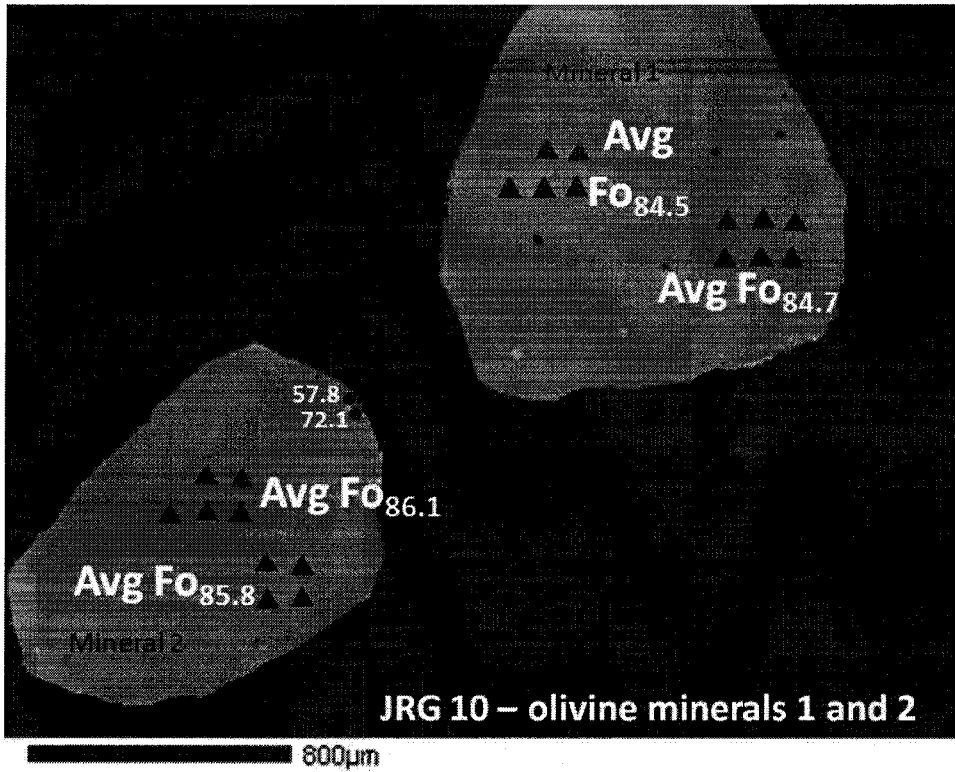


**Figure 30:** Microphotograph of JRG 10 olivine minerals #1 and #2. The triangles represent points measured of the cores, with the average forsterite compositions shown. The dots represent points measured of the rims, with each of their forsterite compositions shown.

## APPENDIX C

### MICROPROBE DATA OF TURKANA CLINOPYROXENE

Pyroxene phenocrysts of four Quaternary and Tertiary Turkana lavas were analyzed for major element compositions on a JEOL JXA-733 Superprobe at MIT. Transects of the phenocrysts were measured for SiO<sub>2</sub>, TiO<sub>2</sub>, Al<sub>2</sub>O<sub>3</sub>, Cr<sub>2</sub>O<sub>3</sub>, FeO, MnO, MgO, CaO, and Na<sub>2</sub>O weight percent (Tables 10 and 11). The major element standards used were Diopside-Jadeite (DJ35) with 56.88 wt. % SiO<sub>2</sub>, 8.82 wt. % Al<sub>2</sub>O<sub>3</sub>, 12.1 wt. % MgO, 16.83 wt. % CaO, and 5.36 wt. % Na<sub>2</sub>O and Aluminous-Orthopyroxene (ALP7) with 51.22 wt. % SiO<sub>2</sub>, 8.82 wt. % Al<sub>2</sub>O<sub>3</sub>, 14.499 wt. % FeO, and 25.797 wt. % MgO. The standards used for minor elements were Rutile (TiO<sub>2</sub>) for Ti, Uvaorite (Ca<sub>3</sub>Cr<sub>2</sub>Si<sub>3</sub>O<sub>12</sub>) for Cr, and Rhodonite (MnSiO<sub>3</sub>) for Mn. For each elemental analysis the count times ranged from 10 – 50 s. The atomic end-members were calculated for enstatite (MgSiO<sub>3</sub>), ferrosilite (FeSiO<sub>3</sub>), jadeite (NaAlSi<sub>2</sub>O<sub>6</sub>), and calcium Tschermark's pyroxene (CaTs) (CaAl<sub>2</sub>SiO<sub>6</sub>); then the enstatite, ferrosilite, and wollastonite end-members were re-normalized (Tables 12 and 13).



**Table 10:**  
Turkana Quaternary clinopyroxene atomic compositions.

Quaternary:			Atomic values									
Sample	Mineral #	Point #	Si	Ti	Al	Cr	Fe	Mn	Mg	Ca	Na	O
CI-10	4	1	1.84	0.040	0.211	0.017	0.201	0.0033	0.801	0.873	0.036	6
CI-10	4	2	1.84	0.038	0.219	0.023	0.194	0.0027	0.791	0.877	0.034	6
CI-10	4	3	1.85	0.037	0.211	0.020	0.189	0.0041	0.796	0.885	0.032	6
CI-10	4	4	1.86	0.036	0.198	0.014	0.189	0.0035	0.809	0.885	0.026	6
CI-10	4	5	1.86	0.034	0.193	0.009	0.198	0.0033	0.810	0.891	0.029	6
CI-10	4	6	1.85	0.036	0.207	0.008	0.203	0.0041	0.799	0.885	0.035	6
CI-10	4	7	1.85	0.038	0.217	0.011	0.196	0.0031	0.811	0.865	0.037	6
CI-10	4	8	1.84	0.035	0.192	0.010	0.198	0.0032	0.828	0.897	0.030	6
CI-10	4	10	1.85	0.033	0.197	0.009	0.197	0.0032	0.817	0.884	0.033	6
CI-10	4	11	1.86	0.033	0.187	0.008	0.196	0.0028	0.831	0.879	0.030	6
CI-10	4	12	1.85	0.035	0.202	0.012	0.190	0.0039	0.816	0.876	0.031	6
CI-10	4	13	1.85	0.034	0.205	0.022	0.179	0.0040	0.808	0.883	0.032	6
CI-10	4	14	1.84	0.036	0.225	0.020	0.186	0.0024	0.803	0.876	0.034	6
CI-10	4	15	1.85	0.034	0.203	0.017	0.188	0.0045	0.822	0.875	0.031	6
CI-10	4	16	1.84	0.040	0.217	0.017	0.211	0.0036	0.789	0.871	0.034	6
CI-10	5	1	1.86	0.027	0.208	0.010	0.152	0.0018	0.834	0.896	0.022	6
CI-10	5	2	1.86	0.029	0.205	0.009	0.167	0.0027	0.836	0.893	0.020	6
CI-10	5	3	1.86	0.029	0.204	0.008	0.164	0.0013	0.843	0.892	0.025	6
CI-10	5	4	1.86	0.029	0.203	0.008	0.163	0.0032	0.840	0.886	0.027	6
CI-10	5	5	1.85	0.027	0.216	0.013	0.161	0.0027	0.838	0.888	0.021	6
CI-10	5	6	1.86	0.028	0.214	0.009	0.160	0.0020	0.839	0.882	0.024	6
CI-10	5	7	1.84	0.031	0.224	0.009	0.165	0.0024	0.831	0.897	0.023	6
CI-10	5	8	1.84	0.029	0.213	0.010	0.164	0.0021	0.843	0.899	0.021	6
CI-10	5	9	1.85	0.030	0.223	0.012	0.166	0.0029	0.825	0.887	0.028	6
KCH-19	1	1a	1.85	0.031	0.215	0.022	0.175	0.0033	0.820	0.874	0.028	6
KCH-19	1	2a	1.82	0.032	0.263	0.024	0.165	0.0025	0.798	0.875	0.054	6
KCH-19	1	3a	1.80	0.038	0.311	0.007	0.202	0.0037	0.764	0.865	0.038	6
KCH-19	1	4a	1.83	0.037	0.235	0.012	0.176	0.0013	0.807	0.890	0.029	6
KCH-19	1	5a	1.83	0.037	0.242	0.008	0.175	0.0025	0.800	0.902	0.032	6
KCH-19	1	6a	1.84	0.035	0.235	0.009	0.163	0.0020	0.814	0.897	0.030	6
KCH-19	1	7a	1.82	0.038	0.242	0.008	0.176	0.0021	0.807	0.910	0.023	6
KCH-19	1	9a	1.83	0.038	0.229	0.008	0.169	0.0024	0.805	0.913	0.042	6
KCH-19	1	10a	1.80	0.038	0.308	0.006	0.200	0.0008	0.774	0.864	0.039	6
KCH-19	1	11a	1.82	0.037	0.241	0.011	0.168	0.0019	0.814	0.916	0.023	6
KCH-19	1	12a	1.83	0.037	0.231	0.008	0.171	0.0023	0.821	0.906	0.026	6

Table 10 - Continued

PYROXENE TRANSECTS			Atomic values									
Quaternary:			Si	Ti	Al	Cr	Fe	Mn	Mg	Ca	Na	O
Sample	Mineral #	Point #										
KCH-19	1	1b	1.90	0.035	0.133	0.001	0.217	0.0049	0.803	0.898	0.024	6
KCH-19	1	2b	1.88	0.048	0.146	0.001	0.273	0.0066	0.731	0.890	0.034	6
KCH-19	1	3b	1.85	0.066	0.165	0.001	0.328	0.0076	0.675	0.882	0.041	6
KCH-19	1	4b	1.84	0.038	0.242	0.007	0.168	0.0049	0.786	0.903	0.027	6
KCH-19	1	5b	1.84	0.034	0.217	0.005	0.169	0.0036	0.825	0.918	0.023	6
KCH-19	1	6b	1.80	0.042	0.294	0.004	0.204	0.0040	0.770	0.881	0.031	6
KCH-19	1	7b	1.85	0.031	0.201	0.005	0.167	0.0045	0.834	0.915	0.024	6
KCH-19	1	8b	1.84	0.036	0.225	0.008	0.162	0.0037	0.816	0.907	0.024	6
KCH-19	1	9b	1.83	0.038	0.248	0.004	0.170	0.0068	0.805	0.898	0.024	6
KCH-19	1	10b	1.83	0.034	0.227	0.004	0.168	0.0040	0.825	0.907	0.028	6
KCH-19	4	1a	1.83	0.035	0.262	0.013	0.164	0.0026	0.796	0.889	0.028	6
KCH-19	4	2a	1.83	0.034	0.260	0.013	0.162	0.0021	0.768	0.908	0.027	6
KCH-19	4	3a	1.84	0.032	0.252	0.011	0.165	0.0025	0.789	0.888	0.028	6
KCH-19	4	4a	1.82	0.033	0.263	0.013	0.171	0.0026	0.817	0.885	0.024	6
KCH-19	4	5a	1.86	0.019	0.212	0.028	0.137	0.0027	0.872	0.855	0.031	6
KCH-19	4	6a	1.82	0.031	0.256	0.026	0.165	0.0030	0.794	0.903	0.028	6
KCH-19	4	8a	1.80	0.067	0.238	0.004	0.241	0.0033	0.741	0.900	0.036	6
KCH-19	4	1b	1.84	0.070	0.183	0.002	0.279	0.0059	0.691	0.917	0.042	6
KCH-19	4	2b	1.88	0.044	0.130	0.001	0.247	0.0064	0.782	0.900	0.026	6
KCH-19	4	3b	1.88	0.031	0.156	0.006	0.175	0.0050	0.849	0.887	0.024	6
KCH-19	4	4b	1.86	0.035	0.199	0.008	0.172	0.0039	0.810	0.893	0.025	6
KCH-19	4	5b	1.88	0.032	0.156	0.006	0.188	0.0049	0.844	0.876	0.023	6
KCH-19	4	6b	1.89	0.031	0.133	0.005	0.191	0.0059	0.853	0.885	0.021	6
KCH-19	4	7b	1.82	0.037	0.273	0.007	0.172	0.0032	0.784	0.902	0.024	6
KCH-19	4	8b	1.84	0.032	0.262	0.007	0.167	0.0056	0.801	0.858	0.030	6
KCH-19	4	9b	1.84	0.032	0.248	0.006	0.169	0.0034	0.794	0.899	0.027	6
KCH-19	4	10b	1.83	0.032	0.245	0.007	0.163	0.0040	0.815	0.901	0.027	6
KCH-19	4	11b	1.85	0.030	0.237	0.006	0.162	0.0040	0.809	0.894	0.023	6
KCH-19	4	12b	1.85	0.033	0.247	0.006	0.159	0.0039	0.784	0.901	0.029	6
KCH-19	6	1	1.84	0.030	0.242	0.011	0.166	0.0018	0.807	0.885	0.027	6
KCH-19	6	2	1.83	0.028	0.228	0.012	0.169	0.0022	0.831	0.898	0.028	6
KCH-19	6	3	1.85	0.026	0.210	0.013	0.168	0.0028	0.826	0.894	0.027	6
KCH-19	6	4	1.85	0.020	0.245	0.010	0.158	0.0035	0.841	0.844	0.055	6
KCH-19	6	5	1.85	0.021	0.242	0.011	0.159	0.0024	0.857	0.848	0.037	6
KCH-19	6	6	1.84	0.022	0.241	0.012	0.167	0.0027	0.856	0.837	0.052	6

**Table 11:**  
Turkana Tertiary Clinopyroxene atomic compositions.

**PYROXENE TRANSECTS**

Tertiary:			Atomic values									
Sample	Mineral #	Point #	Si	Ti	Al	Cr	Fe	Mn	Mg	Ca	Na	O
KJ 1	1	1a	1.83	0.049	0.245	0.002	0.173	0.0007	0.774	0.906	0.052	6
KJ 1	1	2a	1.89	0.030	0.148	0.010	0.154	0.0019	0.851	0.884	0.043	6
KJ 1	1	3a	1.83	0.048	0.249	0.002	0.175	0.0015	0.788	0.890	0.043	6
KJ 1	1	4a	1.82	0.048	0.249	0.002	0.173	0.0012	0.782	0.900	0.055	6
KJ 1	1	5a	1.83	0.048	0.247	0.003	0.180	0.0023	0.779	0.882	0.051	6
KJ 1	1	6a	1.82	0.047	0.252	0.002	0.170	0.0017	0.775	0.906	0.054	6
KJ 1	1	7a	1.83	0.047	0.252	0.001	0.174	0.0010	0.773	0.900	0.050	6
KJ 1	1	8a	1.82	0.048	0.250	0.002	0.176	0.0010	0.778	0.904	0.045	6
KJ 1	1	9a	1.83	0.047	0.250	0.002	0.172	0.0021	0.768	0.905	0.047	6
KJ 1	1	10a	1.83	0.048	0.253	0.002	0.174	0.0020	0.772	0.888	0.055	6
KJ 1	1	11a	1.82	0.048	0.252	0.002	0.172	0.0028	0.780	0.905	0.050	6
KJ 1	1	1b	1.75	0.089	0.266	0.000	0.257	0.0043	0.682	0.964	0.038	6
KJ 1	1	2b	1.80	0.072	0.216	0.000	0.230	0.0040	0.749	0.930	0.035	6
KJ 1	1	3b	1.78	0.078	0.240	0.000	0.235	0.0047	0.709	0.950	0.034	6
KJ 1	1	4b	1.80	0.072	0.222	0.000	0.224	0.0040	0.723	0.948	0.036	6
KJ 1	1	5b	1.84	0.053	0.173	0.000	0.226	0.0044	0.780	0.929	0.038	6
KJ 1	1	6b	1.62	0.142	0.419	0.000	0.264	0.0049	0.596	0.953	0.044	6
KJ 1	1	7b	1.62	0.137	0.416	0.000	0.262	0.0031	0.616	0.954	0.041	6
KJ 1	1	8b	1.81	0.047	0.249	0.001	0.165	0.0021	0.789	0.923	0.049	6
KJ 1	1	9b	1.82	0.046	0.244	0.001	0.171	0.0013	0.778	0.919	0.049	6
KJ 1	1	12b	1.82	0.048	0.246	0.000	0.173	0.0016	0.775	0.909	0.056	6
KJ 1	1	13b	1.82	0.047	0.246	0.001	0.174	0.0018	0.784	0.910	0.056	6
KJ 1	1	14b	1.83	0.048	0.249	0.001	0.174	0.0020	0.767	0.912	0.047	6
KJ 1	1	15b	1.82	0.047	0.249	0.000	0.169	0.0026	0.785	0.917	0.055	6
KJ 1	1	16b	1.82	0.047	0.249	0.001	0.174	0.0027	0.776	0.909	0.056	6
KJ 1	2	1a	1.82	0.056	0.244	0.002	0.199	0.0028	0.750	0.912	0.039	6
KJ 1	2	2a	1.83	0.052	0.216	0.005	0.178	0.0019	0.775	0.941	0.033	6
KJ 1	2	3a	1.81	0.058	0.240	0.005	0.185	0.0025	0.755	0.934	0.040	6
KJ 1	2	4a	1.82	0.055	0.229	0.003	0.184	0.0016	0.776	0.922	0.043	6
KJ 1	2	5a	1.82	0.054	0.224	0.004	0.189	0.0021	0.770	0.925	0.046	6
KJ 1	2	6a	1.83	0.051	0.225	0.002	0.198	0.0015	0.758	0.920	0.053	6
KJ 1	2	7a	1.80	0.057	0.247	0.002	0.203	0.0011	0.759	0.922	0.040	6
KJ 1	2	8a	1.79	0.060	0.244	0.004	0.191	0.0013	0.770	0.933	0.047	6

Table 11 - Continued

PYROXENE TRANSECTS

Tertiary:			Atomic values									
Sample	Mineral #	Point #	Si	Ti	Al	Cr	Fe	Mn	Mg	Ca	Na	O
KJ 1	2	1b	1.63	0.136	0.412	0.001	0.270	0.0040	0.609	0.945	0.045	6
KJ 1	2	2b	1.75	0.073	0.298	0.000	0.233	0.0047	0.704	0.943	0.040	6
KJ 1	2	3b	1.80	0.058	0.254	0.000	0.210	0.0027	0.743	0.934	0.043	6
KJ 1	2	4b	1.77	0.075	0.224	0.000	0.246	0.0044	0.747	0.952	0.037	6
KJ 1	2	5b	1.76	0.082	0.231	0.001	0.255	0.0055	0.735	0.949	0.040	6
KJ 1	2	7b	1.85	0.053	0.171	0.000	0.212	0.0041	0.752	0.952	0.044	6
KJ 1	2	8b	1.66	0.108	0.370	0.000	0.271	0.0053	0.669	0.934	0.050	6
KJ 1	2	9b	1.81	0.056	0.241	0.001	0.186	0.0033	0.774	0.930	0.044	6
KJ 1	2	10b	1.81	0.054	0.242	0.002	0.192	0.0024	0.760	0.925	0.046	6
KJ 1	2	11b	1.83	0.053	0.224	0.002	0.187	0.0027	0.752	0.931	0.045	6
KJ 1	2	12b	1.80	0.058	0.252	0.002	0.189	0.0028	0.752	0.936	0.046	6
KJ 1	2	13b	1.83	0.049	0.226	0.001	0.192	0.0042	0.775	0.914	0.051	6
KJ 1	2	14b	1.82	0.051	0.227	0.001	0.183	0.0029	0.777	0.931	0.041	6
KJ 1	2	15b	1.81	0.055	0.238	0.002	0.187	0.0032	0.764	0.925	0.043	6
KJ 1	5	1	1.82	0.049	0.257	0.004	0.168	0.0014	0.770	0.898	0.048	6
KJ 1	5	2	1.82	0.048	0.251	0.007	0.171	0.0018	0.770	0.901	0.050	6
KJ 1	5	3	1.84	0.041	0.229	0.007	0.168	0.0009	0.793	0.896	0.053	6
KJ 1	5	4	1.85	0.040	0.217	0.006	0.167	0.0029	0.804	0.899	0.044	6
KJ 1	5	5	1.85	0.039	0.210	0.007	0.167	0.0024	0.806	0.895	0.056	6
KJ 1	5	6	1.87	0.039	0.208	0.007	0.171	0.0019	0.791	0.875	0.048	6
JRG 07	2	1a	1.89	0.042	0.141	0.001	0.253	0.0050	0.771	0.874	0.039	6
JRG 07	2	2a	1.87	0.051	0.159	0.000	0.247	0.0044	0.770	0.888	0.036	6
JRG 07	2	3a	1.88	0.045	0.134	0.001	0.241	0.0033	0.783	0.901	0.043	6
JRG 07	2	4a	1.90	0.021	0.124	0.007	0.155	0.0024	0.883	0.900	0.025	6
JRG 07	2	5a	1.93	0.021	0.099	0.008	0.150	0.0022	0.895	0.879	0.021	6
JRG 07	2	6a	1.92	0.023	0.103	0.007	0.152	0.0019	0.895	0.890	0.023	6
JRG 07	2	7a	1.88	0.043	0.145	0.000	0.247	0.0050	0.785	0.881	0.036	6
JRG 07	2	8a	1.92	0.023	0.111	0.008	0.162	0.0031	0.877	0.892	0.015	6
JRG 07	2	9a	1.91	0.023	0.101	0.007	0.164	0.0020	0.910	0.887	0.019	6
JRG 07	2	10a	1.91	0.025	0.119	0.007	0.164	0.0028	0.867	0.890	0.026	6
JRG 07	2	11a	1.85	0.055	0.182	0.001	0.249	0.0056	0.765	0.886	0.039	6
JRG 07	2	12a	1.90	0.026	0.132	0.016	0.178	0.0033	0.853	0.876	0.025	6

Table 11 - Continued

Tertiary:			Atomic values									
Sample	Mineral #	Point #	Si	Ti	Al	Cr	Fe	Mn	Mg	Ca	Na	O
JRG 07	2	1b	1.88	0.046	0.147	0.001	0.247	0.0067	0.769	0.877	0.037	6
JRG 07	2	2b	1.87	0.049	0.145	0.001	0.249	0.0085	0.783	0.893	0.034	6
JRG 07	2	3b	1.87	0.049	0.146	0.001	0.247	0.0047	0.786	0.885	0.034	6
JRG 07	2	4b	1.88	0.044	0.147	0.001	0.241	0.0066	0.777	0.892	0.038	6
JRG 07	2	5b	1.87	0.048	0.148	0.001	0.248	0.0069	0.779	0.894	0.035	6
JRG 07	2	6b	1.88	0.043	0.145	0.001	0.247	0.0063	0.791	0.885	0.035	6
JRG 07	2	7b	1.91	0.023	0.126	0.009	0.160	0.0037	0.874	0.893	0.022	6
JRG 07	2	8b	1.91	0.022	0.119	0.008	0.158	0.0033	0.874	0.897	0.024	6
JRG 07	2	9b	1.92	0.020	0.108	0.007	0.154	0.0035	0.894	0.891	0.026	6
JRG 07	2	10b	1.94	0.018	0.095	0.014	0.139	0.0040	0.894	0.876	0.020	6
JRG 07	2	11b	1.91	0.021	0.122	0.010	0.155	0.0036	0.891	0.886	0.023	6
JRG 07	2	12b	1.93	0.021	0.110	0.007	0.162	0.0032	0.875	0.873	0.022	6
JRG 07	2	13b	1.92	0.025	0.147	0.012	0.164	0.0035	0.867	0.835	0.020	6
JRG 07	2	14b	1.90	0.023	0.133	0.010	0.155	0.0030	0.877	0.899	0.023	6
JRG 07	2	15b	1.88	0.025	0.136	0.009	0.158	0.0040	0.903	0.884	0.029	6
JRG 07	3	1	1.83	0.040	0.281	0.003	0.234	0.0048	0.751	0.819	0.057	6
JRG 07	3	2	1.84	0.041	0.201	0.008	0.203	0.0045	0.815	0.879	0.028	6
JRG 07	3	3	1.86	0.035	0.173	0.010	0.188	0.0048	0.829	0.892	0.028	6
JRG 07	3	4	1.90	0.032	0.115	0.001	0.278	0.0099	0.790	0.860	0.038	6
JRG 07	3	5	1.92	0.028	0.104	0.000	0.275	0.0105	0.787	0.865	0.036	6
JRG 07	3	6	1.92	0.026	0.098	0.001	0.274	0.0097	0.786	0.870	0.037	6
JRG 07	3	7	1.88	0.042	0.142	0.001	0.265	0.0093	0.790	0.866	0.038	6
JRG 07	3	8	1.89	0.035	0.122	0.001	0.261	0.0083	0.799	0.881	0.032	6
JRG 07	3	9	1.88	0.043	0.147	0.000	0.255	0.0069	0.806	0.858	0.032	6
JRG 07	5	1a	1.86	0.035	0.184	0.016	0.176	0.0023	0.837	0.890	0.026	6
JRG 07	5	2a	1.86	0.035	0.179	0.016	0.182	0.0033	0.826	0.886	0.029	6
JRG 07	5	3a	1.86	0.036	0.178	0.014	0.193	0.0032	0.824	0.872	0.054	6
JRG 07	5	4a	1.86	0.033	0.187	0.021	0.174	0.0029	0.829	0.882	0.028	6
JRG 07	5	5a	1.85	0.034	0.183	0.018	0.177	0.0027	0.841	0.884	0.033	6
JRG 07	5	6a	1.88	0.029	0.170	0.008	0.174	0.0025	0.852	0.884	0.023	6
JRG 07	5	7a	1.91	0.022	0.100	0.017	0.190	0.0040	0.921	0.839	0.017	6
JRG 07	5	8a	1.89	0.022	0.131	0.028	0.165	0.0036	0.877	0.874	0.022	6
JRG 07	5	9a	1.87	0.030	0.175	0.020	0.188	0.0037	0.823	0.873	0.032	6
JRG 07	5	10a	1.91	0.022	0.096	0.013	0.180	0.0039	0.912	0.862	0.027	6
JRG 07	5	11a	1.92	0.020	0.094	0.015	0.177	0.0042	0.916	0.853	0.024	6
JRG 07	5	12a	1.89	0.024	0.146	0.015	0.173	0.0016	0.866	0.880	0.025	6

**Table 11 - Continued**

Tertiary:			Atomic values									
Sample	Mineral #	Point #	Si	Ti	Al	Cr	Fe	Mn	Mg	Ca	Na	O
JRG 07	5	1b	1.91	0.019	0.115	0.017	0.151	0.0037	0.906	0.865	0.024	6
JRG 07	5	2b	1.92	0.018	0.114	0.015	0.149	0.0046	0.905	0.868	0.021	6
JRG 07	5	3b	1.87	0.031	0.182	0.015	0.193	0.0047	0.832	0.866	0.028	6
JRG 07	5	4b	1.91	0.020	0.120	0.011	0.163	0.0043	0.884	0.881	0.022	6
JRG 07	5	5b	1.90	0.020	0.114	0.014	0.158	0.0023	0.920	0.874	0.021	6
JRG 07	5	6b	1.88	0.030	0.175	0.003	0.186	0.0050	0.801	0.903	0.024	6
JRG 07	5	7b	1.86	0.032	0.183	0.011	0.178	0.0045	0.844	0.886	0.029	6
JRG 07	5	8b	1.84	0.047	0.191	0.009	0.200	0.0054	0.823	0.876	0.036	6
JRG 07	5	9b	1.85	0.045	0.189	0.010	0.200	0.0049	0.794	0.893	0.031	6
JRG 07	5	10b	1.95	0.015	0.076	0.012	0.148	0.0053	0.947	0.827	0.021	6
JRG 07	5	11b	1.92	0.025	0.103	0.007	0.184	0.0033	0.884	0.861	0.022	6
JRG 07	5	12b	1.89	0.027	0.153	0.012	0.170	0.0047	0.857	0.885	0.023	6
JRG 07	5	13b	1.86	0.042	0.169	0.002	0.241	0.0057	0.794	0.891	0.027	6
JRG 07	5	14b	1.87	0.027	0.159	0.011	0.183	0.0042	0.871	0.881	0.029	6

**Table 12:**

Turkana Quaternary clinopyroxene end-member compositions.  $Fe^* = FeT + Mn$ . The En(Mg) end-member is the enstatite ( $MgSiO_3$ ) composition, the Fs( $Fe^*$ ) end-member is ferrosilite ( $FeSiO_3$ ), Wo(Ca) end-member is wollastonite ( $CaSiO_3$ ), and other is Jadeite ( $NaAlSi_2O_6$ ) and CaTs ( $CaAl_2SiO_6$ ).  $Wo(Ca) = Ca - CaTs$ .

**PYROXENE TRANSECTS**

Quaternary:			End-member mole percentages				Normalized end-members		
Sample	Mineral #	Point #	En(Mg)	Fs( $Fe^*$ )	Wo(Ca)	Other	En(Mg)	Fs( $Fe^*$ )	Wo(Ca)
CI-10	4	1	41.86	10.65	41.05	6.45	44.74	11.38	43.88
CI-10	4	2	41.65	10.36	41.31	6.68	44.63	11.10	44.27
CI-10	4	3	41.80	10.11	41.73	6.36	44.64	10.80	44.56
CI-10	4	4	42.28	10.05	41.82	5.85	44.91	10.68	44.41
CI-10	4	5	41.94	10.44	41.90	5.73	44.49	11.07	44.44
CI-10	4	6	41.48	10.77	41.49	6.27	44.25	11.49	44.26
CI-10	4	7	42.41	10.40	40.54	6.64	45.43	11.14	43.43
CI-10	4	8	42.34	10.27	41.73	5.66	44.88	10.89	44.23
CI-10	4	10	42.26	10.33	41.48	5.92	44.93	10.99	44.09
CI-10	4	11	42.88	10.25	41.27	5.59	45.42	10.86	43.72
CI-10	4	12	42.56	10.10	41.27	6.07	45.32	10.75	43.93
CI-10	4	13	42.40	9.58	41.79	6.22	45.22	10.22	44.57
CI-10	4	14	42.24	9.90	41.07	6.79	45.32	10.62	44.06
CI-10	4	15	42.82	10.01	41.07	6.10	45.60	10.66	43.74
CI-10	4	16	41.33	11.26	40.83	6.58	44.24	12.05	43.71
CI-10	5	1	43.78	8.05	42.12	6.05	46.60	8.57	44.83
CI-10	5	2	43.58	8.85	41.72	5.86	46.29	9.40	44.31
CI-10	5	3	43.82	8.58	41.66	5.94	46.59	9.12	44.29
CI-10	5	4	43.78	8.64	41.59	5.99	46.56	9.19	44.24
CI-10	5	5	43.87	8.59	41.35	6.19	46.76	9.16	44.08
CI-10	5	6	43.98	8.51	41.28	6.23	46.90	9.07	44.02
CI-10	5	7	43.31	8.72	41.54	6.43	46.29	9.32	44.39
CI-10	5	8	43.71	8.59	41.63	6.07	46.53	9.14	44.32
CI-10	5	9	43.25	8.82	41.35	6.57	46.29	9.45	44.26
KCH-19	1	1a	43.15	9.36	41.09	6.40	46.10	10.00	43.90
KCH-19	1	2a	42.14	8.83	40.65	8.37	45.99	9.64	44.37
KCH-19	1	3a	40.78	10.98	38.93	9.31	44.97	12.10	42.93
KCH-19	1	4a	42.39	9.33	41.36	6.92	45.54	10.02	44.44
KCH-19	1	5a	41.88	9.27	41.69	7.16	45.11	9.99	44.90
KCH-19	1	6a	42.69	8.64	41.71	6.95	45.89	9.29	44.83
KCH-19	1	7a	42.06	9.29	41.73	6.92	45.19	9.98	44.83
KCH-19	1	9a	41.69	8.85	42.44	7.02	44.84	9.52	45.64
KCH-19	1	10a	41.21	10.70	38.85	9.24	45.41	11.79	42.80
KCH-19	1	11a	42.30	8.83	42.00	6.87	45.42	9.48	45.10
KCH-19	1	12a	42.61	9.01	41.72	6.66	45.65	9.65	44.69

Table 12 - Continued

PYROXENE TRANSECTS

Quaternary:			End-member mole percentages				Normalized end-members		
Sample	Mineral #	Point #	En(Mg)	Fs(Fe*)	Wo(Ca)	Other	En(Mg)	Fs(Fe*)	Wo(Ca)
KCH-19	1	1b	41.25	11.39	43.33	4.03	42.98	11.87	45.15
KCH-19	1	2b	37.77	14.48	43.11	4.64	39.61	15.18	45.21
KCH-19	1	3b	34.92	17.34	42.41	5.32	36.89	18.31	44.80
KCH-19	1	4b	41.62	9.15	42.13	7.10	44.80	9.85	45.35
KCH-19	1	5b	42.56	8.90	42.36	6.18	45.37	9.48	45.15
KCH-19	1	6b	40.75	11.01	39.66	8.59	44.58	12.04	43.38
KCH-19	1	7b	42.89	8.82	42.52	5.77	45.52	9.36	45.13
KCH-19	1	8b	42.66	8.66	42.18	6.50	45.62	9.26	45.11
KCH-19	1	9b	42.29	9.26	41.30	7.14	45.55	9.98	44.48
KCH-19	1	10b	42.71	8.90	41.80	6.59	45.72	9.53	44.75
KCH-19	4	1a	42.37	8.86	41.07	7.70	45.91	9.59	44.49
KCH-19	4	2a	41.14	8.80	42.40	7.67	44.56	9.53	45.92
KCH-19	4	3a	42.15	8.94	41.45	7.46	45.55	9.66	44.79
KCH-19	4	4a	43.02	9.14	40.30	7.54	46.53	9.89	43.58
KCH-19	4	5a	45.94	7.37	40.29	6.40	49.08	7.88	43.04
KCH-19	4	6a	41.96	8.87	41.69	7.48	45.35	9.59	45.06
KCH-19	4	8a	38.59	12.70	41.58	7.13	41.55	13.68	44.77
KCH-19	4	1b	35.72	14.73	43.76	5.79	37.92	15.64	46.45
KCH-19	4	2b	39.86	12.91	43.26	3.96	41.51	13.45	45.05
KCH-19	4	3b	43.77	9.28	42.33	4.63	45.89	9.73	44.38
KCH-19	4	4b	42.53	9.26	42.33	5.88	45.19	9.83	44.98
KCH-19	4	5b	43.60	9.96	41.82	4.62	45.71	10.45	43.84
KCH-19	4	6b	43.59	10.09	42.39	3.93	45.38	10.50	44.12
KCH-19	4	7b	41.57	9.28	41.26	7.88	45.13	10.08	44.79
KCH-19	4	8b	43.04	9.29	39.83	7.85	46.70	10.08	43.22
KCH-19	4	9b	41.96	9.11	41.67	7.26	45.24	9.83	44.93
KCH-19	4	10b	42.68	8.72	41.48	7.12	45.95	9.39	44.66
KCH-19	4	11b	42.76	8.77	41.58	6.89	45.92	9.42	44.66
KCH-19	4	12b	41.77	8.68	42.21	7.34	45.08	9.36	45.56
KCH-19	6	1	42.75	8.89	41.21	7.14	46.04	9.58	44.38
KCH-19	6	2	43.09	8.87	41.40	6.64	46.16	9.50	44.35
KCH-19	6	3	43.10	8.90	41.83	6.18	45.93	9.48	44.58
KCH-19	6	4	44.23	8.47	39.42	7.88	48.02	9.19	42.79
KCH-19	6	5	45.03	8.49	39.16	7.31	48.58	9.17	42.25
KCH-19	6	6	44.72	8.87	38.78	7.64	48.42	9.60	41.98



**Table 13:**

Turkana Tertiary clinopyroxene end-member compositions.  $Fe^* = Fe_T + Mn$ . The En(Mg) end-member is the enstatite ( $MgSiO_3$ ) composition, the Fs( $Fe^*$ ) end-member is ferrosilite ( $FeSiO_3$ ), Wo(Ca) end-member is wollastonite ( $CaSiO_3$ ), and other is Jadeite ( $NaAlSi_2O_6$ ) and CaTs ( $CaAl_2SiO_6$ ).  $Wo(Ca) = Ca - CaTs$ .

**PYROXENE TRANSECTS**

Tertiary:			End-member mole percentages				Normalized end-members		
Sample	Mineral #	Point #	En(Mg)	Fs( $Fe^*$ )	Wo(Ca)	Other	En(Mg)	Fs( $Fe^*$ )	Wo(Ca)
KJ 1	1	1a	40.61	9.12	42.48	7.78	44.04	9.89	46.06
KJ 1	1	2a	44.00	8.06	42.99	4.95	46.29	8.48	45.23
KJ 1	1	3a	41.53	9.30	41.47	7.70	45.00	10.07	44.93
KJ 1	1	4a	40.92	9.12	42.00	7.96	44.46	9.91	45.63
KJ 1	1	5a	41.12	9.61	41.38	7.88	44.64	10.43	44.92
KJ 1	1	6a	40.65	8.98	42.35	8.02	44.20	9.76	46.04
KJ 1	1	7a	40.72	9.21	42.14	7.94	44.23	10.00	45.77
KJ 1	1	8a	40.84	9.31	42.11	7.74	44.27	10.09	45.64
KJ 1	1	9a	40.54	9.17	42.45	7.84	43.99	9.95	46.07
KJ 1	1	10a	40.83	9.29	41.74	8.14	44.45	10.11	45.44
KJ 1	1	11a	40.83	9.15	42.12	7.90	44.34	9.93	45.73
KJ 1	1	1b	35.06	13.41	43.70	7.82	38.04	14.55	47.41
KJ 1	1	2b	38.46	12.00	43.12	6.42	41.10	12.82	46.08
KJ 1	1	3b	36.68	12.42	43.81	7.09	39.48	13.37	47.16
KJ 1	1	4b	37.37	11.79	44.17	6.67	40.04	12.64	47.33
KJ 1	1	5b	39.47	11.63	43.57	5.33	41.69	12.29	46.02
KJ 1	1	6b	32.03	14.44	41.10	12.44	36.57	16.49	46.94
KJ 1	1	7b	32.84	14.11	40.88	12.18	37.39	16.07	46.55
KJ 1	1	8b	40.92	8.66	42.70	7.72	44.34	9.39	46.27
KJ 1	1	9b	40.58	8.96	42.83	7.63	43.93	9.70	46.37
KJ 1	1	12b	40.50	9.10	42.51	7.89	43.97	9.88	46.15
KJ 1	1	13b	40.72	9.12	42.34	7.83	44.18	9.89	45.93
KJ 1	1	14b	40.32	9.26	42.64	7.78	43.72	10.04	46.24
KJ 1	1	15b	40.70	8.92	42.52	7.87	44.17	9.68	46.15
KJ 1	1	16b	40.47	9.20	42.38	7.94	43.97	9.99	46.04
KJ 1	2	1a	39.43	10.59	42.55	7.43	42.59	11.44	45.97
KJ 1	2	2a	40.19	9.33	44.03	6.45	42.96	9.97	47.07
KJ 1	2	3a	39.40	9.78	43.50	7.32	42.52	10.55	46.94
KJ 1	2	4a	40.31	9.63	43.01	7.06	43.37	10.36	46.27
KJ 1	2	5a	39.86	9.91	43.25	6.98	42.85	10.65	46.50
KJ 1	2	6a	39.28	10.35	43.19	7.18	42.32	11.15	46.53
KJ 1	2	7a	39.42	10.60	42.54	7.44	42.59	11.45	45.96
KJ 1	2	8a	39.65	9.92	42.94	7.50	42.86	10.72	46.42

Table 13 - Continued

PYROXENE TRANSECTS

Tertiary:			End-member mole percentages				Normalized end-members		
Sample	Mineral #	Point #	En(Mg)	Fs(Fe*)	Wo(Ca)	Other	En(Mg)	Fs(Fe*)	Wo(Ca)
KJ 1	2	1b	32.52	14.61	40.67	12.20	37.04	16.64	46.32
KJ 1	2	2b	36.56	12.35	42.30	8.79	40.08	13.54	46.38
KJ 1	2	3b	38.44	11.02	42.87	7.67	41.63	11.93	46.43
KJ 1	2	4b	37.60	12.62	43.23	6.55	40.24	13.50	46.26
KJ 1	2	5b	37.03	13.11	43.03	6.83	39.75	14.07	46.19
KJ 1	2	7b	38.30	11.00	45.22	5.48	40.52	11.64	47.84
KJ 1	2	8b	34.67	14.34	40.12	10.87	38.91	16.08	45.01
KJ 1	2	9b	39.95	9.76	42.93	7.36	43.12	10.54	46.34
KJ 1	2	10b	39.48	10.10	42.94	7.48	42.67	10.91	46.41
KJ 1	2	11b	39.21	9.91	43.86	7.01	42.16	10.66	47.17
KJ 1	2	12b	39.05	9.96	43.26	7.74	42.32	10.79	46.88
KJ 1	2	13b	40.01	10.14	42.69	7.16	43.10	10.92	45.98
KJ 1	2	14b	40.18	9.59	43.30	6.93	43.17	10.30	46.52
KJ 1	2	15b	39.75	9.89	43.04	7.31	42.89	10.67	46.44
KJ 1	5	1	40.83	9.00	42.08	8.10	44.43	9.79	45.78
KJ 1	5	2	40.66	9.11	42.27	7.96	44.18	9.90	45.92
KJ 1	5	3	41.49	8.83	42.30	7.38	44.80	9.53	45.67
KJ 1	5	4	41.97	8.85	42.39	6.80	45.03	9.49	45.48
KJ 1	5	5	41.83	8.79	42.48	6.90	44.93	9.44	45.62
KJ 1	5	6	41.92	9.18	42.13	6.77	44.96	9.85	45.19
JRG 07	2	1a	39.70	13.29	42.39	4.62	41.62	13.94	44.44
JRG 07	2	2a	39.58	12.93	42.49	5.00	41.66	13.61	44.73
JRG 07	2	3a	39.73	12.40	43.40	4.47	41.59	12.98	45.43
JRG 07	2	4a	44.91	8.02	43.26	3.80	46.69	8.34	44.97
JRG 07	2	5a	46.01	7.80	43.14	3.06	47.46	8.05	44.50
JRG 07	2	6a	45.65	7.83	43.33	3.19	47.16	8.09	44.76
JRG 07	2	7a	40.18	12.89	42.31	4.63	42.13	13.51	44.36
JRG 07	2	8a	45.00	8.45	43.33	3.22	46.50	8.73	44.78
JRG 07	2	9a	45.91	8.35	42.71	3.03	47.35	8.61	44.04
JRG 07	2	10a	44.46	8.56	43.27	3.71	46.17	8.89	44.94
JRG 07	2	11a	39.36	13.07	41.89	5.68	41.73	13.86	44.41
JRG 07	2	12a	44.10	9.35	42.50	4.05	45.96	9.75	44.30

Table 13 - Continued

## PYROXENE TRANSECTS

Tertiary:			End-member mole percentages				Normalized end-members		
Sample	Mineral #	Point #	En(Mg)	Fs(Fe*)	Wo(Ca)	Other	En(Mg)	Fs(Fe*)	Wo(Ca)
JRG 07	2	1b	39.69	13.11	42.46	4.74	41.67	13.76	44.57
JRG 07	2	2b	39.79	13.11	42.55	4.55	41.68	13.73	44.58
JRG 07	2	3b	40.14	12.88	42.39	4.60	42.07	13.50	44.43
JRG 07	2	4b	39.73	12.69	42.84	4.74	41.71	13.32	44.97
JRG 07	2	5b	39.70	13.00	42.66	4.64	41.63	13.63	44.74
JRG 07	2	6b	40.28	12.91	42.25	4.56	42.20	13.53	44.27
JRG 07	2	7b	44.78	8.37	43.08	3.78	46.54	8.69	44.77
JRG 07	2	8b	44.66	8.26	43.42	3.65	46.35	8.58	45.07
JRG 07	2	9b	45.42	7.98	43.20	3.40	47.02	8.26	44.72
JRG 07	2	10b	46.23	7.42	43.37	2.99	47.65	7.65	44.70
JRG 07	2	11b	45.50	8.09	42.71	3.71	47.25	8.40	44.35
JRG 07	2	12b	45.24	8.54	42.83	3.39	46.82	8.84	44.34
JRG 07	2	13b	45.89	8.88	40.80	4.43	48.02	9.30	42.69
JRG 07	2	14b	44.83	8.08	43.11	3.98	46.69	8.41	44.90
JRG 07	2	15b	45.62	8.21	41.99	4.18	47.61	8.57	43.83
JRG 07	3	1	40.22	12.81	37.90	9.07	44.24	14.09	41.68
JRG 07	3	2	42.24	10.75	41.06	5.95	44.91	11.43	43.66
JRG 07	3	3	42.66	9.94	42.22	5.18	44.99	10.48	44.52
JRG 07	3	4	39.98	14.58	41.59	3.85	41.58	15.16	43.26
JRG 07	3	5	39.90	14.45	42.10	3.55	41.37	14.98	43.65
JRG 07	3	6	39.77	14.36	42.45	3.41	41.18	14.87	43.95
JRG 07	3	7	40.13	13.94	41.37	4.56	42.05	14.61	43.35
JRG 07	3	8	40.31	13.59	42.20	3.90	41.95	14.14	43.92
JRG 07	3	9	41.16	13.39	40.87	4.58	43.14	14.03	42.83
JRG 07	5	1a	43.34	9.23	41.98	5.45	45.84	9.76	44.40
JRG 07	5	2a	42.86	9.63	42.12	5.39	45.30	10.18	44.52
JRG 07	5	3a	42.34	10.06	41.64	5.96	45.03	10.70	44.28
JRG 07	5	4a	43.29	9.23	41.89	5.60	45.85	9.78	44.37
JRG 07	5	5a	43.42	9.29	41.73	5.57	45.98	9.83	44.19
JRG 07	5	6a	44.01	9.12	41.89	4.98	46.31	9.60	44.08
JRG 07	5	7a	46.75	9.84	40.46	2.95	48.17	10.14	41.69
JRG 07	5	8a	45.16	8.68	42.21	3.94	47.02	9.04	43.95
JRG 07	5	9a	42.86	9.99	41.76	5.39	45.30	10.56	44.14
JRG 07	5	10a	45.96	9.26	41.69	3.10	47.42	9.55	43.02
JRG 07	5	11a	46.43	9.18	41.42	2.98	47.85	9.46	42.69
JRG 07	5	12a	44.50	8.97	42.14	4.39	46.54	9.38	44.08

Table 13 - Continued

PYROXENE TRANSECTS

Tertiary:			End-member mole percentages				Normalized end-members		
Sample	Mineral #	Point #	En(Mg)	Fs(Fe*)	Wo(Ca)	Other	En(Mg)	Fs(Fe*)	Wo(Ca)
JRG 07	5	1b	46.50	7.93	42.03	3.54	48.21	8.22	43.57
JRG 07	5	2b	46.46	7.88	42.21	3.45	48.12	8.17	43.72
JRG 07	5	3b	43.50	9.79	41.22	5.49	46.02	10.36	43.62
JRG 07	5	4b	45.21	8.57	42.60	3.62	46.91	8.90	44.20
JRG 07	5	5b	46.57	8.12	41.88	3.43	48.23	8.41	43.36
JRG 07	5	6b	41.75	9.93	43.15	5.18	44.03	10.47	45.50
JRG 07	5	7b	43.45	9.41	41.69	5.46	45.96	9.95	44.09
JRG 07	5	8b	42.44	10.56	41.15	5.85	45.08	11.22	43.70
JRG 07	5	9b	41.30	10.64	42.34	5.72	43.81	11.28	44.91
JRG 07	5	10b	48.63	7.86	41.02	2.49	49.87	8.06	42.06
JRG 07	5	11b	45.22	9.59	41.99	3.20	46.71	9.91	43.38
JRG 07	5	12b	44.19	9.02	42.26	4.53	46.29	9.45	44.26
JRG 07	5	13b	40.53	12.61	41.86	5.00	42.66	13.28	44.06
JRG 07	5	14b	44.27	9.50	41.46	4.77	46.49	9.97	43.53

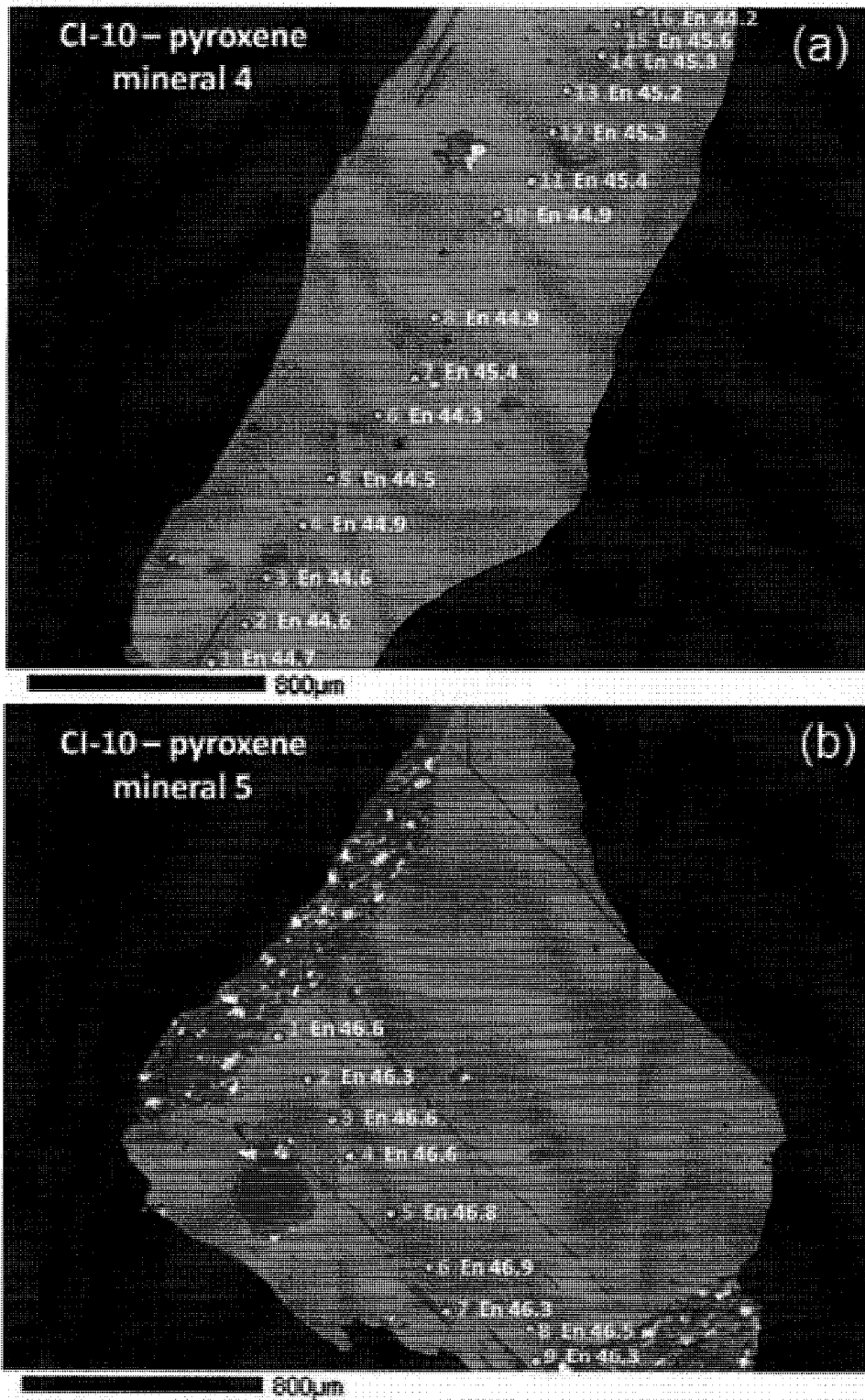


**Figure 31:** Microphotograph of CI-10 pyroxene minerals #4(a) and #5(b). The dots represent points measured along a transect of the crystal, with each of their enstatite end-member compositions shown as an example of how the composition varies spatially.

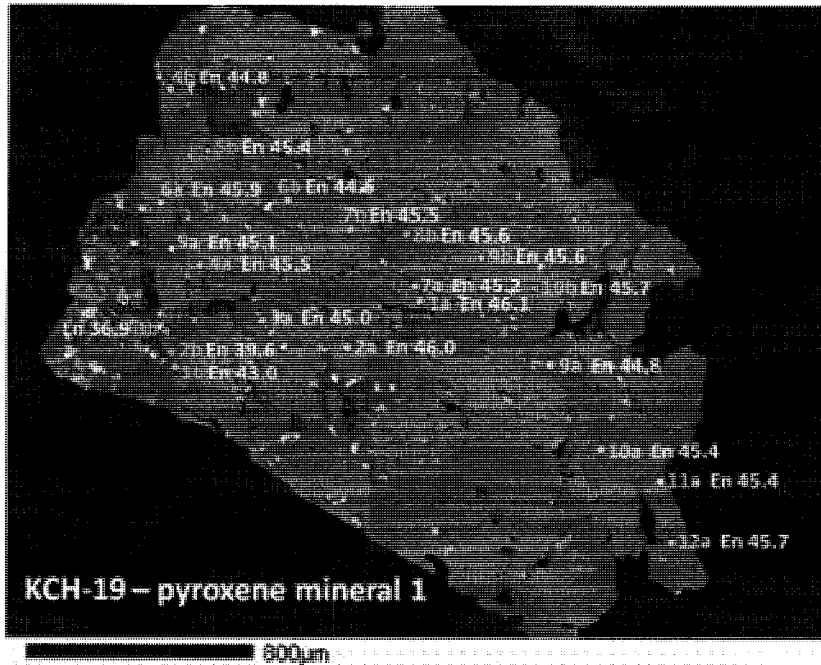


**Figure 32:**  
Microphotograph of KCH-19 pyroxene mineral #1. The dots represent points measured along a transect of the crystal, with each of their enstatite end-member compositions shown.

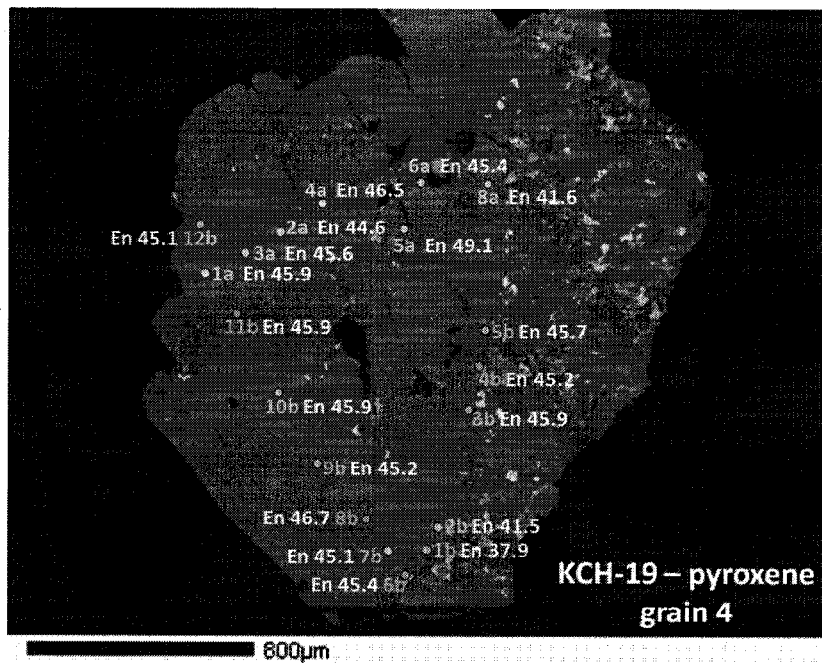


**Figure 33:**  
Microphotograph of KCH-19 pyroxene mineral #4. The dots represent points measured along a transect of the crystal, with each of their enstatite end-member compositions shown.

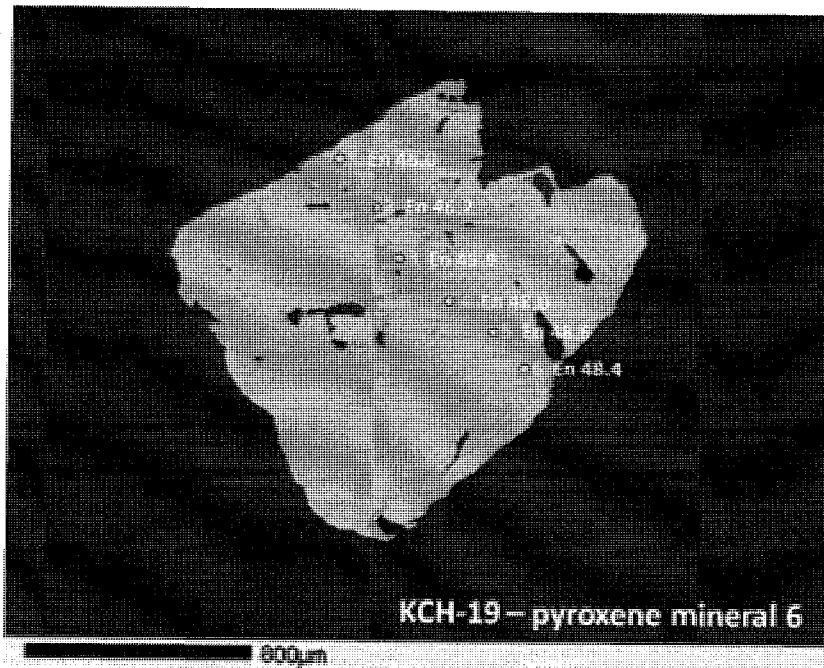


**Figure 34:**  
 Microphotograph of KCH-19 pyroxene mineral #6. The dots represent points measured along a transect of the crystal, with each of their enstatite end-member compositions shown.

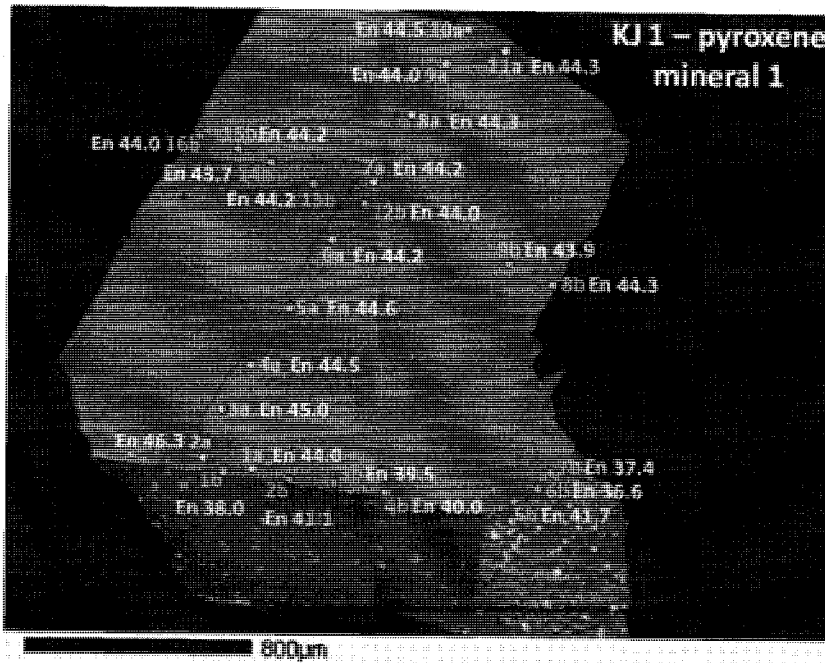


**Figure 35:**  
 Microphotograph of KJ 1 pyroxene mineral #1. The dots represent points measured along a transect of the crystal, with each of their enstatite end-member compositions shown.

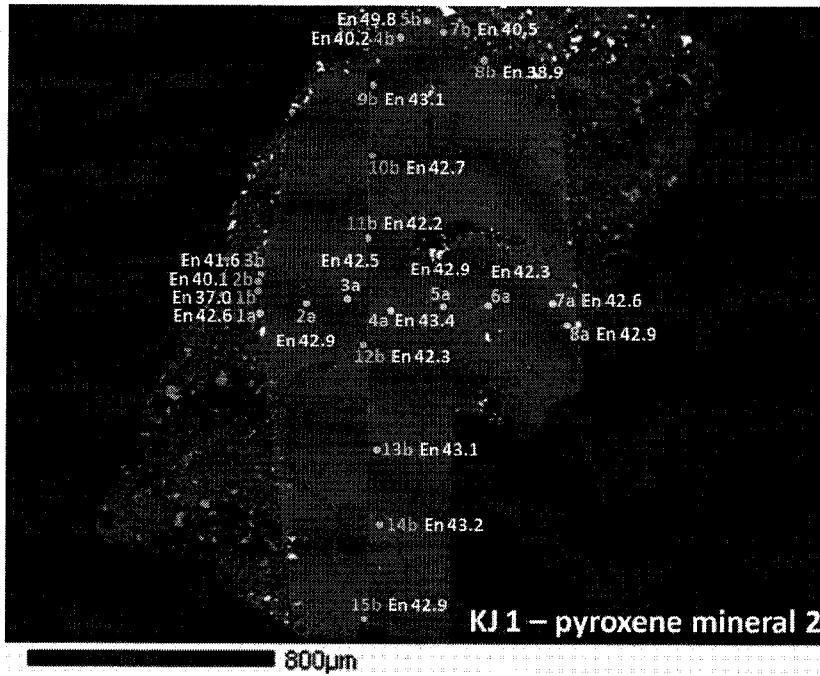


**Figure 36:**  
Microphotograph of KJ 1 pyroxene mineral #2. The dots represent points measured along a transect of the crystal, with each of their enstatite end-member compositions shown.

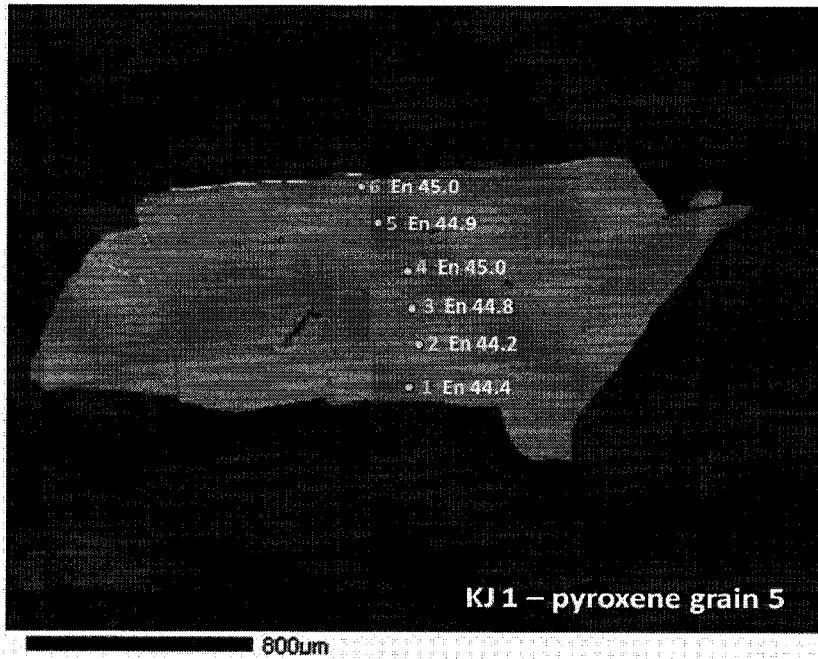


**Figure 37:**  
Microphotograph of KJ 1 pyroxene mineral #5. The dots represent points measured along a transect of the crystal, with each of their enstatite end-member compositions shown.



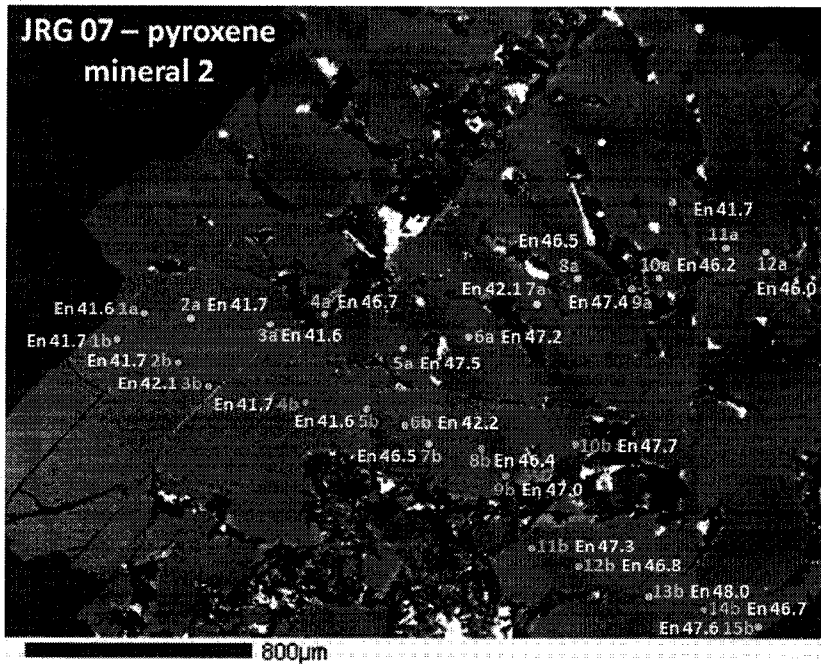


**Figure 38:**  
Microphotograph of JRG 07 pyroxene mineral #2. The dots represent points measured along a transect of the crystal, with each of their enstatite end-member compositions shown.

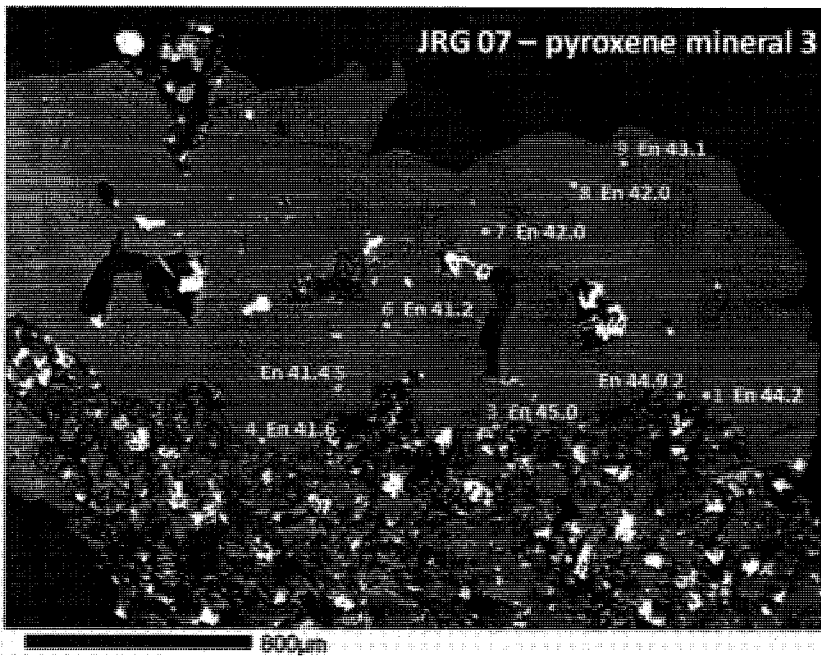


**Figure 39:**  
Microphotograph of JRG 07 pyroxene mineral #3. The dots represent points measured along a transect of the crystal, with each of their enstatite end-member compositions shown.

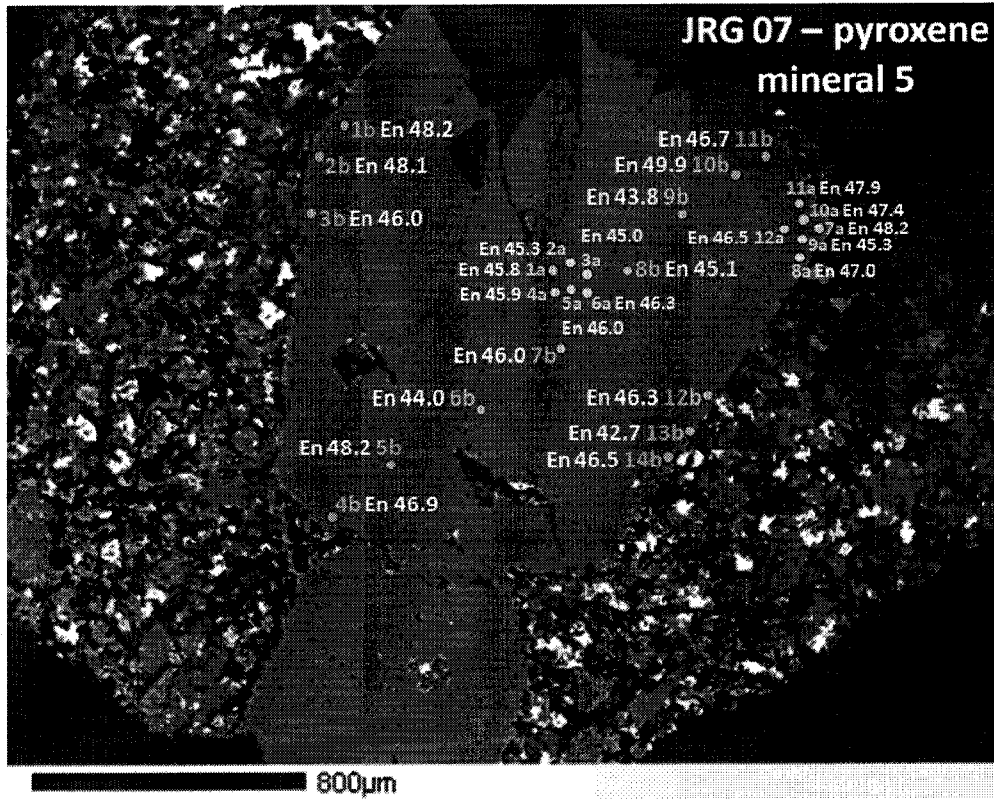


**Figure 40:**

Microphotograph of JRG 07 pyroxene mineral #5. The dots represent points measured along a transect of the crystal, with each of their enstatite end-member compositions shown.

## APPENDIX D

### SAMPLE PREPARATIONS AND CHEMICAL PROCEDURES

#### Hafnium (Hf) Procedures

##### Sample Preparation

1. Cut down rock sample with a saw or hammer until about of fist sized piece – or pieces – of rock is obtained. Crush each sample in a stainless steel mortar and pestle to approximately sand sized grains. Between samples clean the mortar and pestle by scrubbing with stainless steel brushes, then wipe down with lent free tissues (i.e. Kimwipes) and alcohol until the mortar and pestle wipe clean. Store the crushed samples in clean labeled plastic vials.
2. Pick the sand sized grains with titanium (Ti) tweezers, picking for cleanliness and size, using a binocular microscope. The grains need to be 1 to 1.5 mm so they will be able to fully dissolve during the dissolution steps. Each grain must be clean, with no weathering, no rind, no rust, no zeolites, and no saw marks (if the sample has been cut). The grains that usually meet these requirements are from inside the rock, away from any surface exposed to the atmosphere, water, and chemical weathering. In order to get accurate Hf isotope ratios about 500 ng Hf is needed; with basalts about 0.5 g of clean picked grains per sample should suffice.

##### Vial Preparation

3. A 7 ml Savillex vial that has been cleaned appropriately for Hf chemistry is needed for each sample plus one additional vial to be used as a blank. Add a drop of 3 times distilled 1 N HBr to each empty clean vial then cap and place on a hotplate at 90° C to flux overnight. This step removes all possible lead (Pb) from the vials.
4. Remove vials from the hotplate and let cool down, and then rinse out the vials with nanopure water three times. Place the empty vials back on the hotplate uncapped to dry.

### **Weighing**

5. Weigh the picked samples into the dry cleaned vials on a high precision scale that measures to the 5<sup>th</sup> decimal place. Record each sample's mass.

### **Leaching/Rinsing**

6. Add 3 times distilled 2.5 N HCl to each sample, enough to fully cover the entire sample. Let samples sit for 5 minutes in the HCl, and then pipette out the HCl into a waste container. Rinse the samples 3 times with nanopure water, each time letting the sample sit in the water for 5 minutes before being pipetted out. Next add 3 times distilled 1 N HBr to the samples and let sit for 5 minutes. Then pipette out the HBr into a waste container and rinse the samples with nanopure water 3 times, as done after the HCl leach.

### **Dissolution**

7. Add 18 drops of 3 times distilled concentrate HNO<sub>3</sub> to each sample. If the 18 drops do not entirely cover the sample then add few more drops. Allow the samples to sit in the HNO<sub>3</sub> until any reactions taking place have slowed or stopped. Add 3 times distilled concentrate HF, enough to obtain about 5 ml total solution. The samples are then capped and placed on a hotplate at 90° C to dissolve for about 36 hours.

8. Let samples cool to room temperature then uncap the samples and dry down at 90° C on a hotplate. When they are near dry reduce the temperature to 80° C to prevent splattering and then let the samples dry completely.

9. Add 1.46 ml 3 times distilled concentrate HF to each sample. Cap the vials very tightly and place in a dry bath at 110° C for 48 hours. This step brings all the high field strength elements (HFSE), including Hf, into solution.

10. Remove samples from the dry bath and let cool down. Ultrasonicate samples for 1.5 hours. The samples are then shaken vigorously on a shaker for 10 minutes. Then transfer the entire sample and solution from the Savillex vials into 1.5 ml centrifuge tubes. Centrifuge the samples for 4 minutes at 11,000 rpm. Rinse the Savillex vials that had contained the samples 3 times with nanopure water. Pour the leachate within the centrifuge tubes out into the rinsed corresponding Savillex vials. Add 1.1 ml 3 times distilled concentrate HF into each centrifuge tube with the remaining solids. Tap each tube vigorously to dislodge the solids into the HF. Place centrifuge tubes in a shaker and shake vigorously for 10 minutes, then ultrasonicate for 2 hours. Centrifuge the samples for 4 minutes at 11,000 rpm and then decant them again into the corresponding Savillex vials. Repeat the steps of adding 1.1 ml 3 times distilled concentrate

HF, tapping, shaking, ultrasonication, centrifuging, and decanting once more for a total of decanting 3 times.

11. Add 1.1 ml 3 times distilled concentrate HF to the solids in the centrifuge tubes again, then tap and shake them once more, let sit in solution over night. The next day shake the centrifuge tubes once more, ultrasonicate for 2 hours, centrifuge for 4 minutes at 11,000 rpm, and decant the solution into the Savillex vials. This decanting process concentrates all HFSE into the HF in the Savillex vials. The remaining solids of each sample in the centrifuge tubes are put aside for Pb, strontium (Sr) and neodymium (Nd) analyses. The sample solutions in the 7 ml Savillex vials are what continue on for Hf separation.

12. Place the Savillex vials on a hotplate at 90° C and dry down completely.

13. Add 1.0 ml 3 times distilled 0.5 N HF to each sample and cap them. Shake the samples then let sit on a hotplate at 90° C for 24 hours.

14. Shake and ultrasonicate the samples multiple times until all solids have dissolved. Then uncap and place on a hotplate at 90° C to dry down completely.

15. Once dry, add 1 ml 3 times distilled 0.5 N HF: 0.5 N HCl solution to each sample. Shake the samples and let sit in solution over night at room temperature.

16. Shake, ultrasonicate, and heat the samples for 20 to 30 minutes at a time until all the sample was fully dissolve. Let the samples sit over night at room temperature again.

#### **Hf Column #1 (Hf-Ti-Zr Separation)**

17. Shake the samples for 10 minutes then ultrasonicate for 1 hour to ensure entire sample has been dissolved.

18. Transfer the dissolved samples into 1.5 ml centrifuge tubes and centrifuge 4 minutes at 11,000 rpm.

Note: The columns to be used are 11 ml polyethylene with AG 1x8 100 – 200 mesh anion exchange resin that fills the column to the top of the stem. The columns have been cleaned by alternating full reservoirs of 1 time distilled 6 N HCl and nanopure water dripping through the resin 3 times each, then 1 reservoir of 4 times distilled concentrate HF, and lastly 3 reservoirs of nanopure water.

19. Condition the clean columns with 6 ml 3 times distilled 0.5 N HF: 0.5 N HCl solution and let drip through completely.

20. Pipette the centrifuged samples solutions into the corresponding columns with clean pipette tips, making sure to not add any solids.
21. Rinse the columns twice, each time with 1 ml 3 times distilled 0.5 N HF: 0.5 N HCl solution. Let the first rinse drip completely through before adding the second. The solution dripping out of the columns is all waste, collect in waste containers.
22. Flush out the bulk of the sample with 8 ml 3 times distilled 0.5 N HF: 0.5 N HCl solution. Then follow with a 10 ml flush with the same solution as the first, collecting both in waste containers.
23. Rinse the Savillex vials that contained the samples before they were centrifuged 3 times with nanopure water. Add a drop of 3 times distilled 6 N HCl to each vial, then cap and flux on a hotplate at about 60° C for at least 30 minutes. Remove the vials from the hotplate, empty into waste containers, and rinse 3 times with nanopure water.
24. After the flushes have completely dripped through, place the rinsed Savillex vials under the corresponding columns to collect the elution.
25. Add 6 ml 3 times distilled 6 N HCl to each column to elute Hf, Ti, and Zr.
26. Once all 6 ml HCl has dripped through, add 9 drops of concentrate pure HClO<sub>4</sub> to the vials with the solution. Place the samples in a dry bath at 130° C and dry down until each sample has about 2 ml of solution. Remove from heat and let sit over night.
27. Clean the columns by following the procedures described in the note above.

#### **Removal of Fluorides by Perchloric Evaporation**

28. Uncap samples and place in dry bath at 150° C, dry down samples until 0.5 ml solution is left.
29. Add 10 drops of concentrate pure HClO<sub>4</sub> to the solution and dry down in the dry bath until the solution reaches 0.5 ml again. This process is repeated 3 times; after the 3<sup>rd</sup> time dry the sample down to 0.25 ml then remove from heat, cap, and let sit overnight.

If at any time during this procedure a precipitate forms (usually appears as a cloudy white color in the solution) add 3 drops of 3 times distilled concentrate HF and begin the procedure over again from the first dry down in step 28. Precipitate may form in a sample more than once, each time add the HF and begin the procedure over again up to a total of 3 times. Once HF has been

added a third time, begin the procedure over and complete whether or not precipitate forms a 4<sup>th</sup> time.

By the time the procedure is complete the samples should be in solution with 0.25 concentrate pure HClO<sub>4</sub>; all the HCl and HF has evaporated.

### **Hf Column #2 (Hf-Zr Separation)**

Note: The columns to be used are Savillex PFA Teflon microcolumns with 15 ml reservoir and 14 cm stem (5 mm I.D.) with a 35 mesh frit. The stem is filled to the base of the reservoir with AG 50Wx8 200 – 400 mesh. The columns have been cleaned by backwashing resin with 10 ml nanopure water, this is done using a vacuum to pull resin with the water up into the reservoir, then allowing the resin to resettle in the stem as the water drips through. Then 10 ml of 4 times distilled 4 N HF wash dripped through, then 2 washes with 10 ml of 6 N HCl, then a backwash with 10 ml of 2.5 N HCl. The columns are then stored sealed with 2.5 N HCl filled to the base of the reservoir (all the resin needs to be fully covered).

30. Unseal the clean columns and allow all 2.5 N HCl to drip through.
31. Condition the columns with 8 ml 2.5 N HCl, allow to drip through completely.
32. Prepare column wash while the condition drips through. For 8 columns: 60 ml 2.5 N HCl is combined with 0.24 ml concentrate H<sub>2</sub>O<sub>2</sub> in a 60 ml Savillex vial.
33. Prepare samples for loading while the condition continues to drip though. To each sample add 0.3 ml 2.5 HCl and 30 µl concentrate H<sub>2</sub>O<sub>2</sub>, samples should already contain approximately 0.25 ml HClO<sub>4</sub> from Perchloric evaporation process. When H<sub>2</sub>O<sub>2</sub> is added to the sample the sample should become bright red.
34. Transfer samples to 1.5 ml centrifuge tubes and centrifuge 4 minutes at 11,000 rpm.
35. Load samples onto columns once the condition has completely dripped through; load them directly onto the resin from the centrifuge tubes with a 200 µl pipette. The bubbles in sample and resin from the H<sub>2</sub>O<sub>2</sub> are normal.
36. Rinse columns with 0.4 ml of the prepared 2.5 N HCl and trace H<sub>2</sub>O<sub>2</sub> wash. The rinse and wash are collected with waste containers.
37. Wash columns with 5 ml of the same wash solution, eliminating the bulk Ti.

38. While the wash drips through, rinse the original Savillex vials that contained the samples 3 times with nanopure water, then reflux vials with 6 N HCl. When the wash is almost completely drained rinse the vials 3 times with nanopure water.
39. Place cleaned vials under the columns after the wash has completely dripped through.
40. Elute Hf and Zr with 2.5 N HCl: 0.3 N HF.
41. When all 5 ml are collected place the samples uncapped on hotplate at 90° C and dry down. Store Hf samples dry and capped until ready to be analyzed.
42. Clean the columns by following the procedures described in the note above.

### **Lead (Pb) Procedures**

#### **If Hf analyses are first conducted:**

Use precipitate stored in the centrifuge tubes from the decanting process.

Add 1 ml 3 times distilled 6 N HCl to centrifuge tubes that contain the precipitate, tap and shake the tubes to dissolve the precipitate into solution. Transfer the solution into Pb cleaned and labeled 7 ml Savillex vials. Repeat the process of adding 1 ml 6 N HCl to centrifuge tube and transferring the solution into the Savillex vials 3 more times, for a total of 4 ml 6 N HCl. Place capped on hotplate at 90° C and let sit overnight. Continue on step 10 of Pb procedures.

#### **If Hf analyses are not conducted:**

Follow Hf procedures: Steps 1 through 8.

9. Once HF has been dried down, add 4 ml 3 times distilled 6 N HCl, cap the vials and place on hotplate at 90° C and let sit overnight.
10. Uncap vials and place on hotplate at 90° C to dry down. When the samples are almost dry (when about 0.5 ml are left) turn down heat to 80° C to prevent splattering. Allow to dry completely.
11. Add 1.78 ml 1 N HBr to dry samples. Heat, shake, and ultrasonicate samples as needed to aid in dissolving the sample, though some white/clear solid will remain. Then place capped samples on hotplate overnight at 80° C.



## **Pb Column #1**

Note: The columns to be used are made of TFE tubing with a 3 ml reservoir and 6 cm stem that holds 500  $\lambda$  AG 1x8 100 – 200 mesh resin. New resin is used each time. Columns are stored in 8 N HNO<sub>3</sub> until ready for use. Resin is stored in a Teflon dropper bottle in nanopure water.

12. Remove columns from 8 N HNO<sub>3</sub> and rinse with nanopure water.
13. For each column, fill stem and about 1 ml of the reservoir with nanopure water. Tap out all bubbles from the stem. Before the water drains down to the stem add about 11 drops of resin from the dropper bottle to the column. The stem needs to be filled to the top with resin. Let the nanopure water drain through the column.
14. Rinse the resin with 3 ml nanopure water, let drip through completely. While rinse drains: if Sr and/or Nd are going to be analyzed add 6 N HCl to cleaned 15 ml Teflon vials used for Sr/REE. Let flux on a hotplate at 80° C.
15. While the rinse continues to drain, transfer samples into 2 ml labeled centrifuge tubes, centrifuge for 4 minutes at 11,000 rpm.
16. Wash resin with 3 ml 6 N HCl and let drip through completely. Then wash resin with 3 ml nanopure water and let drip through completely. Then condition resin with 1 ml 1 N HBr.
17. Once the condition has dripped through completely, add a few drops of 1 N HBr to column and pour off into waste to remove excess resin in the reservoir. If analyzing Sr and/or Nd: remove Sr/REE vials from hotplate and rinse 3 times with nanopure water. Place the Sr/REE vials under the columns to collect bulk waste from Pb columns; the bulk waste will contain the Sr and REEs from each sample.
18. Pour samples from centrifuge tube into corresponding columns, let drip through completely.
19. Add 1 ml 1 N HBr wash, let drip through completely. Then add 3 ml 1 N HBr wash, let drip through completely. If collecting for Sr and/or Nd: remove Sr/REE vial and cap the vial. Place aside with the centrifuge tubes containing precipitate for Sr and/or Nd procedures later. Place waste beakers under the columns.
20. Add 2.5 ml 2 N HCl wash to columns, let drip through completely. While wash drains, rinse original Savillex vials containing samples 3 times with nanopure water.

21. Place rinsed Pb vials under corresponding columns and then elute Pb with 3 ml 6 N HCl.
22. Place the vials uncapped on hotplate and dry down the samples overnight at 65° C.
23. Rinse resin out of the columns with nanopure water, then store columns in 8 N HNO<sub>3</sub>.

### **Pb Column #2**

Note: The columns to be used are made of TFE tubing with a 1.5 ml reservoir and 5 cm stem that holds 200  $\lambda$  AG 1x8 100 – 200 mesh resin. New resin is used each time. Columns are stored in 8 N HNO<sub>3</sub> until ready for use. Resin is stored in a Teflon dropper bottle in nanopure water.

24. Remove columns from 8 N HNO<sub>3</sub> and rinse with nanopure water.
25. For each column, fill stem and about 0.5 ml of the reservoir with nanopure water. Tap out all bubbles from the stem. Before the water drains down to the stem add about 5 drops of resin from the dropper bottle to the column. The stem needs to be filled to the top with resin. Let the nanopure water drain through the column.
26. Rinse the resin with 1 ml nanopure water, let drip through completely.
27. While the rinse drains: add 1 drop 2 N HCl to the dried down sample that was eluted from Pb column #1. Roll the drop of HCl around the vial to dissolve sample. Add 0.5 ml 1 N HBr, and then cap the vials and place on hotplate at about 45° C to warm samples.
28. Wash resin with 1 ml 6 N HCl and let drip through completely. Then wash resin with 1 ml nanopure water and let drip through completely. Next, condition resin with 1 ml 1 N HBr. Once the condition has dripped through completely, add a few drops of 1 N HBr to column and pour off into waste to remove excess resin in the reservoir.
29. Add 0.4 ml 1 N HBr to each vial with sample, swirl solution to dissolve any remaining sample, then pour samples into corresponding columns, let drip through completely.
30. Add 0.8 ml 1 N HBr wash, let drip through completely. Then add 0.8 ml 2 N HCl wash to columns, let drip through completely.

31. Place original Pb vials under corresponding columns and then elute Pb with 1 ml 6 N HCl.
32. Place the vials uncapped on hotplate and dry down the samples at 80° C.
33. Rinse resin out of the columns with nanopure water, then store columns in 8 N HNO<sub>3</sub>.
34. Once the Pb sample has dried completely add 2 drops concentrate HNO<sub>3</sub>, swirl around to dissolve. Dry down on a hotplate at 80° C then store Pb samples dry and capped until ready to be analyzed.

### **Strontium (Sr) and Neodymium (Nd) Procedures**

Note: Assuming Pb has been run, using precipitates in centrifuge tubes and the Pb bulk waste collected in Sr/REE 15 ml Savillex vials from Pb column #1.

#### **Dissolution**

1. Add the precipitate from the centrifuge tubes to the corresponding Sr/REE vials. Liquid from the vials may be added to the precipitate in the centrifuge tubes and shaken to help dislodge the precipitate, and then add to the vials. Add 1 ml concentrate HNO<sub>3</sub> to the centrifuge tubes to dissolve any remaining precipitate, and then pour into the vials. Swirl vials gently to help dissolve the solids. Then place samples uncapped on hotplate to dry down at 90° C.
2. Add 2 ml 6 N HCl to dry samples, this should dissolve most solids. Heat on hotplate capped for about 1 hour at 90° C. Then uncap and dry down on hotplate at the same temperature.
3. Add 1 ml 2.5 N HCl to dry sample. Let the samples heat overnight, capped, on a hotplate at 90° C.
4. Transfer samples from the Sr/REE vials into labeled 2 ml centrifuge tubes. Centrifuge for 4 minutes at 11,000 rpm. Decant the liquid from the centrifuge tubes back into the corresponding vials. Add 1 ml 2.5 N HCl to the solids remaining in the centrifuge tubes, tap the centrifuge tubes to dislodge the solids and then shake them to break up the solids and possibly dissolve some. Centrifuge for 4 minutes at 11,000 rpm, and then decant the liquid into the corresponding vials. Repeat the process one more time with 1 ml 2.5 N HCl. The Sr and REE are in the leachate in the vials.
5. Dry down samples overnight at 65° C.

### **Sr/REE Column (Sr Column #1)**

Note: The columns to be used are quartz glass with a 19 ml reservoir and a 20 cm stem that is 0.5 cm in diameter. The stem holds 3.7 ml of 100 – 200 mesh hydrogen form AG 50Wx8 BioRad cation exchange resin, held by a 35 mesh frit, new resin is used each time. The columns are stored in 8 N HNO<sub>3</sub> until ready for use.

6. Remove columns from 8 N HNO<sub>3</sub> and rinse them with quartz distilled water. Fill the stems with 2.5 N HCl and then add resin to the stem so that resin is filled to the base of the reservoir, the resin must be filled exactly to this point.

7. Condition the resin with 25 ml 3 times distilled 2.5 N HCl. While the condition is dripping through, add 0.6 ml 3 times distilled 2.5 N HCl to the dry samples. Place the samples on the hotplate to warm at 45° C until ready to be loaded on column.

8. Once condition has dripped completely through, load sample onto resin with a 1 ml pipette. Then add 0.5 ml 3 times distilled 2.5 N HCl to the empty Sr/REE vials, swirl to dissolve any remaining sample, and then load solution onto the column. Repeat with another 0.5 ml 3 times distilled 2.5 N HCl.

9. Wash column with 15 ml 3 times distilled 2.5 N HCl, collect in waste beaker. While the wash is dripping rinse the Sr/REE 3 times with nanopure water, then add 6 N HCl, cap, and flux on hotplate at 80° C. After condensation is seen on caps then remove from hotplate and rinse 3 times with nanopure water. These will be used to collect Sr elution.

10. Get a second set of vials to collect REE, vials should be cleaned 15 ml Savillex. Label vials then add 6 N HCl, cap, and let flux on hotplate at 80° C. Before REE are eluted, remove vials from hotplate and rinse 3 times with nanopure water.

11. After the wash has completely dripped through place clean Sr vials under the columns. Elute Sr with 10 ml 3 times distilled nanopure water. Once all has dripped through remove the Sr vial and cap. Place waste beakers under columns.

12. Wash column with 13 ml 2.0 N HNO<sub>3</sub>, then wash with 10 ml 2.0 N HNO<sub>3</sub>. After that has completely dripped through, wash column with 1 ml 6.0 N HNO<sub>3</sub>.

13. After the HCl wash has dripped through, place clean REE vials under the columns. Elute REE with 9.5 ml 6.0 N HNO<sub>3</sub>. Remove REE vial and cap.

14. Rinse resin out of columns with quartz distilled water then place columns back into 8 N HNO<sub>3</sub>.

### **Preparation for Sr Column #2**

15. Dry down sample in Sr vial on hotplate at 90° C. Once sample has about 0.25 ml liquid left, turn down to 70° C. Be careful of static.

16. Once samples are dry add 0.5 ml 3 N HNO<sub>3</sub> and cap. Let stand for at least one night before running through columns. Do not heat sample, let sit at room temperature.

### **EiChrom Sr-Spec Column (Sr Column #2)**

Note: the columns to be used are made from TFE shrink tubing with a 3 ml reservoir and a 4.5 cm stem. The stem holds 0.25 ml EiChrom Sr-Spec resin with a 35 mesh frit, new resin is used each time. Columns are stored in 8 N HNO<sub>3</sub> until ready for use. The resin is stored in a Teflon dropper bottle with quartz distilled water.

17. Remove columns from 8 N HNO<sub>3</sub> and rinse with quartz distilled water.

18. For each column, fill stem and about 1 ml of the reservoir with quartz distilled water. Tap out all bubbles from the stem. Before the water drains down to the stem add about 14 drops of resin from the dropper bottle to the column. The stem needs to be filled to the top with resin. Let the quartz distilled water drain through the column.

19. Rinse the resin with 1 ml quartz distilled water and let drip through completely. Then condition the resin with 0.75 ml 3 times 3 N HNO<sub>3</sub>.

20. Once all the condition has dripped through, pour samples from the vials into the corresponding columns and let drip through completely, collect in waste beakers. Rinse the sample vials 3 times with quartz distilled water, then add 6 N HNO<sub>3</sub> to the vials, cap, and flux on a hotplate at 90° C. Before eluting Sr from the columns remove the vials from heat, pour out HNO<sub>3</sub> into waste, and rinse 3 times with quartz distilled water.

21. Wash column with 0.75 ml 3 N HNO<sub>3</sub> and let completely drip through. Then wash with 2 ml 3 N HNO<sub>3</sub> and let completely drip through.

22. Place cleaned Sr vials under the columns, and then elute Sr with 1 ml quartz distilled water. Once all of the water has dripped through place Sr vials on the

hotplate, uncapped, and dry down at 80° C. Store Sr samples dry and capped until ready to analyze.

23. Rinse resin out of the columns with quartz distilled water, then store columns in 8 N HNO<sub>3</sub>.

### **Preparation for Nd Column**

24. Dry down sample in REE vial on hotplate at 90° C. Once sample has about 0.25 ml liquid left, turn down to 70° C. Be careful of static.

25. Once samples are dry add 0.3 ml 0.18 N HCl and cap. Let stand for at least two nights at room temperature before running through columns. If samples are not dissolving, alternate between heating on hotplate at 45° C for an hour at a time and ultrasonicing for an hour at a time, do so until samples are dissolved.

### **EiChrom SPS Ln-Spec Column (Nd Column)**

Note: the columns to be used are quartz glass with a 20 ml reservoir and a 10 cm stem that holds about 4 ml resin with a 35 mesh frit. There are 3 layers of resin that fill the stem: about a 2 mm layer of 200 – 400 mesh BioRad anion exchange resin base directly on top of the frit, the layer above the base is EiChrom SPS Ln-spec resin that fills the stem up to about 4 mm below the top of the stem, the upper 4 mm of the stem is filled with a 200 – 400 mesh BioRad anion exchange resin cap that holds the Ln-spec in place. The columns are cleaned by washing with 2 ml 6 N HCl, then 6 ml 6 N HCl. Next a 2 ml 0.1 N HCl wash and a 10 ml 0.1 N HCl wash are run through the columns. Lastly a 2 ml 0.18 N HCl followed by a 4 ml 0.18 N HCl are run through the columns. The columns are sealed with the last 4 ml 0.18 N HCl wash in the column to keep the resin wet, and they are stored until ready for use.

26. Unseal the columns and let the 0.18 N HCl wash drain through the columns, collect in waste beakers.

27. Rinse clean pipettes with 0.18 N HCl, one pipette is needed for each sample plus one extra. Once the columns have drained, pipette each sample into the corresponding column. Add 0.3 ml 0.18 N HCl to each vial (with extra pipette) to dissolve any remaining sample, and then pipette the vial rinses into corresponding columns.

28. Wash column with 0.3 ml 0.18 N HCl. Then wash with 17.1 ml 0.18 N HCl. While the wash is dripping through add 6 N HCl to the REE vials, cap, and flux on hotplate at 90° C. Before eluting Nd pour out HCl into waste container and rinse the vials 3 times with quartz distilled water.

29. After wash has dripped completely through, place clean REE vials under corresponding columns and elute Nd with 2 ml 0.18 N HCl, let completely drip through, followed by 6 ml 0.25 N HCl. Once all the HCl has dripped through, place the vials uncapped on the hotplate at 90° C and dry down. Store Nd sample dry and capped until ready to analyze.

30. Clean columns following the instructions listed in the note above.

## APPENDIX E

### ISOTOPE STANDARDS

The Nu Plasma 1700 multicollector inductively coupled plasma mass spectrometer (MC-ICP-MS) in the Baylor Brooks Institute for Isotope Geology in the Department of Geological Sciences at San Diego State University was used to measure new Hf, Pb, and Nd isotope ratios. All samples and standards were diluted in 0.05 N HNO<sub>3</sub>, and about 2 mL of solution was needed for each run. Hf samples and standards were diluted to 100 ppb. Hf isotopic measurements were corrected for instrument drift using standard-sample-standard bracketing with the JMC 475 Hf standard was measured twenty-two times, throughout the analyses, and values are reported in Table 14.

Pb samples and standards were diluted to 30 ppb Pb. The Tl-doping technique was used to correct the standards isotopic values for Pb analyses using NIST SRM 997 Tl (White et al., 2000; and Albarède et al., 2004) and  $^{205}\text{Tl}/^{203}\text{Tl} = 2.3889$  (Thirlwall, 2002). About 6 ng Tl from the NIST SRM 997 Tl was added to 2 mL of the diluted samples and standards to bring the concentrations up to 3 ppb Tl. Within-run fractionation of sample isotopic values was corrected by using standard-sample-standard bracketing and a delta correction using NIST SRM 981 Pb and values from Todt et al. (1996). The NIST SRM 981 Pb standard was run seven times throughout the analyses and the values are reported in Table 15.



Nd samples and standards were diluted to 70 ppb Nd. Nd isotopic measurements were corrected for instrument drift using standard-sample-standard bracketing. The AMES Nd standard was run eight times and the values are reported in Table 16. La Jolla was measured between standards and reported a corrected value of  $^{143}\text{Nd}/^{144}\text{Nd} = 0.511840 \pm 0.000003$ . Within run fractionation was corrected for using  $^{146}\text{Nd}/^{144}\text{Nd} = 0.7219$ .

Sr isotopic values were measured with a VG Sector 54 thermal ionization mass spectrometer (TIMS) at San Diego State University. The Sr isotopic values were corrected for fractionation using the NIST SRM 987 Sr standard. The standard was run eleven times and values are reported in Table 17.

**Table 14:**

**Hf Standard Measurements**  
JMC 475 at 100 ppb Hf

run #	$^{176}\text{Hf}/^{177}\text{Hf}$
1	0.282141
2	0.282140
3	0.282139
4	0.282139
5	0.282138
6	0.282141
7	0.282142
8	0.282145
9	0.282140
10	0.282145
11	0.282143
12	0.282137
13	0.282144
14	0.282144
15	0.282140
16	0.282141
17	0.282142
18	0.282141
19	0.282142
20	0.282138
21	0.282136
22	0.282139
Average	0.282141
Std. Dev.	0.000002

**Table 15:**

**Pb and Tl Standard Measurements**  
 NIST SRM 981 at 30 ppb Pb, NIST SRM 997 at 3 ppb Tl

run #	$^{205}\text{Tl}/^{203}\text{Tl}$	$^{208}\text{Pb}/^{204}\text{Pb}$	$^{207}\text{Pb}/^{204}\text{Pb}$	$^{206}\text{Pb}/^{204}\text{Pb}$
1	2.4305	38.006	15.904	17.237
2	2.4310	38.012	15.906	17.238
3	2.4311	38.019	15.908	17.240
4	2.4308	38.007	15.904	17.237
5	2.4308	38.007	15.905	17.237
6	2.4313	38.023	15.910	17.241
7	2.4310	38.014	15.907	17.239
Average	2.4309	38.013	15.906	17.238
Std. Dev.	0.0003	0.007	0.002	0.002

**Table 16:**

**Nd Standard Measurements**  
 AMES at 100 ppb Nd

run #	$^{143}\text{Nd}/^{144}\text{Nd}$
1	0.512107
2	0.512110
3	0.512106
4	0.512107
5	0.512115
6	0.512116
7	0.512118
8	0.512107
Average	0.512111
Std. Dev.	0.000005

**Table 17:**

**Sr Standard Measurements**  
 NIST SRM 987 Sr

run #	$^{87}\text{Sr}/^{86}\text{Sr}$
1	0.710232
2	0.710231
3	0.710236
4	0.710240
5	0.710238
6	0.710243
7	0.710241
8	0.710237
9	0.710235
10	0.710229
11	0.710241
Average	0.710237
Std. Dev.	0.000005